Markus Flaig

Magnetorotational Turbulence in Protoplanetary Discs

Dissertation

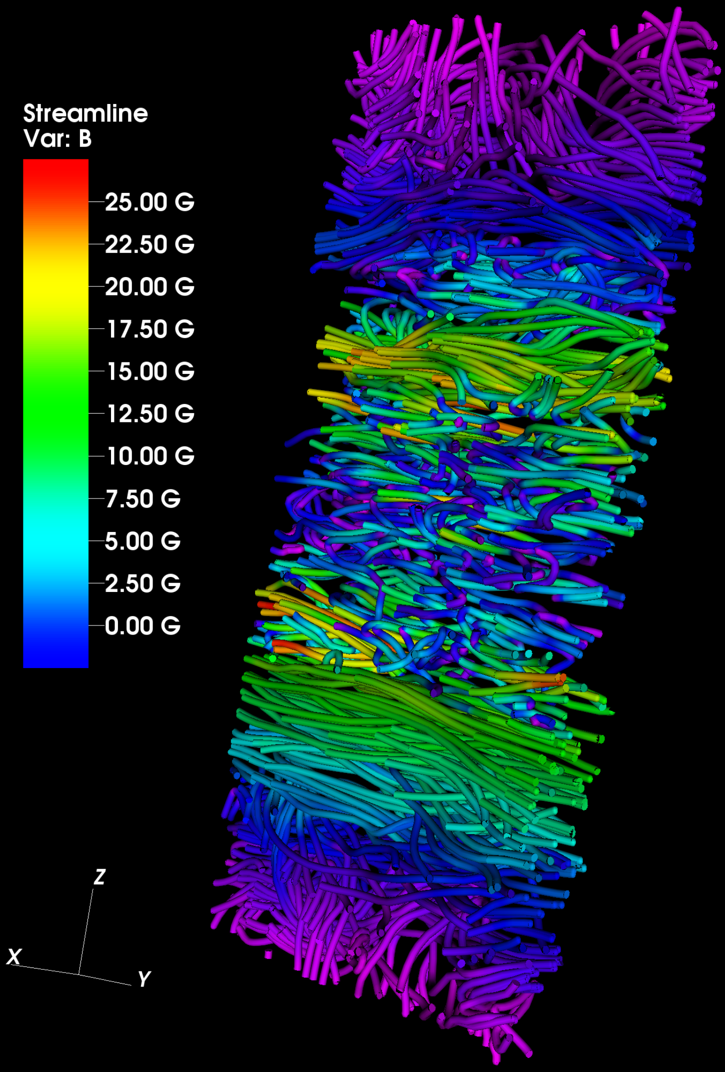
Streamline
Var: B
25.00 G
22.50 G
20.00 G
17.50 G
15.00 G
12.50 G
10.00 G
7.50 G
5.00 G
2.50 G
0.00 G
Z
X
Y

Tübingen, 2011

Magnetorotational Turbulence in Protoplanetary Discs

Dissertation
der Mathematisch-Naturwissenschaftlichen Fakultät
der Eberhard Karls Universität Tübingen
zur Erlangung des Grades eines
Doktors der Naturwissenschaften
(Dr. rer. nat.)

vorgelegt von
Markus Benjamin Flaig
aus Oberndorf a.N.

Tübingen
2011

Tag der mündlichen Qualifikation: 21.06.2011
Dekan Prof. Dr. Wolfgang Rosenstiel
1. Berichterstatter: Prof. Dr. Wilhelm Kley
2. Berichterstatter: Prof. Dr. Klaus Werner
3. Berichterstatter: Prof. Dr. Thomas Henning

Abstract

Protoplanetary discs are disc-shaped structures around T-Tauri stars which are composed of gas and dust. The matter in the disc is accreted onto the host star in a time of several million years. During this phase, the dust particles grow to form larger bodies, eventually leaving behind a planetary system after the disc is gone. It is assumed that the accretion process is powered by turbulence, which most likely is of magnetic origin. The turbulence is not only important concerning the evolution of the disc in general, but might possibly also play a key role in the process of planet formation.

In the present thesis, we describe numerical models of magnetorotational turbulence in protoplanetary discs. We use a modern finite-volume grid code which solves the equations of radiation magnetohydrodynamics in a three-dimensional domain. Being the first radiative models of turbulent protoplanetary discs to date, our simulation provide for the first time a self-consistent and detailed picture of the vertical structure of protoplanetary discs. The turbulent line-broadening that we find in our simulations is consistent with existing astrophysical observations, supporting the assumption that magnetorotational turbulence is indeed present in protoplanetary discs. The numerical tool that we developed provides the basis for future research work where constraints on key physical parameters of protoplanetary discs will be obtained by comparing the results of numerical simulations with astrophysical observations.

Zusammenfassung

Protoplanetare Scheiben sind scheibenförmige Strukturen aus Gas und Staub um T-Taui Sterne. Die Materie in den Scheiben wird im Laufe von mehreren Millionen Jahren auf den Zentralstern akkretiert. Während dieser Phase klumpen die Staubpartikel zu größeren Körpern zusammen, so dass am Ende mglicherweise ein Planetensystem zurückbleibt. Es wird angenommen, dass der Akkretionsprozess durch Turbulenz getrieben wird, welche sehr wahrscheinlich mit Magnetfeldern im Zusammenhang steht. Die Turbulenz ist nicht nur wichtig in Bezug auf die Dynamik der Scheibe im Allgemeinen, sondern spielt möglicherweise auch eine wichtige Rolle bei dem Prozess der Planetenentstehung.

In der vorliegenden Arbeit beschreiben wir numerische Modelle hydromagnetischer Turbulenz in protoplanetaren Scheiben. Wir benutzen einen modernen finite Volumen Gittercode, der strahlungs-magnetohydrodynamischen Gleichungen in drei Dimensionen löst. Als die ersten radiativen Modelle turbulenter protoplanetarer Scheiben, liefern

unsere Simulationen zum ersten Mal ein selbskonsistentes und detailiertes Bild der vertikalen Struktur einer protoplanetaren Scheibe. Die turbulente Linienverbreiterung, die wir in unseren Simulationen finden, stimmt mit bereits existierenden Resultaten aus astrophysikalischen Beobachtungen überein. Somit stützen unsere Ergebnisse die Annahme der Existenz hydromagnetischer Turbulenz in protoplanetaren Scheiben. Das numerische Werkzeug, das wir im Laufe unserer Forschungsarbeit entwickelt haben, bietet ein wertvolle Basis für die Zukunft, um Schlüsselparameter protoplanetarer Scheiben einzuschränken durch den Vergleich der Resultate numerischer Simulationen mit astrophysikalischen Beobachtungen.

Contents

1 Introduction 1
- 1.1 Protostars and Protostellar Discs . . . 3
  - 1.1.1 Formation . . . 3
  - 1.1.2 Classification . . . 4
  - 1.1.3 Typical Parameters . . . 6
- 1.2 Phenomenological Accretion Disc Theory . . . 8
  - 1.2.1 Astrophysical Accretion Discs . . . 8
  - 1.2.2 Theory of Viscous Accretion Discs . . . 9
- 1.3 Summary . . . 13

2 Protoplanetary Disc Physics 15
- 2.1 Fundamental Fluid-dynamical Equations . . . 15
  - 2.1.1 The Equation of Motion for the Neutral Particles . . . 17
  - 2.1.2 Evolution of the Magnetic Field . . . 18
  - 2.1.3 Importance of Non-ideal MHD-effects . . . 20
  - 2.1.4 Thermodynamics . . . 22
  - 2.1.5 Final Set of Equations . . . 25
- 2.2 Accretion Disc Viscosity . . . 25
  - 2.2.1 Molecular Viscosity vs. Turbulent Viscosity . . . 25
  - 2.2.2 Dynamical Foundation of Accretion Disc Viscosity . . . 28
- 2.3 Disc Instabilities . . . 31
  - 2.3.1 Hydrodynamical Shear Instabilities . . . 31
  - 2.3.2 Convective & Baroclinic Instability . . . 32
  - 2.3.3 Gravitational Instability . . . 32
  - 2.3.4 Magnetorotational Instability . . . 33
- 2.4 Numerical Simulations . . . 35
  - 2.4.1 Unstratified Shearing Box Simulations . . . 35
  - 2.4.2 Stratified Simulations . . . 38
  - 2.4.3 Global Simulations . . . 38
- 2.5 Summary . . . 39

3 Linear Growth Phase of the MRI 41
3.1 Local Stability Analysis . . . 41
3.2 Ideal MHD Dispersion Relation . . . 42
3.2.1 Incompressible Fluid . . . 43
3.2.2 Including Compressibility . . . 45
3.3 General Dispersion Relation . . . 47
3.3.1 Linearised Equations . . . 47
3.3.2 Dispersion Relation . . . 49
3.3.3 Eigenfunctions . . . 51
3.4 Effect of Resistivity and Radiation Transport . . . 52
3.4.1 Resistivity . . . 52
3.4.2 Radiation Transport . . . 53
3.5 Summary . . . 61

4 Local Shearing Box Simulations 63
4.1 Numerical Schemes . . . 63
4.1.1 Finite Difference vs. Finite Volume . . . 63
4.1.2 The ZEUS code . . . 64
4.1.3 A Simple Finite Volume Scheme . . . 65
4.1.4 Godunov Schemes . . . 73
4.1.5 Evolution of the Magnetic Field . . . 73
4.1.6 Radiation Transport . . . 74
4.2 Code Tests . . . 76
4.2.1 Convergence Tests . . . 76
4.2.2 Code Comparison . . . 77
4.2.3 Resolution Study . . . 81
4.3 Investigating the Influence of Radiation Transport on Magnetorotational Turbulence . . . 82
4.3.1 Saturation Level . . . 85
4.3.2 Temperature Distribution . . . 86
4.4 Summary . . . 88

5 Simulations Including Vertical Stratification 91
5.1 Stratified Local Shearingbox . . . 91
5.1.1 Boundary Conditions . . . 92
5.1.2 Initial Conditions . . . 96
5.2 Simulation Runs . . . 98
5.2.1 Overview . . . 98

5.2.2 Turbulent Saturation Level . . . 101
5.2.3 Vertical Structure . . . 101
5.3 Summary . . . 104

6 Radiative Models of Protoplanetary Discs 105
6.1 Numerical Setup . . . 106
6.1.1 Boundary Conditions . . . 107
6.2 The Physical Model . . . 107
6.2.1 Basic Parameters of the “Hot” Model . . . 108
6.2.2 Stellar Irradiation . . . 108
6.2.3 Opacity . . . 110
6.2.4 Turbulent Dissipation . . . 111
6.2.5 Initial Conditions . . . 111
6.2.6 Test Problem: Equilibrium Temperature Profile . . . 112
6.3 Simulation Results I: “Hot” Disc Model . . . 113
6.3.1 Time History . . . 116
6.3.2 Vertical Structure . . . 121
6.3.3 Density & Temperature Profile . . . 121
6.3.4 Magnetic Field . . . 122
6.3.5 Turbulent Stresses . . . 125
6.3.6 Turbulent Velocities . . . 126
6.3.7 Turbulent Saturation Level . . . 127
6.4 Simulation Results II: “Cool” Disc Model . . . 128
6.4.1 Time History . . . 129
6.4.2 Turbulent Stresses . . . 132
6.4.3 Temperature . . . 132
6.5 Summary . . . 136

7 Summary and Outlook 137

A Table of Physical and Astronomical Constants 151

B Table of Mathematical Symbols 153

List of Figures

1.1 Exoplanets: Semi-major axis vs. mass distribution 2
1.2 Hubble view of the Orion nebula 2
1.3 Model spectral energy distribution 5
1.4 Classification of protoplanetary discs 5

2.1 Sketch of an MRI-turbulent protoplanetary disc 21
2.2 Difference between molecular and turbulent viscosity 27
2.3 Basic mechanism of the MRI 34
2.4 Numerical simulations of the MRI 36

3.1 MRI growth rates (incompressible case) 44
3.2 MRI growth rates (compressible case) 48
3.3 Effective adiabatic index 55
3.4 Growth rates obtained with explicit scheme 57
3.5 Growth rates obtained with implicit scheme 58
3.6 Sketch of the MRI eigenmodes 60

4.1 Sketch of Riemann fans 69
4.2 Single MRI Mode Convergence Test 78
4.3 Magnetic and thermal energy for code comparison simulations 80
4.4 Resolution study – alpha parameter 83
4.5 Alpha parameter for 3D shearing-box simulations 84
4.6 Magnetic energy in 3D shearing box simulations 87
4.7 Temperature distribution with and without radiation transport 88
4.8 Temperature distribution in the density-thermal energy plane 89

5.1 Time history of alpha parameter 100
5.2 Plot of gas pressure and magnetic pressure for model `I6D` 102
5.3 Plots of the vertical stress profiles found in model `I6D` 102
5.4 Magnetic field configuration for model `rs32` 103

6.1 Distribution of mass in the solar system 109
6.2 Opacity landscape 110
6.3 Vertical structure for a disc in hydrodynamical equilibrium 114
6.4 Time history for model `R7` 117
6.5 Correlation between alpha stress and photospheric temperature 119
6.6 Snapshots from model `R6D` 120
6.7 Temperature profile 122
6.8 Density profile 123
6.9 Gas pressure and magnetic pressure 123
6.10 Magnetic field configuration for model `R6D` 124
6.11 Turbulent stresses 125
6.12 Turbulent velocities 126
6.13 Resolution study 128
6.14 Time history of model `ri32` 131
6.15 Space-time plot of turbulent stresses for the “cool” model 133
6.16 Alpha parameter for the “cool” model 134
6.17 Space-time plots of temperature for the “cool” model 135

List of Tables

1.1 Physical components of a protoplanetary disc 8

4.1 Simulation runs for resolutions study 81
4.2 Turbulent stresses obtained with `CRONOS` 85
4.3 Turbulent stresses obtained with `ZEUS` 86

5.1 Overview of isothermal simulation runs 99

6.1 Summary of basic physical parameters for the “hot” model 109
6.2 Overview of simulation runs for the “hot” model 115
6.3 Summary of basic physical parameters for the “cool” model 129
6.4 Overview of simulation runs for the “cool” model. 130

A.1 Table of Physical and Astronomical Constants. 151

B.1 Table of Mathematical Symbols 153

Für meine Frau

Chapter 1: Introduction

At the time of the writing of the present work, more than 500 extrasolar planets (or “exoplanets” for short) have been discovered. They form a diverse “zoo” of bodies that cover a wide range of physical parameters (Fig. 1.1). Explaining the formation and the physical properties of such a diverse population of objects poses a difficult challenge to theorists working in the field of planet formation.

It is assumed that planets form in accretion discs around T Tauri stars, which for this reason are commonly termed “protoplanetary discs” (PPDs). The discovery of so many exoplanets over the last 15 years has lead to a great deal of activity in the research of protoplanetary discs. Improved observational methods have provided new data that helped to increase our understanding of the structure and composition of these objects. The Hubble space telescope delivered the first spatially resolved images taken at visible wavelengths (see Fig. 1.2). Protoplanetary discs are rather frequent, at least half of all protostars are surrounded by PPDs (McCaughrean and O’Dell, 1996).

Despite the significant advances on the observational side, the physics of protoplanetary accretion discs is still not well understood. Significant uncertainties remain both with respect to their physical composition as well as their temporal evolution. Their rather short lifetime of $\sim$10 Myr requires a physical process that transfers angular momentum outwards efficiently so that the matter can be accreted fast enough onto the star. Usually it is assumed that some sort of turbulence is acting in the disc, providing an effective viscosity that drives accretion (see Sec. 1.2). As of today, the most promising mechanism for this scenario is the *magnetorotational instability* (MRI), a powerful linear instability that exists in rotating, weakly magnetised shear flows and operates under very general conditions (see Sec. 2.3).

Protoplanetary discs are both cold and dense. This implies that they are for a large part optically thick, and therefore a realistic model should include radiation transport. The inclusion of radiation transport into theoretical models is not only necessary in order to achieve self-consistency, but it is also an important step towards the goal of comparing theory with observations by matching observed disc spectra with the results of numerical simulations. Since protoplanetary discs are cold objects that are for some part not well ionised, one should take into account also non-ideal magnetohydrodynamical effects like

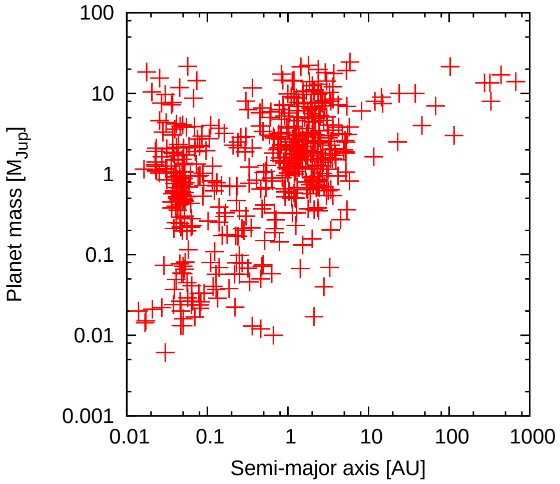

Fig. 1.1: Plot of semi-major axis versus planet mass for all known planets, as of Jan 2011. (Source: `www.exoplanets.eu`)

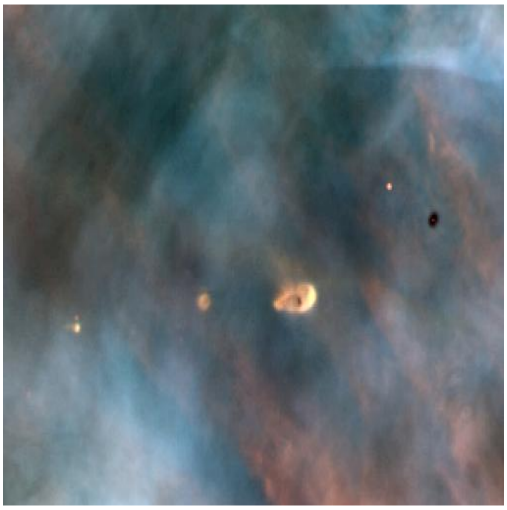

Fig. 1.2: Hubble view of the Orion nebula showing five young stars of which four are surrounded by “proplyds” (compact clouds of gas and dust that are supposed to harbour circumstellar discs). (Courtesy: NASA)

Ohmic resistivity. For the determination of the ionisation state it is necessary to include at least a small chemical network that contains the most important chemical reactions. A self-consistent model of magnetorotational turbulence in protoplanetary discs thus has to include magnetic fields, radiation transport and chemistry.

Up to now, there have been no protoplanetary disc simulations reported that model the magnetorotational turbulence in a self-consistent manner by including all these physical factors into one model. This lack of self-consistent turbulent disc models (and especially the lack of radiative models) was the main reason for carrying out the present research project. In this thesis, we describe the first fully radiative simulations of magnetorotational turbulence in protoplanetary discs. While we will concentrate our study mainly on the effects of radiation transport, we will also describe a few simulations that additionally include disc chemistry and are therefore applicable to colder regions of the disc where the ionisation level is small. We argue that such self-consistent numerical simulations are a very important field of research for the future and will help to constrain theoretical models by comparing the results of numerical simulations with actual observations.

1.1 Protostars and Protostellar Discs

1.1.1 Formation

According to the current theoretical understanding, stars are formed through the gravitational collapse of molecular cloud cores (Larson, 2003). Molecular cloud cores contain masses from $1\,M_\odot$ up to $10^4\,M_\odot$ and their size ranges from $L = 0.1\,\mathrm{pc}$ up to several pc. They are cool, with typical temperatures of order $\sim 10\,\mathrm{K}$, meaning that they consist mostly of molecular hydrogen H_2. The condition for gravitational instability is that the mass M of the cloud core exceeds the Jeans mass M_J, which is given by

$$M_\mathrm{J} = \frac{5k_\mathrm{B}TL}{\mu m_\mathrm{H} G}, \tag{1.1}$$

where k_B is the Boltzmann constant, μ is the mean molecular weight, m_H is the mass of hydrogen and G is the gravitational constant. Since at the start of the collapse the pressure is negligible, the initial collapse happens on the free-fall time scale

$$\tau_\mathrm{ff} = \sqrt{\frac{3\pi}{32G\rho}}. \tag{1.2}$$

As long as the system stays optically thin, the temperature will not change much and the Jeans mass will decrease during the collapse. This means that the collapse will continue on smaller scales and the system will fragment, leading to the formation of a system of multiple stars. The collapse is temporarily slowed down once the collapsing cloud becomes optically thick, since the system can then no longer efficiently get rid of its gravitational energy. The corresponding object is called the “first core”. As soon as the temperatures are high enough to allow for the dissociation of the molecular hydrogen, the collapse accelerates again, since now the system can effectively transfer its gravitational energy into the dissociation of H_2 molecules. This second collapse is stopped once the bulk of the matter is completely ionised, leading to the formation of the protostellar core. Because of angular momentum conservation, the collapse will in general lead to the formation of a disc-like structure around the protostar. The young stellar object (YSO) will continue to accrete matter from the surrounding disc for several million years until the disc is gone.

1.1.2 Classification

Young stellar objects can be divided into two groups, depending on their mass: Stars with masses bigger than $2\,M_\odot$ are called Herbig Ae/Be stars while those with masses below $2\,M_\odot$ are called T Tauri stars. Classical T Tauri stars (CTTS) have similar masses and effective temperatures as their main sequence counterparts, but they are more luminous since they do not yet have contracted to their final main sequence radii. The spectral energy distribution (SED) of T Tauri stars shows both an UV and an IR excess.[1] The UV excess stems from the accretion of matter onto the star, where matter is channeled along magnetic field lines onto a “hot spot” on the stellar surface. The IR excess comes from the surrounding disc, which is the characteristic signature through which a circumstellar discs reveals its existence (see Fig. 1.3 for a model SED of a protoplanetary disc).

Traditionally, protoplanetary discs are grouped into three categories according to the shape of their SED (Lada, 1987, see Fig. 1.4). Class I objects are discs where the *spectral index*

$$s = \frac{\mathrm{d}\log(\lambda F_\lambda)}{\mathrm{d}\log\lambda} \tag{1.3}$$

is positive. They correspond to very young objects deeply embedded in their parent molecular cloud. Class II objects are defined by

$$-2 < s < 0. \tag{1.4}$$

---

[1] In addition to the classical T Tauri stars there are also so-called weak lined T Tauri stars (WTTS) which lack the UV excess and show at best only a weak IR excess. These are believed to be more evolved systems where no or only a small residual disc is left.

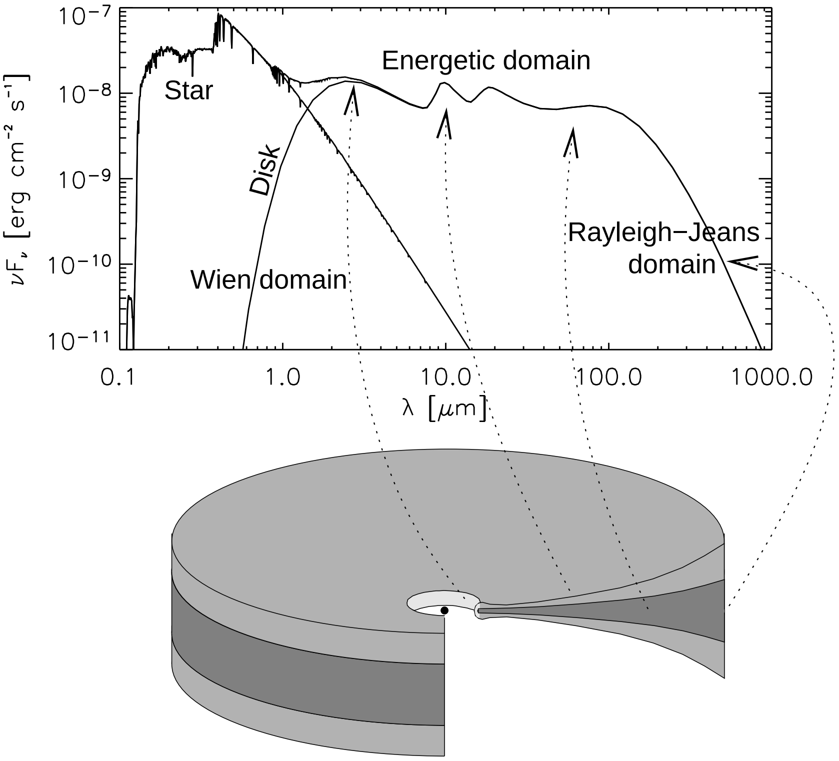

Fig. 1.3: Model SED, taken from Dullemond et al. (2007). The different wavelengths of the emitted radiation correspond to different locations in the disc. The near- and mid-infrared emission comes from the region near the inner rim, while the far-infrared emission corresponds to the outer disc regions.

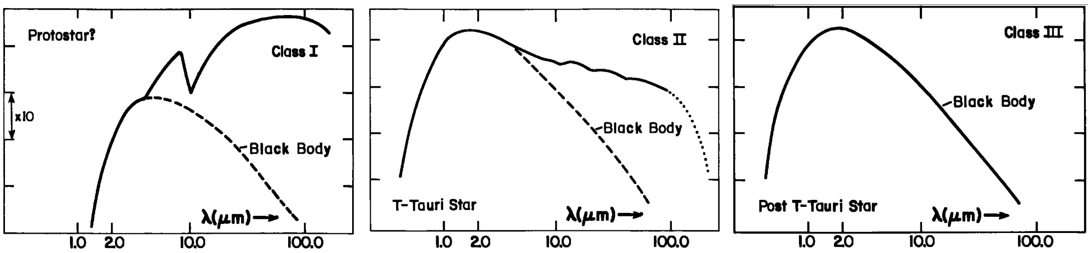

Fig. 1.4: Classification of protoplanetary discs according to Lada (1987). The young Class I objects show a strong IR excess and the protostar is still hidden in the parent molecular cloud. The older class II objects show a combination of stellar and disc spectrum, while class III objects can be modelled by a blackbody spectrum. (Taken from Lada, 1987, adapted.)

These correspond to objects of intermediate age in the T Tauri phase. Class III objects have a spectral index smaller than -2 and correspond to post T Tauri stars.

1.1.3 Typical Parameters

In this section we summarise the basic physical parameters of protoplanetary discs, namely the disc mass, temperature, size, magnetic field, accretion rate, lifetime and chemical composition. We will also discuss how these parameters are inferred from observations and theoretical arguments.

Disc Masses

Circumstellar discs are composed of gas and dust, with a dust-to-gas ratio of typically 1 %. Although the dust component is much smaller than the gas component, it dominates the opacity, and therefore the emission properties of the disc. Disc masses are usually inferred from sub-mm emission. At these wavelengths, the dust emission is optically thin, which means that the measured flux can be converted into a disc mass, once the dust opacity is known. The masses of protoplanetary discs that are obtained with this method are in the range of $10^{-4}\,M_\odot$ up to more than $0.1\,M_\odot$, with a typical mass being $10^{-2}\,M_\odot$ (Lodato, 2008).

Temperatures

The temperatures in protoplanetary discs, as inferred from the SED, range from a a few thousand K in the very inner regions down to a few 10 K in the outer parts. Note that the SED does not tell us from which radius the emission at a certain wavelength actually comes, which means that the temperature profile cannot be obtained directly from observations. Instead, it is obtained by fitting observational data to theoretical models (see, for example, Hueso and Guillot, 2005).

Disc Size & Density Profile

In order to determine the size of the disc, one has to spatially resolve it. This is possible with sub-mm interferometry (Dutrey et al., 1996; Andrews and Williams, 2007). Protoplanetary disc sizes obtained with this method range from several 100 AU up to 1000 AU. As is the case with the temperature, the density profile cannot be determined directly, but is instead obtained from a fit of the experimental data to theoretical models (Hueso and Guillot, 2005).

Magnetic Field

The observation of jets (Ferreira, 2008) is a strong argument in favor of the existence of significant magnetic fields in protoplanetary discs. Magnetic fields in protoplanetary discs may arise either from the frozen-in magnetic field of the parent molecular cloud or as a consequence of internal dynamo action, or through a combination of both.

The Zeeman splitting of OH in molecular cloud cores places a lower limit on the magnetic field of $\gtrsim 10$ mG in these objects (Wardle, 2007), which will likely be amplified during the collapse of the cloud core. Direct evidence for magnetic fields in protoplanetary discs comes from the observation of polarised sub-millimeter emission (Tamura et al., 1999), but see also Hughes et al. (2009), which is emitted by dust grains aligned with the magnetic field. Cho and Lazarian (2007) calculate a critical magnetic field of order $10 - 100$ mG for the grains to become aligned with the magnetic field.

Another constraint on the magnetic field in protoplanetary discs comes from the remanent magnetic field found in meteorites, if this field is interpreted as an imprint of the magnetic field in the solar nebula (King and Pringle, 2010). The data from meteorites suggests field strengths of the order of 1 Gauss at 1 AU (Levy and Sonett, 1978).[2] Finally, numerical simulations of magnetorotational turbulence (for example Flaig et al., 2010) also yield magnetic field strengths of this magnitude.

Accretion Rates & Disc Lifetime

There are mainly two methods to determine accretion rates: The first consists of measuring the strength of emission lines that are generated by the infall of disc gas, which is channeled along magnetic field lines, onto the star. The second makes use of the veiling (the ‘filling-in’) of photospheric absorption lines due to the accretion shock. Typical values for the accretion rate of discs around T Tauri stars are in the range of $10^{-9} - 10^{-7}\, M_\odot/\mathrm{y}$.

Disc lifetimes are usually determined by comparing the fraction of discs which show an infrared excess between young stellar clusters of different age. Typical lifetimes are in the range of $10^6 - 10^7\,\mathrm{y}$ (Hartmann et al., 1998; Sicilia-Aguilar et al., 2006).

Chemical Composition

As has already been mentioned, protoplanetary discs are made up mainly of gas and dust. Direct detection of the disc gas is difficult since the emission features are dominated by the dust grains. The most abundant molecule, H_2 is very difficult to observe due to

---

[2] Note, however, that the magnetic field in meteorites can alternatively be interpreted as being the result of an *internal* dynamo, rather than the product of external magnetic fields (Weiss et al., 2010).

Component	Description/Properties	Observational basis
Neutral gas	Mainly H_2. Mass fraction 99%.	molecular lines
Ions	Mainly alkali metals K^+, Na^+, ...	-
Free electrons	From ionisation of neutrals.	-
Photons	Wavelength 0.1-1000 µm.	direct detection
Magnetic fields	Field strengths of order ~ 1 G.	polarised sub-mm emission
Dust grains	µm-cm size, mass fraction $\sim 1\%$.	dust emission
Bigger objects	Pebbles, boulders, planet(esimal)s.	observation of planets

Tab. 1.1: Table showing the main physical constituents which make up a protoplanetary disc.

the lack of low excitation emission lines. The next most abundant molecule is CO, its abundance being $\sim 10^{-4}$ compared to molecular hydrogen. It can be detected through emission from rotational lines at mm wavelengths. All other molecules are much less abundant and very difficult to observe.

The ratio between dust and disc mass is usually assumed to something around 1%. Most of the emission that is observed comes from µm sized dust grains. However, there is observational evidence for grain growth up to mm and cm sizes Natta et al. (2007); Wilner et al. (2005); Isella et al. (2007).

The gas in protoplanetary discs will certainly be ionised to some degree since there are a number of ionisation sources present, such as stellar X-rays, cosmic rays or the decay of radionuclides. The most important ions will in general be K^+ and Na^+. Unfortunately, the question how the ionisation level varies as a function of position in the disc can not be answered from the observational side, and must instead be estimated from theoretical arguments. To summarise, Tab. 1.1 gives an overview of the main physical constituents of protoplanetary discs.

1.2 Phenomenological Accretion Disc Theory

1.2.1 Astrophysical Accretion Discs

In addition to protostellar systems, accretion discs are present also in a variety of other astrophysical objects, namely active galactic nuclei, binary X-ray sources and cataclysmic variables. The classical problem in the theory of accretion discs is why they are accreting, or, stated in other words, what is the mechanism which transports angular momentum outwards so that matter can spiral inwards? It cannot be ordinary molecular viscosity because it is several orders of magnitude too small to account for the observed accretion rates (Pringle, 1981, see also Sec. 2.2.1). Instead, it is usually assumed that accretion discs are turbulent and that it is the large kinematic viscosity associated with the turbulent motions in the disc that drives the outward angular momentum transport (Shakura and Sunyaev, 1973). This effect can be modelled phenomenologically by introducing an effective turbulent viscosity. Despite the remarkable success of such phenomenological models, the question of what mechanism could make the disc turbulent, however, still remains a matter of debate. We will later see (Sec. 2.3) that magnetorotational turbulence is the most likely driver of turbulent angular momentum transport in astrophysical accretion discs. In this introductory chapter, we will restrict ourselves to a simple phenomenological treatment of viscous accretion.

1.2.2 Theory of Viscous Accretion Discs

In the classical theory of viscous accretion discs (Pringle, 1981), the disc is described by the basic fluid dynamical equations, namely the continuity and the Navier-Stokes equations:

$$\frac{\partial \rho}{\partial t} + \boldsymbol{\nabla} \cdot (\rho \boldsymbol{v}) = 0, \tag{1.5a}$$

$$\frac{\partial \boldsymbol{v}}{\partial t} + \boldsymbol{v} \cdot \boldsymbol{\nabla} \boldsymbol{v} = -\frac{1}{\rho}(\boldsymbol{\nabla} p + \boldsymbol{\nabla} \cdot \sigma) - \boldsymbol{\nabla} \varPhi. \tag{1.5b}$$

where ρ is the density of the fluid, $\boldsymbol{v}$ the velocity, p is the pressure, σ is the stress tensor and $\varPhi$ the gravitational potential. The stress tensor contains the effect of viscous forces, which are assumed to be a consequence of turbulent motions in the disc.[3] The origin of the turbulence is, however, left open in the phenomenological theory. The most simple ad-hoc ansatz is to model it as a classical shear viscosity, i.e.

$$\sigma_{R\phi} = -\rho \nu \, R \frac{\mathrm{d}\varOmega}{\mathrm{d}R}, \tag{1.6}$$

where the angular orbital velocity $\varOmega = v_\phi / R$ and ν takes the place of the kinematic viscosity. All other components of the stress tensor are assumed to be zero. Neglecting the self-gravity of the disc, the gravitational potential is simply the gravitational potential of the central star:

$$\varPhi = -\frac{GM_\star}{r}. \tag{1.7}$$

---

[3] Note that although it is assumed that the accretion disc viscosity is of turbulent origin, classical viscous disc theory treats the flow as laminar. This means that the quantities appearing in Eqs. (1.5) should be considered as mean-field quantities that have been suitably averaged to smooth over the inhomogeneities created by the turbulence. See Sec. 2.2.2 for a further discussion.

We assume axisymmetry and switch to cylindrical coordinates (R, ϕ, z). Furthermore, for the case of circumstellar discs, we may in general assume that the disc is thin, which will lead us to consider vertically integrated quantities. We will now construct an approximate solution to Eqs. (1.5) by considering all three components of Eq. (1.5b) separately.

Rotation Profile

We start with the radial component of Eq. (1.5b). Assuming that the radial and vertical components of the velocity are negligible compared to the azimuthal component, we get:

$$\frac{\partial v_R}{\partial t} - \frac{v_\phi^2}{R} = -\frac{1}{\rho}\frac{\partial p}{\partial R} - \frac{GM_\star}{r^2}\,\hat{\boldsymbol{r}} \cdot \hat{\boldsymbol{R}}. \tag{1.8}$$

To first order, we can neglect $\partial v_R/\partial t$ as compared to the centrifugal term $-v_\phi^2/R$ and the pressure term $-\frac{1}{\rho}\frac{\partial P}{\partial R}$ as compared to the gravitational acceleration. Furthermore, we may (due to our assumption of a thin disc) set $\hat{\boldsymbol{r}} \cdot \hat{\boldsymbol{R}} \approx 1$, leading to

$$v_\phi^2 \approx \frac{GM_\star}{R} = \mathit{\Omega}_\mathrm{K}^2 R^2, \tag{1.9}$$

where we have defined the Keplerian angular velocity $\mathit{\Omega}_\mathrm{K}$ as

$$\mathit{\Omega}_\mathrm{K}^2 \equiv \frac{GM_\star}{R^3}. \tag{1.10}$$

This means that to first order, the velocity profile of the disc is described by a Keplerian rotation profile, which is a simple consequence of centrifugal balance. Discs that obey Eq. (1.9) are therefore called “Keplerian discs”.

Vertical Structure

Next, we consider the z-component of Eq. 1.5b. Since the disc is confined to the equatorial plane, we can to first order ignore motions in the vertical direction, which leads to

$$\frac{1}{\rho}\frac{\partial p}{\partial z} = -\frac{GM_\star}{r^2}\,\hat{\boldsymbol{r}} \cdot \hat{\boldsymbol{z}}. \tag{1.11}$$

Using $r \approx R$ and $\hat{\boldsymbol{r}} \cdot \hat{\boldsymbol{z}} = z/r \approx z/R$ yields

$$\frac{1}{\rho}\frac{\partial p}{\partial z} = -\frac{GM_\star}{R^2}\frac{z}{R}. \tag{1.12}$$

Assuming a constant temperature such that $p = \rho c_{\mathrm{s}}^2$, we arrive at

$$\frac{c_{\mathrm{s}}^2}{\rho}\frac{\partial \rho}{\partial z} = -\frac{GM_\star z}{R^3} = -\Omega_{\mathrm{K}}^2 z. \tag{1.13}$$

Defining the disc scale height H as $H \equiv c_{\mathrm{s}}/\Omega_{\mathrm{K}}$, we can write the solution to Eq. (1.13) as a Gaussian

$$\rho = \rho_0 \exp\left(-\frac{z^2}{2H^2}\right), \tag{1.14}$$

where ρ_0 is the density at the disc midplane. We note that the aspect ratio is just the ratio of the sound speed to the Keplerian velocity. This means that in order for the disc to be thin, the sound speed has to be significantly smaller than the Keplerian rotation speed.

Angular Momentum Transport

We finally turn to the azimuthal component of Eq. (1.5b). The vertically integrated version of this equation in cylindrical coordinates reads:

$$\Sigma\left(\frac{\partial V_\phi}{\partial t} + \frac{V_R V_\phi}{R} + V_R\frac{\partial V_\phi}{\partial R}\right) = -\frac{1}{R^2}\frac{\partial}{\partial R}(R^2 T_{R\phi}); \tag{1.15}$$

where Σ, the *surface density*, denotes the vertically integrated density,

$$\Sigma \equiv \int_{-\infty}^{\infty} \rho \,\mathrm{d}z, \tag{1.16}$$

$T_{R\phi}$ is the vertically integrated stress tensor,

$$T_{R\phi} \equiv \int_{-\infty}^{\infty} \sigma_{R\phi} \,\mathrm{d}z, \tag{1.17}$$

and V_R/V_ϕ are density-weighted mean values of the corresponding velocity components, i.e.

$$V_i \equiv \frac{1}{\Sigma}\int_{-\infty}^{\infty} \rho v_i \,\mathrm{d}z. \tag{1.18}$$

(Note that in the derivation of Eq. (1.15) we have made use of the fact that according to Eq. (1.9), v_ϕ does not depend on z, so that $V_\phi = v_\phi$). Analogously, the vertically integrated continuity equation becomes

$$\frac{\partial \Sigma}{\partial t} + \frac{1}{R}\frac{\partial}{\partial R}(R\Sigma V_R) = 0. \tag{1.19}$$

With the help of (1.19) we can write Eq. (1.15) in conservation form as

$$\frac{\partial}{\partial t}(\Sigma R V_\phi) + \frac{1}{R}\frac{\partial}{\partial R}[R^2(\Sigma V_R V_\phi + T_{R\phi})] = 0. \tag{1.20}$$

Written this form, Eq. (1.20) expresses angular momentum conservation, with $G(R) \equiv -RT_{R\phi}$ representing the torque exerted by viscous forces. Using Eq. (1.9) as well as Eq. (1.6), we obtain the radial velocity from Eq. (1.15):

$$v_R = \frac{\partial_R(R^2 T_{R\phi})}{R\Sigma\partial_R(Rv_\phi)} = -\frac{3}{\Sigma R^{1/2}}\frac{\partial}{\partial R}(\nu\Sigma R^{1/2}). \tag{1.21}$$

Insertion of this expression into the continuity equation, Eq. (1.19), results in an diffusion equation for the surface density,

$$\frac{\partial \Sigma}{\partial t} = \frac{3}{R}\frac{\partial}{\partial R}\left[R^{1/2}\frac{\partial}{\partial R}(\nu\Sigma R^{1/2})\right]. \tag{1.22}$$

This equation is the fundamental equation of viscous disc theory. The temporal evolution of the surface density is governed by one single parameter – the kinematic viscosity. However, since viscous disc theory is only a phenomenological theory, it can by itself not make any statements about the the nature or the magnitude of this effective viscosity.

Temperature Profile

We will now derive the temperature profile for a disc in a steady state, where the time derivatives in the continuity equation and the Navier-Stokes equation vanish. In the steady state, the continuity equation Eq. (1.19) reduces to

$$\dot{M} = 2\pi R v_R \Sigma, \tag{1.23}$$

with $\dot{M}$ being the constant mass accretion rate on to the star. Analogously, the angular momentum conservation equation Eq. (1.20) becomes

$$\dot{J} = \dot{M}\Omega R^2 - 3\pi\nu\Sigma\Omega R^2, \tag{1.24}$$

with $\dot{J}$ being the constant net flux of angular momentum. For small R, both terms on the right hand side of Eq. (1.24) become small. This implies that once we are far from the inner edge of the disc, $\dot{J}$ will be small compared to either of the the two terms on the right hand side and can be neglected, leading to

$$\dot{M} = 3\pi\nu\Sigma; \tag{1.25}$$

which is a very useful relation connecting the mass accretion rate, the viscosity and the surface density.[4] Note that Eq. (1.25) implies that in a steady state, the surface density and the viscosity are inversely proportional.

The energy that is locally dissipated through viscous torques per unit radial interval is given by

$$-G\Omega' = 2\pi R\nu\Sigma(R\Omega')^2 \overset{(1.9)}{=} \frac{9}{4}\nu\Sigma\Omega^{\cdot} \overset{(1.25)}{=} \frac{3GM_\star\dot{M}}{4\pi R^3} \tag{1.26}$$

Under the assumption that this power is radiated away locally, we can equate Eq. (1.26) with $2\sigma T_\mathrm{s}^4$, where σ is the Stefan-Boltzmann constant and T_s is the surface temperature (the factor of two coming from the fact that the disc has two sides), leading to

$$T_\mathrm{s}^4(R) = \frac{3GM\dot{M}}{8\pi\sigma R^3}. \tag{1.27}$$

Far from the disc's inner edge, the surface temperature thus has the characteristic scaling $T_\mathrm{s} \propto R^{-3/4}$. This relation, being simply a consequence of energy conservation, does not depend on the value of the viscosity ν. Note, however, that although this relation is often used, it is actually not well satisfied for real protoplanetary discs (Balbus, 2003).

1.3 Summary

Protoplanetary discs are disc-shaped structures around T Tauri stars in which planets are supposed to form. They are complicated objects in which many different physical mechanisms interact. The current picture that we have of these objects looks as follows:

- Protoplanetary discs form from the collapse of molecular cloud cores, where, due to angular momentum conservation, a disc-like structure forms around the young star. The matter in the disc is accreted onto the star in a time frame of ~10 My.
- The temporal evolution of protoplanetary discs is determined by some form of turbulence, which transports angular momentum outwards and powers the accretion process. The turbulence is likely of magnetic origin and connected with the magnetorotational instability (MRI).
- In the classical theory of viscous accretion discs, the (unknown) turbulence is parameterised as a turbulent viscosity. This phenomenological approach has proved

---

[4] Ultimately, $\dot{J}$ will be determined by the boundary condition at the inner edge of the disc. Using for example so-called "no-torque" conditions at the inner edge leads to $\dot{J} = \dot{M}(\Omega R^2)_\mathrm{in} = \dot{M}\sqrt{GMR_\mathrm{in}}$, resulting in the relation $3\pi\nu\Sigma = \dot{M}(1 - \sqrt{R_\mathrm{in}/R})$, which indeed reduces to Eq. (1.25) for $R \gg R_\mathrm{in}$.

> remarkably successful and provides the basic framework for interpreting observations of astrophysical accretion discs.

However, in order to make real progress towards understanding the nature of the turbulence in accretion discs and and also towards predicting the value of the turbulent viscosity, we must move towards a *microscopic* description of protoplanetary discs. Such a theory will have to start from the fundamental fluid-dynamical equations and it must identify an instability that has the desired properties. The rate of angular momentum transport that results from the instability can then be measured by means of numerical simulations and compared to astronomical observations. In the next chapter, we will derive the mathematical framework necessary for building such a theory.

Chapter 2: Protoplanetary Disc Physics

In the present chapter, we will have a more detailed look at the physics of protoplanetary discs. We will first derive the fundamental fluid-dynamical equations that govern the dynamics of the matter in a protoplanetary disc. Then we will have a look at how the viscous evolution of accretion discs can be described in terms of turbulent angular momentum transport. We will review the most important instability mechanisms, arguing that the magnetorotational instability is the most promising driver of angular momentum transport in protoplanetary discs.

2.1 Fundamental Fluid-dynamical Equations

Astrophysical plasmas (like the gas in protoplanetary discs) usually consist of a dilute mixture of atoms, molecules, ions and electrons. The time evolution of such a system can be described exactly by specifying the distribution function (the phase space density) which is evolved in time according to the Boltzmann equation. Luckily, such a cumbersome approach is usually not necessary, instead, in most cases one can use a much simpler, statistical description of the plasma which is obtained by taking successively higher moments of the Boltzmann equation, leading to the familiar equations of hydrodynamics. The criterion for this approach to work is that the mean free path of a particle is smaller than the length scale of the system under consideration, a condition that does hold for protoplanetary discs (see Sec. 2.2). As we will see, this means that we can describe the gas in protoplanetary discs by the equations of magnetohydrodynamics (MHD).

We start from a multifluid approach, describing the matter in protoplanetary discs as a mixture of four different fluids, namely:

1. Neutrals (mainly H_2), denoted by ‘n’.

2. Ions (K^+, Na^+, …), denoted by ‘I’.

3. Free electrons, denoted by ‘e’.
4. Small (∼ µm sized) dust grains. We allow our model to contain dust species of different sizes, which we denote by ‘d_1’, ‘d_2’, …, ‘$\mathrm{d}_{n_\mathrm{dust}}$’, where n_dust is the number of dust species that we want to model.

To a good approximation, each of of the four species is separately conserved Balbus (2009)[1] and obeys a mass conservation equation, i.e.

$$\frac{\partial \rho_s}{\partial t} + \boldsymbol{\nabla} \cdot (\rho_s \boldsymbol{v}_s) = 0, \tag{2.1}$$

where $s \in \{\mathrm{n}, \mathrm{I}, \mathrm{e}, \mathrm{d}_1, \mathrm{d}_2, \ldots, \mathrm{d}_{n_\mathrm{dust}}\}$. Denoting the (mean) number of ionisations per ion with Z and treating the dust as a pressureless uncharged fluid, the equations of motions for the different species become

$$\rho_\mathrm{n} \frac{\partial \boldsymbol{v}_\mathrm{n}}{\partial t} + \rho_\mathrm{n} \boldsymbol{v}_\mathrm{n} \cdot \boldsymbol{\nabla} \boldsymbol{v}_\mathrm{n} + \boldsymbol{\nabla} p_\mathrm{n} - \rho_\mathrm{n} \boldsymbol{\nabla} \mathit{\Phi} = \boldsymbol{f}_\mathrm{In} + \boldsymbol{f}_\mathrm{en} + \textstyle\sum_i \boldsymbol{f}_{\mathrm{d}_i\mathrm{n}}, \tag{2.2a}$$

$$\rho_\mathrm{I} \frac{\partial \boldsymbol{v}_\mathrm{I}}{\partial t} + \rho_\mathrm{I} \boldsymbol{v}_\mathrm{I} \cdot \boldsymbol{\nabla} \boldsymbol{v}_\mathrm{I} + \boldsymbol{\nabla} p_\mathrm{I} - \rho_\mathrm{I} \boldsymbol{\nabla} \mathit{\Phi} = Zen_\mathrm{I} \Big(\boldsymbol{E} + \frac{\boldsymbol{v}_\mathrm{I}}{c} \times \boldsymbol{B} \Big) + \boldsymbol{f}_\mathrm{nI} + \boldsymbol{f}_\mathrm{eI} + \textstyle\sum_i \boldsymbol{f}_{\mathrm{d}_i\mathrm{I}}, \tag{2.2b}$$

$$\rho_\mathrm{e} \frac{\partial \boldsymbol{v}_\mathrm{e}}{\partial t} + \rho_\mathrm{e} \boldsymbol{v}_\mathrm{e} \cdot \boldsymbol{\nabla} \boldsymbol{v}_\mathrm{e} + \boldsymbol{\nabla} p_\mathrm{e} - \rho_\mathrm{e} \boldsymbol{\nabla} \mathit{\Phi} = -en_\mathrm{e} \Big(\boldsymbol{E} + \frac{\boldsymbol{v}_\mathrm{e}}{c} \times \boldsymbol{B} \Big) + \boldsymbol{f}_\mathrm{ne} + \boldsymbol{f}_\mathrm{Ie} + \textstyle\sum_i \boldsymbol{f}_{\mathrm{d}_i\mathrm{e}}, \tag{2.2c}$$

$$\rho_{\mathrm{d}_i} \frac{\partial \boldsymbol{v}_{\mathrm{d}_i}}{\partial t} + \rho_{\mathrm{d}_i} \boldsymbol{v}_{\mathrm{d}_i} \cdot \boldsymbol{\nabla} \boldsymbol{v}_{\mathrm{d}_i} - \rho_{\mathrm{d}_i} \boldsymbol{\nabla} \mathit{\Phi} = \boldsymbol{f}_{\mathrm{nd}_i} + \boldsymbol{f}_{\mathrm{Id}_i} + \boldsymbol{f}_{\mathrm{ed}_i} + \textstyle\sum_{j \neq i} \boldsymbol{f}_{\mathrm{d}_j\mathrm{d}_i}; \tag{2.2d}$$

where the index i runs from 1 to n_dust and $\boldsymbol{f}_{s_1 s_2}$ denotes the force that species s_1 exerts on species s_2. Note that charge neutrality demands

$$n_\mathrm{e} = Zn_\mathrm{I}, \tag{2.3}$$

and because of Newtons third law, we have the relations $\boldsymbol{f}_\mathrm{In} = -\boldsymbol{f}_\mathrm{nI}$, $\boldsymbol{f}_\mathrm{en} = -\boldsymbol{f}_\mathrm{ne}$, … and so on. Since in protoplanetary discs, the neutral particles are by far the dominant species, we can in general neglect $\sum_i \boldsymbol{f}_{\mathrm{d}_i\mathrm{n}}$ in Eq. (2.2a), $\boldsymbol{f}_\mathrm{eI}$ and $\sum_i \boldsymbol{f}_{\mathrm{d}_i\mathrm{I}}$ in Eq. (2.2b), $\boldsymbol{f}_\mathrm{Ie}$ and $\sum_i \boldsymbol{f}_{\mathrm{d}_i\mathrm{e}}$ in Eq. (2.2c) and $\boldsymbol{f}_{\mathrm{Id}_i}$, $\boldsymbol{f}_{\mathrm{ed}_i}$ and $\sum_{j\neq i} \boldsymbol{f}_{\mathrm{d}_j\mathrm{d}_i}$in Eqs. (2.2d). This means that we only need to provide explicit expressions for $\boldsymbol{f}_\mathrm{ne}$, $\boldsymbol{f}_\mathrm{nI}$ and $\boldsymbol{f}_{\mathrm{nd}_i}$. We express $\boldsymbol{f}_\mathrm{ne}$ as

$$\boldsymbol{f}_\mathrm{ne} = n_\mathrm{e} m_\mathrm{e} \nu_\mathrm{en} (\boldsymbol{v}_\mathrm{n} - \boldsymbol{v}_\mathrm{e}), \tag{2.4}$$

---

[1] This is, of course, not exactly true, since for example the number of electrons may be subject to changing chemical conditions, and the number of small dust grains may decrease during the disc’s evolution as a consequence of grain growth.

with ν_{en} denoting the collision frequency between electrons and neutrals. Next, we write $\boldsymbol{f}_{\mathrm{In}}$ in the form

$$\boldsymbol{f}_{\mathrm{nI}} = \rho_{\mathrm{n}}\rho_{\mathrm{I}}\gamma\,(\boldsymbol{v}_{\mathrm{n}} - \boldsymbol{v}_{\mathrm{I}}), \tag{2.5}$$

where the *drag coefficient* $\gamma = 3 \times 10^{13}\,\mathrm{cm}^3\,\mathrm{s}^{-1}$ (Balbus, 2009). Finally, the drag force that the gas exerts on the dust can be written as

$$\boldsymbol{f}_{\mathrm{nd}_i} = \rho_{\mathrm{d}_i}\frac{\boldsymbol{v}_{\mathrm{n}} - \boldsymbol{v}_{\mathrm{d}_i}}{\tau_i}, \tag{2.6}$$

where τ_i is the *stopping time* for dust species d_i. Small dust particles, whose size a is smaller than 4/9 the gas mean free path, λ_{mfp}, belong to the so-called Epstein regime, with a stopping time given by

$$\tau^{\mathrm{Ep}} = \frac{\rho_s a}{\rho_{\mathrm{n}} c_s}, \tag{2.7}$$

where ρ_s is the material density of the dust particles. For dust particles that are bigger, but still small enough so that the Reynolds number of the flow past the particle, $\mathrm{Re} = 4a|\boldsymbol{v}_{\mathrm{d}} - \boldsymbol{v}_{\mathrm{n}}|/(c_{\mathrm{s}}\lambda_{\mathrm{mfp}})$, is smaller than one, have a stopping time according to Stokes' law:

$$\tau^{\mathrm{St}} = \frac{4\rho_{\mathrm{s}} a^2}{9\rho_{\mathrm{n}} c_s \lambda_{\mathrm{mfp}}}. \tag{2.8}$$

For still larger particles, the fluid description breaks down (see Youdin and Goodman, 2005).

As has been discussed in the previous chapter, protoplanetary discs are likely to be magnetised. In order to incorporate magnetic fields into our mathematical model, we further have to add Maxwell's equations to our Eqs. (2.1) and (2.2). The solution of the resulting system of equations would be a formidable task. However, since the neutral particles make up the bulk of the matter in protoplanetary discs, we can concentrate on this species. Our next aim will therefore be to derive a closed system of equations describing the evolution of the neutral particles.

2.1.1 The Equation of Motion for the Neutral Particles

Summing Eqs. (2.2a)-(2.2c) and neglecting the terms on the left hand side of Eqs. (2.2b)-(2.2c) against the corresponding terms in Eq. (2.2a), we obtain the following equation of motion for the neutral particles:

$$\rho_{\mathrm{n}}\frac{\partial \boldsymbol{v}_{\mathrm{n}}}{\partial t} + \rho\boldsymbol{v}_{\mathrm{n}}\cdot\boldsymbol{\nabla}\boldsymbol{v}_{\mathrm{n}} = -\boldsymbol{\nabla}p_{\mathrm{n}} + \frac{\boldsymbol{J}}{c}\times\boldsymbol{B} + \rho_{\mathrm{n}}\boldsymbol{\nabla}\mathit{\Phi}, \tag{2.9}$$

where we have introduced the current density

$$\boldsymbol{J} \equiv e n_{\mathrm{e}} \left(\boldsymbol{v}_{\mathrm{I}} - \boldsymbol{v}_{\mathrm{e}}\right). \tag{2.10}$$

As a result of the collisional coupling, the neutrals behave just as if they were a charged gas. We can now use the second Maxwell equation to express the current density $\boldsymbol{J}$ via the magnetic field $\boldsymbol{B}$:

$$\frac{1}{c}\frac{\partial \boldsymbol{E}}{\partial t} + \boldsymbol{\nabla} \times \boldsymbol{B} = \frac{4\pi}{c}\boldsymbol{J}. \tag{2.11}$$

The displacement current $(1/c)\partial \boldsymbol{E}/\partial t$ is a term of order v^2/c^2 and should be neglected in non-relativistic MHD. Therefore, the current density becomes:

$$\boldsymbol{J} = \frac{c}{4\pi}\boldsymbol{\nabla} \times \boldsymbol{B}. \tag{2.12}$$

Neglecting from now on the subscript ‘n’, we obtain the equations of motion for the neutral particles in their final form:

$$\frac{\partial \rho}{\partial t} + \boldsymbol{\nabla} \cdot (\rho \boldsymbol{v}) = 0, \tag{2.13a}$$

$$\rho\frac{\partial \boldsymbol{v}}{\partial t} + \rho \boldsymbol{v} \cdot \boldsymbol{\nabla} \boldsymbol{v} = -\boldsymbol{\nabla} p + \frac{(\boldsymbol{\nabla} \times \boldsymbol{B}) \times \boldsymbol{B}}{4\pi} + \rho \boldsymbol{\nabla} \Phi. \tag{2.13b}$$

Note that the Lorentz force can be decomposed according to

$$\frac{(\boldsymbol{\nabla} \times \boldsymbol{B}) \times \boldsymbol{B}}{4\pi} = \boldsymbol{\nabla}\left(\frac{B^2}{8\pi}\right) - \frac{\boldsymbol{B} \cdot \boldsymbol{\nabla} \boldsymbol{B}}{4\pi}, \tag{2.14}$$

where the first term of on the right hand side corresponds to the gradient of the magnetic pressure $P_{\mathrm{mag}} = B^2/8\pi$ and the second to the magnetic stress.

2.1.2 Evolution of the Magnetic Field

In order to derive an equation for the evolution of the magnetic field, we start by looking at Faraday’s law,

$$\frac{1}{c}\frac{\partial \boldsymbol{B}}{\partial t} + \boldsymbol{\nabla} \times \boldsymbol{E} = 0. \tag{2.15}$$

We calculate $\boldsymbol{\nabla} \times \boldsymbol{E}$ with the help of the equation of motion for the electrons, Eq. (2.2c). For a weakly ionised gas, this equation reduces to

$$\boldsymbol{f}_{\mathrm{ne}} \approx e n_{\mathrm{e}} \left(\boldsymbol{E} + \frac{\boldsymbol{v}_{\mathrm{e}}}{c} \times \boldsymbol{B}\right). \tag{2.16}$$

The justification for this is that the ratio of the inertial terms to the Lorentz force can be estimated to be

$$\left|\rho_{\mathrm{e}}\frac{\mathrm{D}\boldsymbol{v}_{\mathrm{e}}}{\mathrm{D}t}\Big/ en_{\mathrm{e}}\left(\boldsymbol{E}+\frac{\boldsymbol{v}_{\mathrm{e}}}{c}\times\boldsymbol{B}\right)\right| \sim \frac{\rho_{\mathrm{e}}v_{\mathrm{e}}}{\Delta t}\frac{c}{en_{\mathrm{e}}v_{\mathrm{e}}B} = \frac{m_{\mathrm{e}}c}{eB}\Big/\Delta t \ll 1; \tag{2.17}$$

i.e. it is of the order of the ratio of the electron gyro-period to a macroscopic flow crossing time, denoted here by Δt. In protoplanetary discs, this quantity will usually be very small (Balbus, 2009); so the Lorentz and collisional terms will dominate all other terms and Eq. (2.16) will be an excellent approximation. Using Eq. (2.4), we can write the electric field $\boldsymbol{E}$ as

$$\boldsymbol{E} = -\frac{1}{c}[\boldsymbol{v}_{\mathrm{n}} + (\boldsymbol{v}_{\mathrm{e}} - \boldsymbol{v}_{\mathrm{I}}) + (\boldsymbol{v}_{\mathrm{I}} - \boldsymbol{v}_{\mathrm{n}})] \times \boldsymbol{B} - \frac{m_{\mathrm{e}}\nu_{\mathrm{en}}}{e}[(\boldsymbol{v}_{\mathrm{e}} - \boldsymbol{v}_{\mathrm{I}}) + (\boldsymbol{v}_{\mathrm{I}} - \boldsymbol{v}_{\mathrm{n}})]. \tag{2.18}$$

The term $\boldsymbol{v}_{\mathrm{I}} - \boldsymbol{v}$ in Eq. (2.18) is related to the momentum exchange rate between ions and neutrals $\boldsymbol{f}_{\mathrm{In}}$ via Eq. (2.5). Using the fact that in general $\boldsymbol{f}_{\mathrm{en}}$ will be small compared to $\boldsymbol{f}_{\mathrm{In}}$, we can write $\boldsymbol{v}_{\mathrm{I}} - \boldsymbol{v}_{\mathrm{n}}$ as

$$\boldsymbol{v}_{\mathrm{I}} - \boldsymbol{v}_{\mathrm{n}} = \frac{\boldsymbol{f}_{\mathrm{In}}}{\rho_{\mathrm{n}}\rho_{\mathrm{I}}\gamma} \approx \frac{\boldsymbol{J}\times\boldsymbol{B}}{c\rho_{\mathrm{n}}\rho_{\mathrm{I}}\gamma}. \tag{2.19}$$

It can be shown (Balbus, 2009) that the final term in Eq. (2.18) is small compared to the third term in this equation, i.e.

$$\frac{m_{\mathrm{e}}\nu_{\mathrm{en}}}{e}(\boldsymbol{v}_{\mathrm{I}} - \boldsymbol{v}_{\mathrm{n}}) \ll \frac{1}{c}(\boldsymbol{v}_{\mathrm{e}} - \boldsymbol{v}_{\mathrm{I}}) \times \boldsymbol{B}, \tag{2.20}$$

so it may be neglected. Using this fact, as well as Eq. (2.19), and Eq. (2.10), we may write the force balance equation for the electrons, Eq. (2.18), as

$$\boldsymbol{E} + \frac{\boldsymbol{v}_{\mathrm{n}}}{c}\times\boldsymbol{B} - \frac{\boldsymbol{J}\times\boldsymbol{B}}{en_{\mathrm{e}}c} + \frac{\boldsymbol{J}\times\boldsymbol{B}\times\boldsymbol{B}}{c^2\rho_{\mathrm{n}}\rho_{\mathrm{I}}\gamma} - \frac{\boldsymbol{J}}{\sigma_{\mathrm{cond}}} = 0, \tag{2.21}$$

where we have defined the electrical conductivity σ_{cond} as

$$\sigma_{\mathrm{cond}} = \frac{e^2 n_{\mathrm{e}}}{m_{\mathrm{e}}\nu_{\mathrm{en}}}. \tag{2.22}$$

Operating with $\boldsymbol{\nabla}\times$ on Eq. (2.21) and putting this into Faraday's law, Eq. (2.15), we obtain the following equation describing the self-induction of the magnetised gas:

$$\frac{\partial\boldsymbol{B}}{\partial t} = \boldsymbol{\nabla}\times\left[\underbrace{\boldsymbol{v}\times\boldsymbol{B}}_{\mathscr{I}}\underbrace{-\eta\boldsymbol{\nabla}\times\boldsymbol{B}}_{\mathscr{O}}\underbrace{-c\frac{\boldsymbol{\nabla}\times\boldsymbol{B}\times\boldsymbol{B}}{4\pi en_{\mathrm{e}}}}_{\mathscr{H}}\underbrace{+\frac{\boldsymbol{\nabla}\times\boldsymbol{B}\times\boldsymbol{B}\times\boldsymbol{B}}{4\pi\gamma\rho_{\mathrm{n}}\rho_{\mathrm{I}}}}_{\mathscr{A}}\right], \tag{2.23}$$

where we have introduced the resistivity η, which is related to the conductivity $\sigma_{\rm cond}$ via

$$\eta = \frac{c^2}{4\pi\sigma_{\rm cond}}. \tag{2.24}$$

The first term in Eq. (2.23) is the induction term ($\mathscr{I}$), the second is the ohmic resistivity ($\mathscr{O}$), the third corresponds to the Hall current ($\mathscr{H}$) and the fourth describes ambipolar diffusion ($\mathscr{A}$). The Hall term $\mathscr{H}$ (the ambipolar diffusion term $\mathscr{A}$) is present whenever the drift velocity between electrons and ions $\boldsymbol{v}_{\rm e} - \boldsymbol{v}_{\rm I}$ (the drift velocity between ions and neutrals $\boldsymbol{v}_{\rm I} - \boldsymbol{v}$) has a component perpendicular to the magnetic field.

2.1.3 Importance of Non-ideal MHD-effects

The scaling of the non-ideal MHD terms for an astrophysical gas goes as follows (Balbus, 2009):

$$\frac{\mathscr{A}}{\mathscr{H}} = Z \left(\frac{9 \times 10^{12}\,{\rm cm}^{-3}}{n}\right)^{1/2} \left(\frac{T}{10^3\,{\rm K}}\right)^{1/2} \left(\frac{v_{\rm A}}{c_{\rm s}}\right), \tag{2.25}$$

$$\frac{\mathscr{O}}{\mathscr{H}} = \left(\frac{n}{8 \times 10^{17}\,{\rm cm}^{-3}}\right)^{1/2} \left(\frac{c_{\rm s}}{v_{\rm A}}\right). \tag{2.26}$$

We see that for a weakly magnetised gas, ohmic dissipation will always be the dominant non-ideal term. For protoplanetary discs, the critical ionisation fraction for ideal MHD to be applicable is about 10^{-13} (Balbus, 2009). This means that actually for a large part of the disc, ideal MHD will be a very good approximation.

As has already been stated in the previous chapter, the turbulent angular momentum transport in protoplanetary disc is most likely due to hydromagnetic turbulence driven by the magnetorotational instability (MRI).[2] If this is true, then the level of turbulence (and the magnitude of angular momentum transport) at a certain location in the disc will depend on the ionisation level there. The ionisation level itself is determined by a balance between ionisation processes (namely thermal ionisation, ionisation due to stellar X-rays, cosmic rays and the decay of radionuclides) and recombination processes (the most important one being the sweeping-up of free charges by small dust grains). Since the recombination rate depends critically on the abundance of small dust grains (which is unknown), any estimate of the ionisaton profile of protoplanetary discs is highly uncertain.

Nevertheless, numerous analytical and numerical calculations (see Armitage, 2010, for a review) hint at the following picture (see Fig. 2.1):

---

[2] The MRI is discussed in some detail near the end of the present chapter, see Sec. 2.3.

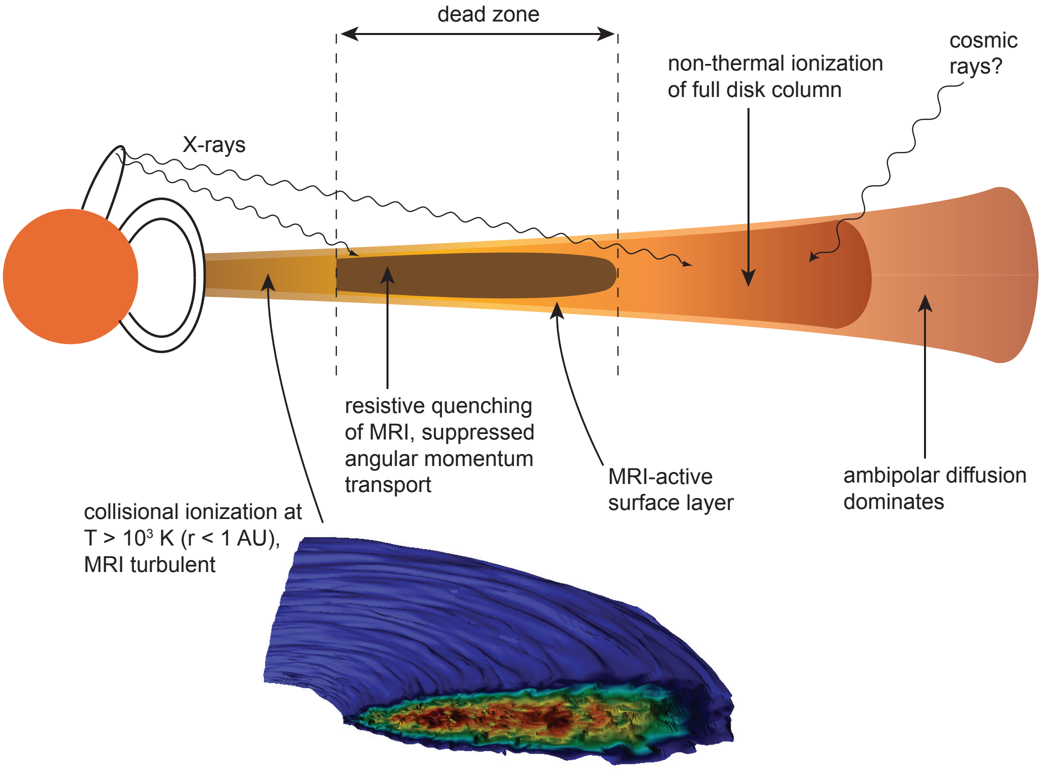
dead zone
cosmic rays?
non-thermal ionization of full disk column
X-rays
resistive quenching of MRI, suppressed angular momentum transport
MRI-active surface layer
ambipolar diffusion dominates
collisional ionization at T > 10³ K (r < 1 AU), MRI turbulent

Fig. 2.1: *Sketch of an MRI-turbulent protoplanetary disc.* The disc is consists of a thermally ionised, fully turbulent inner zone, an intermediate zone, where only the surface layers are turbulent, and an outer zone, which, is fully turbulent again. [Image taken from Armitage (2010)]

1. In the region near to the central star, the gas is hot enough ($T \geq 1000$ K) for collisional ionisation to be effective, forming a turbulent inner zone. The outer edge of this inner, active zone will lie somewhere between 0.1 and 5 AU, and moves inward with time as the disc's surface density decreases.
2. Next comes an intermediate region, where the midplane is cool enough, and well-enough shielded from the ionising radiation, so that near the midplane the hydromagnetic turbulence gets quenched by resisistivity, forming a so-called "dead zone". The upper layers may still show some turbulent activity and (weak) angular momentum transport.
3. Finally, there is an outer region, where the disc's surface density is low enough for the non-thermal ionisation sources (mainly stellar X-rays) to be effective, so the disc becomes fully turbulent again.

Since the location of the dead zone corresponds to the place where planetesimals are assumed to form, constraining the size of the dead zone and the level of turbulence in this region is a very important task for current research.

2.1.4 Thermodynamics

From now on, we will restrict ourselves to the region of a protoplanetary disc, where the ambipolar diffusion and Hall term can be neglected. Then, our set of equations, which describes the combined evolution of the neutral particles and the magnetic field looks as follows:

$$\frac{\partial \rho}{\partial t} + \boldsymbol{\nabla} \cdot (\rho \boldsymbol{v}) = 0, \tag{2.27a}$$

$$\rho \frac{\partial \boldsymbol{v}}{\partial t} + \rho \boldsymbol{v} \cdot \boldsymbol{\nabla} \boldsymbol{v} = -\boldsymbol{\nabla} p + \frac{(\boldsymbol{\nabla} \times \boldsymbol{B}) \times \boldsymbol{B}}{4\pi} + \rho \boldsymbol{\nabla} \Phi, \tag{2.27b}$$

$$\frac{\partial \boldsymbol{B}}{\partial t} = \boldsymbol{\nabla} \times (\boldsymbol{v} \times \boldsymbol{B} - \eta \boldsymbol{\nabla} \times \boldsymbol{B}) \tag{2.27c}$$

However, this system of equations is not yet closed, since we have not yet specified the pressure p. This means that we have to make some assumptions about the thermodynamics of the gas.

Isothermal Equation of State

The simplest possibility to close the set of equations (2.27) is to use a prescribed value for the sound speed $c_\mathrm{s}^2 = \partial p / \partial \rho$, from which the pressure immediately follows as

$$p = \rho c_\mathrm{s}^2. \tag{2.28}$$

This is identical to keeping the temperature fixed at some predefined value, since the two quantities are directly related via

$$c_\mathrm{s} = \sqrt{k_\mathrm{B} T / \mu m_\mathrm{H}}. \tag{2.29}$$

The closure Eq. (2.28) is often used in numerical simulations of magnetorotational turbulence in accretion discs. However it has the drawback that the temperature profile must be known (or guessed) in advance. Also it does not account for changes in the temperature profile due to varying turbulent activity.

Adiabatic Equation of State

If we want to determine the temperature in the disc self-consistently, rather than to prescribe it, we have to add the equation for the thermal energy e to our set of gas-dynamical equations (2.27). Neglecting the interaction between matter and radiation, the thermal energy equation reads:

$$\frac{\partial e}{\partial t} + \boldsymbol{\nabla} \cdot (e\boldsymbol{v}) = -p\boldsymbol{\nabla} \cdot \boldsymbol{v} + \frac{\eta}{4\pi}|\boldsymbol{\nabla} \times \boldsymbol{B}|^2, \tag{2.30}$$

where the first term on the r.h.s. describes the change in thermal energy due to compression or expansion of the fluid and the second term describes the Ohmic heating. For an ideal gas, e and p are related via

$$e = p/(\gamma - 1). \tag{2.31}$$

Note that this ansatz is not well suited for simulations of magnetorotational turbulence: Since no form of cooling is prescribed, the turbulent dissipation will lead to rapid secular heating of the disc. In an optically thin gas, this problem can be cured by adding a cooling function (Brandenburg et al., 1995), but for the optically thick protoplanetary discs this is very unrealistic. For a realistic description of protoplanetary discs, one needs to include radiation transport.

Radiation Transport

For the most part of a protoplanetary disc, the radiation pressure is negligible compared to the gas pressure, so we need not to include the radiation pressure in the equation of motion, Eq. (2.27b). Including the interaction between matter and radiation, the thermal energy equation becomes:

$$\frac{\partial e}{\partial t} + \boldsymbol{\nabla} \cdot (e\boldsymbol{v}) = -p\boldsymbol{\nabla} \cdot \boldsymbol{v} + \frac{\eta}{4\pi}|\boldsymbol{\nabla} \times \boldsymbol{B}|^2 - \kappa_\mathrm{P}\rho(4\pi B - cE), \tag{2.32}$$

where E is the radiation energy and κ_{P} is the Planck mean opacity. Furthermore, we must add the radiation energy equation

$$\frac{\partial E}{\partial t} + \boldsymbol{\nabla}(E\boldsymbol{v}) = -\frac{E}{3}\boldsymbol{\nabla}\cdot\boldsymbol{v} + \kappa_{\mathrm{P}}\rho(4\pi B - cE) - \boldsymbol{\nabla}\cdot\boldsymbol{F}, \tag{2.33}$$

where $\boldsymbol{F}$ is the radiative energy flux. We close our system of equations by employing a flux-limited diffusion approach which consists of writing $\boldsymbol{F}$ as

$$\boldsymbol{F} = -\frac{\lambda c}{\kappa\rho}\boldsymbol{\nabla}E, \tag{2.34}$$

where λ is the so-called flux limiter, for which we use the form as given in Levermore and Pomraning (1981). In the optically thick limit, where

$$\frac{\boldsymbol{\nabla}E}{E} \ll \kappa\rho, \tag{2.35}$$

the flux limiter becomes $\lambda = 1/3$ which is the exact expression in this limit. In the optically thin limit, where

$$\frac{\boldsymbol{\nabla}E}{E} \gg \kappa\rho, \tag{2.36}$$

the flux limiter becomes

$$\lambda = \frac{\kappa\rho E}{|\boldsymbol{\nabla}E|}, \tag{2.37}$$

As a result, the flux is then

$$\boldsymbol{F} = cE\frac{\boldsymbol{\nabla}E}{|\boldsymbol{\nabla}E|}, \tag{2.38}$$

which is the correct physical expression in the optically thin limit, where photons stream freely. In between, the flux limiter extrapolates between the optically thick and the optically thin regimes, and the solution will only be approximately correct.

One-temperature approximation

When considering protoplanetary discs, we can make use of the fact that in most part of the disc, radiation and matter are closely coupled and therefore in thermodynamic equilibrium. This means that the radiation energy can be expressed in terms of the gas temperature according to the following relation:

$$E = aT^4, \tag{2.39}$$

where a is the radiation constant. When using the relation Eq. (2.39), we do no longer need to solve the equation for the radiation energy. Instead we add the radiation energy equation, Eq. (2.33) to the thermal energy equation, Eq. (2.32), which yields, after making use of $E \ll e$,

$$\frac{\partial e}{\partial t} + \boldsymbol{\nabla} \cdot (e\boldsymbol{v}) = -p\boldsymbol{\nabla} \cdot \boldsymbol{v} - \boldsymbol{\nabla} \cdot \boldsymbol{F}. \tag{2.40}$$

Since $\boldsymbol{F}$ can now be written as

$$\boldsymbol{F} = -\frac{\lambda c}{\kappa\rho}\boldsymbol{\nabla} a T^4 = -4aT^3 \frac{\lambda c}{\kappa\rho}\boldsymbol{\nabla} T, \tag{2.41}$$

with the radiation energy no longer appearing.

2.1.5 Final Set of Equations

To summarise, we will restrict ourselves to the planet forming region inside the first ten AU, where the Hall term and ambipolar diffusion can be neglected, yielding the following set of equations:

$$\frac{\partial \rho}{\partial t} + \boldsymbol{\nabla} \cdot (\rho\boldsymbol{v}) = 0, \tag{2.42a}$$

$$\rho\frac{\partial \boldsymbol{v}}{\partial t} + \rho\boldsymbol{v} \cdot \boldsymbol{\nabla}\boldsymbol{v} = -\boldsymbol{\nabla} p + \frac{(\boldsymbol{\nabla} \times \boldsymbol{B}) \times \boldsymbol{B}}{4\pi} + \rho\boldsymbol{\nabla}\Phi, \tag{2.42b}$$

$$\frac{\partial \boldsymbol{B}}{\partial t} = \boldsymbol{\nabla} \times (\boldsymbol{v} \times \boldsymbol{B} - \eta\boldsymbol{\nabla} \times \boldsymbol{B}), \tag{2.42c}$$

$$\frac{\partial e}{\partial t} + \boldsymbol{\nabla} \cdot (e\boldsymbol{v}) = -p\boldsymbol{\nabla} \cdot \boldsymbol{v} + \frac{\eta}{4\pi}|\boldsymbol{\nabla} \times \boldsymbol{B}|^2 - \boldsymbol{\nabla} \cdot \boldsymbol{F}, \tag{2.42d}$$

$$\boldsymbol{F} = -4aT^3\frac{\lambda c}{\kappa\rho}\boldsymbol{\nabla} T, \quad e = p/(\gamma - 1). \tag{2.42e}$$

This set of radiation-magnetohydrodynamics equations form the basis for most of the calculations carried out in the present work.

2.2 Accretion Disc Viscosity

2.2.1 Molecular Viscosity vs. Turbulent Viscosity

In the phenomenological disc theory, the kinematic viscosity ν is nothing more than a phenomenological parameter for which we have yet to put up a physical explanation. On thing that can be made clear immediately, is that it cannot be the ordinary molecular viscosity $\nu_{\rm mol}$, because the Reynolds numbers in accretion discs are much to high to explain the observed accretion rates (Pringle, 1981; Balbus, 2003). This can be seen by calculating the Reynolds number

$$\mathrm{Re} = \frac{R^2 \Omega}{\nu_{\rm mol}}. \tag{2.43}$$

The physical origin for molecular viscosity is the diffusion of molecules across fluid layers moving at different velocities (see Fig. 2.2 a). The magnitude of the molecular viscosity is given by the product of the collisional mean free path $\ell = 1/n\sigma_{\rm coll}$ (with n the number density and $\sigma_{\rm coll}$ the collisional cross section) and the random velocity $v_{\rm therm} \sim c_{\rm s}$:

$$\nu_{\rm mol} = v_{\rm therm} \ell \tag{2.44}$$

The number density is

$$n = \frac{\rho}{\mu m_{\rm H}} \sim \frac{\Sigma / H}{m_{\rm H}}, \tag{2.45}$$

since the mean molecular weight μ is of order one. Thus we can estimate (using $H = c_{\rm s}/\Omega$) the Reynolds number to be of order

$$\mathrm{Re} = \frac{\Sigma \sigma_{\rm coll}}{m_{\rm H}} \left(\frac{H}{R}\right)^{-2} = 10^{14} \times \left(\frac{\Sigma}{100\,{\rm g cm^{-2}}}\right) \left(\frac{H}{R}\right)^{-2}, \tag{2.46}$$

after inserting the hydrogen mass $m_{\rm H} \approx 10^{-24}\,$g and the geometrical cross section of the hydrogen molecule $\sigma_{\rm coll} \approx 10^{-16}\,{\rm cm}^2$. For a typical aspect ratio of $H/R \sim 0.1$ and a typical surface density of $\Sigma \sim 100\,{\rm g cm^{-2}}$ at a distance of ~ 10 AU, we thus get a Reynolds number of $\mathrm{Re} \sim 10^{12}$! From the fact that the dynamical timescale is of the order of years, this implies that the accretion process would take many billions of years, which contradicts the observational results mentioned in the previous chapter. Therefore, there must be some other mechanism that drives the accretion process in protoplanetary discs. This unknown mechanism is sometimes referred to as *anomalous* viscosity.

As has already been stated in the previous chapter, turbulent motions within the disc are the most likely source for anomalous viscosity. The mechanism of turbulent angular momentum transport can be understood as follows: Given that our disc is turbulent, then the accretion process is no longer dominated by the dynamics of individual atoms and molecules with their corresponding molecular viscosity, but instead it is the dynamics of the turbulent eddies with their much larger turbulent viscosity $\nu_{\rm turb}$ that will determine the strength of the angular momentum transport (Fig. 2.2 b). We can estimate the

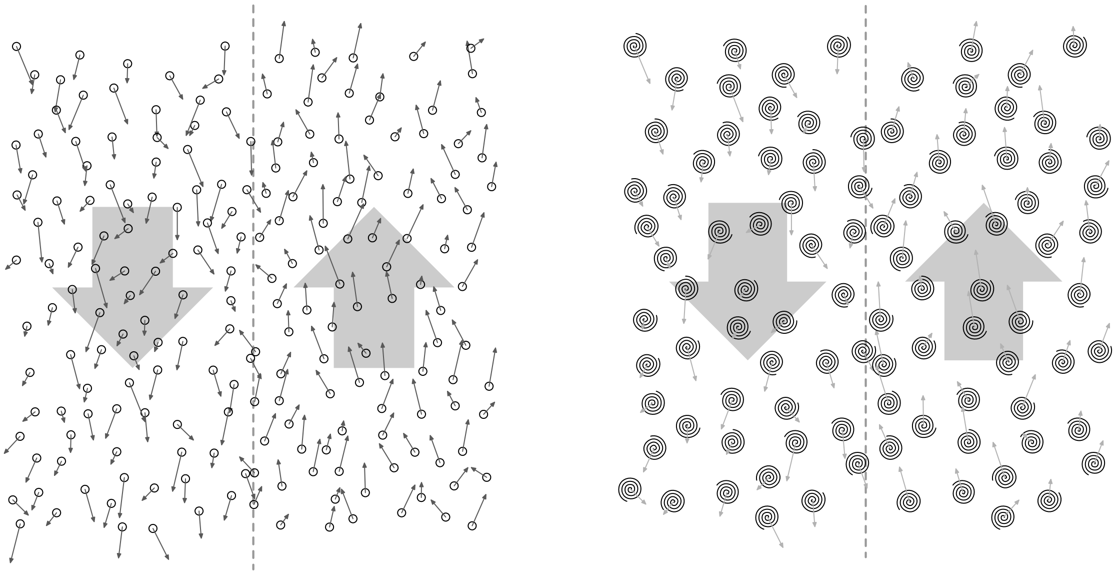

(a) Molecular viscosity: $\nu = v_{\rm th}\lambda \Rightarrow {\rm Re} \gtrsim \mathcal{O}(10^{12})$. (b) Eddy viscosity: $\nu \sim c_{\rm s}L \Rightarrow {\rm Re}_{\rm turb} \sim 10^{-10}{\rm Re}$.

Fig. 2.2: Schematic plot of two fluid layers moving at different speeds. The diffusion of molecules from one layer to the other leads to the transport of momentum between the layers, thus reducing the velocity difference between them (left panel). In astrophysical accretion discs, the friction that is generated in this way is more or less negligible, because the mean free path over which the molecules diffuse is very small compared to the size of the whole system. If, on the other hand, the flow is turbulent, then the diffusion of turbulent eddies will provide much stronger viscous forces between the two fluid layers (right panel). Since the mean free path of the eddies will likely be of the same order as the typical length scale of the system (i.e. the pressure scaleheight) this process will generate a *turbulent* viscosity that many orders of magnitude larger than the molecular viscosity of the gas.

magnitude of the eddy viscosity in the same manner as we did for the molecular viscosity. The collisional mean free path of the turbulent eddies can be taken to be of the order of the disc scale height H, while the random velocity of the turbulent eddies must be smaller than the sound speed c_s,[3] leading to

$$\nu_\mathrm{turb} = \alpha c_\mathrm{s} H, \tag{2.47}$$

where the dimensionless parameter α satisfies

$$\alpha \lesssim 1. \tag{2.48}$$

The parametrisation Eq. (2.47) is the basis for so-called alpha models of accretion discs and was introduced by Shakura and Sunyaev (1973). Using this equation, we can calculate the turbulent Reynolds number $\mathrm{Re}_\mathrm{turb}$,

$$\mathrm{Re}_\mathrm{turb} = \frac{R^2 \varOmega}{\alpha c_\mathrm{s} H} = \frac{1}{\alpha} \left(\frac{H}{R} \right)^{-2}, \tag{2.49}$$

If we now consider a disc with an aspect ratio of 0.1, and take the dynamical timescale to be in the range of 10-100 y, then α should be of order 10^{-3} in order to produce the observed accretion timescales of 1-10 My. We see that the assumption of turbulent disc does indeed have the potential to explain the large accretion rates observed. However, in order to make further progress, we first have to establish the connection between the unknown alpha parameter and the dynamics of the underlying turbulence.

2.2.2 Dynamical Foundation of Accretion Disc Viscosity

As has already been mentioned, classical viscous disc theory can be interpreted in terms of a mean field theory. By suitably averaging the fundamental fluid-dynamical equations, we can obtain mean-field equation of the same form as used in the phenomenological disc theory described in Sec. 1.2.2, with the stress tensor being a function of the correlated fluctuations that live atop the background mean flow.

The question is how to define a suitable average. Since we are dealing with a disc, it is certainly sensible to perform an average in the azimuthal direction. If the disc is thin, as is the case for protoplanetary discs, it is natural to also integrate the equations in the vertical direction. Because of the turbulence, the azimuthally and vertically averaged profile will likely still show significant spatial and temporal variations. This suggests to perform also a smoothing in the radial direction, leading to the sort of averaging procedure as proposed for example by Balbus (2003):

---

[3] If the turbulence were supersonic, we would have strong dissipation by shocks, which would make the turbulence subsonic. Therefore, the sound speed poses an upper limit on the velocity of the turbulent eddies.

$$\langle \bullet \rangle^{\mathrm{Balbus}} = \frac{1}{2\pi \Delta R} \int_{R-\Delta R/2}^{R+\Delta R/2} \int_0^{2\pi} \int_{-\infty}^{\infty} \bullet \, \mathrm{d}R \, \mathrm{d}\phi \, \mathrm{d}z. \tag{2.50}$$

The smoothing length scale ΔR must be small compared to R but large compared to the length scale of the turbulence, i.e. the pressure scale height H. If such a separation of length scales does not exist, one may alternatively also perform a time average, or, as a last resort, employ an ensemble average.

Let us now assume that a suitable average exists, and let us denote it by $\langle \bullet \rangle$. We operate with this average on the azimuthal component of the momentum equation Eq. (2.27b), which, in cylindrical coordinates, reads

$$\begin{aligned} &\frac{\partial}{\partial t}(\rho R v_\phi) + \frac{1}{R}\frac{\partial}{\partial R}\left[R^2\left(\rho v_R v_\phi - \frac{B_R B_\phi}{4\pi}\right)\right] \\ &\qquad + \frac{1}{R}\frac{\partial}{\partial \phi}\left[R\left(\rho v_\phi^2 + P + \frac{B_R^2 + B_z^2}{8\pi}\right)\right] + \frac{\partial}{\partial z}\left[R\left(\rho v_\phi v_z - \frac{B_\phi B_z}{4\pi}\right)\right] = 0. \end{aligned} \tag{2.51}$$

This operation results in

$$\frac{\partial}{\partial t}(\Sigma R \langle v_\phi \rangle_\rho) + \frac{1}{R}\frac{\partial}{\partial R}\left[R^2\left(\Sigma \langle v_R \rangle_\rho \langle v_\phi \rangle_\rho + \left\langle \rho v_R \delta v_\phi - \frac{B_R B_\phi}{4\pi}\right\rangle\right)\right] = 0, \tag{2.52}$$

where $\langle \bullet \rangle_\rho \equiv \langle \rho \, \bullet \rangle / \Sigma$ and δv_ϕ denotes the fluctuating azimuthal velocity:

$$\delta v_\phi \equiv v_\phi - \langle v_\phi \rangle_\rho. \tag{2.53}$$

Note that in deriving Eq. (2.52) we have assumed that the boundary terms

$$R\left(\rho v_\phi v_z - \frac{B_\phi B_z}{4\pi}\right)\Bigg|_{z=-\infty}^{z=\infty} \tag{2.54}$$

vanish, which is equivalent to assuming that there is no disc wind. Defining

$$V_R \equiv \langle v_R \rangle_\rho, \quad V_\phi \equiv \langle v_\phi \rangle_\rho, \tag{2.55}$$

as well as

$$T_{R\phi} \equiv \left\langle \rho v_R \delta v_\phi - \frac{B_R B_\phi}{4\pi} \right\rangle, \tag{2.56}$$

we can write Eq. (2.52) in a form identical to Eq. (1.20)

$$\frac{\partial}{\partial t}(\varSigma R V_\phi) + \frac{1}{R}\frac{\partial}{\partial R}\left[R^2\left(\varSigma V_R V_\phi + T_{R\phi}\right)\right] = 0. \tag{2.57}$$

This shows that classical viscous disc theory can indeed be interpreted in terms of a mean field theory. The "anomalous" viscosity arises from *correlated* fluctuations in the velocity and the magnetic field. At this point, however, it becomes clear that matters are more complicated as in the heuristic picture outlined in Sec. 2.2.1: In principle, the stress tensor Eq. (2.56) may take on any value or even become negative. It is therefore not enough to have just *some* mechanism that generates turbulent fluid motions, rather it is of primary importance that these motions are correlated in such a way that they yield a stress tensor of the desired magnitude and sign.

Diffusion Equation for Surface Density

We proceed by using the azimuthally averaged height-integrated version of the continuity equation,

$$\frac{\partial \varSigma}{\partial t} + \frac{1}{R}\frac{\partial}{\partial R}(R\varSigma V_R) = 0, \tag{2.58}$$

to obtain an equation for V_R in analogy to Eq. (1.21):

$$V_R = \frac{\partial_R(R^2 T_{R\phi})}{R\varSigma\partial_R(RV_\phi)} = \frac{2\partial_R(R^2 T_{R\phi})}{R\varSigma\varOmega_{\mathrm{K}}}, \tag{2.59}$$

where we have made use of the assumption that $V_\phi \approx R\varOmega_{\mathrm{K}}$. Plugging this into Eq. (2.58), we obtain

$$\frac{\partial \varSigma}{\partial t} + \frac{1}{R}\frac{\partial}{\partial R}\left[\frac{2}{\varOmega}\frac{\partial}{\partial R}\left(R^2 T_{R\phi}\right)\right] = 0, \tag{2.60}$$

in analogy to Eq. (1.22).

Measuring the Alpha Parameter

The connection established by Eq. (2.56) opens the possibility to actually measure the value of the anomalous viscosity by means of a numerical simulation. Eq. (1.6) suggests the following relation between $T_{R\phi}$ and the non-dimensional parameter α defined in Eq. (2.47):

$$T_{R\phi} = \left\langle \frac{\mathrm{d}\ln\varOmega}{\mathrm{d}\ln R}\alpha\rho c_{\mathrm{s}}^2 \right\rangle = \frac{3}{2}\alpha P, \tag{2.61}$$

with $P \equiv \langle p \rangle$. This leads us to define the alpha parameter as

$$\alpha \equiv \frac{2}{3}\frac{T_{R\phi}}{P} \approx \frac{T_{R\phi}}{P}. \tag{2.62}$$

Throughout the paper, we will drop the numerical factor $3/2 \sim 1$, since it has by itself no physical significance but instead follows from how α is defined.

2.3 Disc Instabilities

There are quite a number of mechanisms that have been investigated as a possible explanation for enhanced angular momentum transport in accretion discs. As we will see, the most plausible mechanism is hydromagnetic turbulence initiated by the magnetorotational instability.

2.3.1 Hydrodynamical Shear Instabilities

It is natural to look first for purely hydrodynamical instabilities, since in general shear flows are known to easily develop instabilities. The dispersion relation for a hydrodynamical shear flow is simply

$$\omega^2 = c_{\mathrm{s}}^2 k^2 + \kappa^2, \tag{2.63}$$

where κ is the *epicyclic frequency* defined as

$$\kappa^2 \equiv \frac{2\Omega}{R}\frac{\mathrm{d}(\Omega R^2)}{\mathrm{d}R}. \tag{2.64}$$

In order for the rotation profile to become unstable, κ^2 should be negative (the Reynolds criterion). For Keplerian shear flows, where $\Omega \propto R^{-3/2}$ this criterion is not met, i.e. Keplerian flows are linearly stable to small perturbations.

Even when a flow configuration is stable against weak perturbations there is of course still the possibility that the flow might develop self-sustained turbulence if the perturbations are strong enough. Although the debate concerning nonlinear hydrodynamical instabilities is still ongoing, there has been so far no convincing demonstration that suitable instabilities exist, that have the desired properties needed for explaining enhanced angular momentum transport in accretion discs (Hawley et al., 1999; Balbus and Hawley, 2006).

2.3.2 Convective & Baroclinic Instability

The situation changes if a temperature gradient is present in the disc. The first possibility that has been investigated in this context is convective instability arising from a sufficiently steep vertical temperature gradient. Early simulations suggested that convective motions transport angular momentum in the wrong direction, namely inwards (see, for example Kley et al., 1993). This view has changed a bit since the recent simulations of (Lesur and Papaloizou, 2010). However, it is still questionable if the this mechanism is important for protoplanetary discs during their main evolutionary stage, since it is unlikely that they will be able to maintain a convectively unstable temperature profile Armitage (2010).

Instead of a vertical temperature gradient, one may also consider a radial gradient. Such a flow may be unstable to the baroclinic instability which is well known in the field of meteorology. It turns out that the linear instability that arises in this case is in fact only a transient phenomenon (Klahr, 2004). However, nonlinear perturbations lead to the sustained production of vortices and also to the transport of angular momentum. Whether the baroclinic instability is really a viable mechanism to explain angular momentum transport in protoplanetary discs is, however, not clear at the present. It has been found that in the case where both the baroclinic instability and the magnetorotational instability (which will be discussed in a moment) are present, then the magnetorotational instability will dominate the dynamics anyway Lyra & Klahr (2011).

2.3.3 Gravitational Instability

Another mechanism that may redistribute angular momentum in an accretion disc is gravitational instability. The problem with this mechanism is, of course, that the disc needs to be sufficiently massive, otherwise it will not work. For protoplanetary discs, gravitational instability should only play a role in the very early phase of the discs evolution, when the disc is very massive. Taking self gravity into account, the dispersion relation Eq. (2.63) is replaced by

$$\omega^2 = c_\mathrm{s}^2 k^2 - 2\pi G \Sigma |k| + \kappa^2. \tag{2.65}$$

From this dispersion relation, the condition for instability follows to be $Q < 0$, where Q is defined as

$$Q \equiv \frac{c_\mathrm{s}\kappa}{\pi G \Sigma}. \tag{2.66}$$

Q can be estimated to be

$$Q \approx \frac{c_\mathrm{s}\Omega}{\pi G \Sigma} = \frac{c_\mathrm{s}}{\Omega R}\frac{GM}{\pi G \Sigma R^2} \approx \frac{H}{R}\frac{M_\star}{M_\mathrm{disc}(R)}. \tag{2.67}$$

Since around young stellar objects, the disc masses may reach a mass of a fraction of $H/R \sim 0.1$ of the host star, gravitational instability might indeed be important in the outer parts of a very young protoplanetary disc.

2.3.4 Magnetorotational Instability

The magnetorotational instability (MRI) comes about by a combination of differential rotation and magnetic fields (Balbus and Hawley, 1998; Balbus, 2003, 2009). In the incompressible limit $c_\mathrm{s} \to \infty$, the effect of including magnetic fields is to change the purely hydrodynamic dispersion relation Eq. (2.63) to

$$\tilde{\omega}^4 - \tilde{\omega}^2\kappa^2 - 4\mathit{\Omega}^2(\boldsymbol{k}\cdot\boldsymbol{v}_\mathrm{A})^2 = 0, \tag{2.68}$$

where $\tilde{\omega}^2 \equiv \omega^2 - (\boldsymbol{k}\cdot\boldsymbol{v}_\mathrm{A})^2$ Balbus and Hawley (1991). A mode with wave vector $\boldsymbol{k}$ is unstable if it fulfills the criterion

$$(\boldsymbol{k}\cdot\boldsymbol{v}_\mathrm{A})^2 + \frac{\mathrm{d}\mathit{\Omega}^2}{\mathrm{d}\ln R} < 0. \tag{2.69}$$

As a consequence, the Reynolds criterion of outwardly decreasing angular momentum is replaced by the condition that the angular orbital frequency decrease outwards, i.e.

$$\frac{\mathrm{d}\mathit{\Omega}}{\mathrm{d}R} < 0, \tag{2.70}$$

which is satisfied in most astrophysical discs. Note that, for vanishing magnetic field, one does not recover the Reynolds criterion, meaning that magnetic fields alter the physical situation fundamentally. As long as ideal MHD can be applied, the flow will be unstable to arbitrarily small magnetic fields. Note also that, from Eq. (2.69), strong magnetic fields will have a stabilising effect. Therefore, the MRI is a weak field instability.

The basic mechanism of the MRI can be grasped by looking at a simple mechanical analogue. Let us look at an axisymmetric disc in the presence of a weak vertical magnetic field. The displacement of fluid elements in the orbital plane by an amount $\boldsymbol{\xi} \propto e^{ikz}$ yields a perturbed magnetic field which is given by

$$\delta\boldsymbol{B} = \boldsymbol{\nabla}\times(\boldsymbol{\xi}\times\boldsymbol{B}) = \mathrm{i}kB\,\boldsymbol{\xi}. \tag{2.71}$$

The magnetic tension force (per unit mass) corresponding to the newly created magnetic field is

$$\boldsymbol{f}_\mathrm{tension} = \frac{\boldsymbol{B}\cdot\boldsymbol{\nabla}\boldsymbol{B}}{4\pi\rho} = -k^2 v_\mathrm{A}^2\,\boldsymbol{\xi}. \tag{2.72}$$

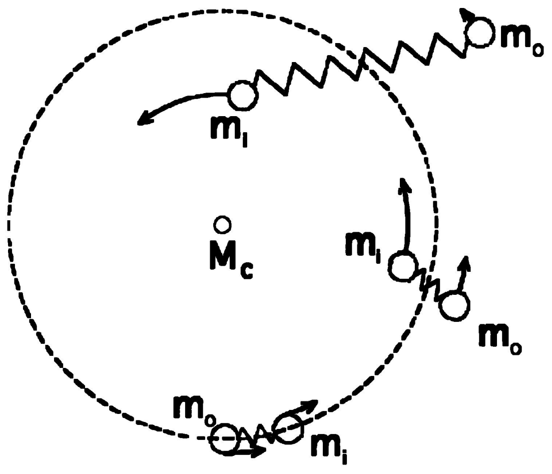

Fig. 2.3: Schematic picture elucidating the basic physical mechanism through which the magnetorotational instability operates. Fluid parcels moving at slightly different orbits are sheared apart in a runaway manner due magnetic tension forces. (Picture courtesy H. Ji)

The tension force is proportional to the displacement vector and has the opposite sign. This means it acts exactly like a classical mechanical spring. The situation is depicted schematically in Fig. 2.3, considering two fluid parcels initially on the same orbit. The parcels are disturbed in such a way that one parcel, m_i, moves on an orbit slightly nearer to the star, while the other parcel, m_o moves on an orbit slightly more far away from the star. The magnetic tension force exerts a negative torque on the inner parcel, causing it to move further inwards; and a positive torque on the outer parcel, causing it to move further outwards. This further increases the magnetic field and thus the magnetic tension between the two parcels, causing the process to run away. Note that the outward transport of angular momentum is an intrinsic property of the instability mechanism.

As we have seen, the MRI needs only two basic ingredients for it to work, namely an outwardly decreasing angular orbital frequency profile and a weak magnetic field. This means that the MRI operates under quite general conditions and is therefore supposed to be active in many astrophysical discs. However, there is as of today still no direct observational confirmation for this. Laboratory experiments of the MRI bear no direct relevance to the MRI in astrophysical systems since the parameter regime is very different. The only field where magnetorotational turbulence in astrophysical systems can be actively explored are thus numerical simulations. In the following, we will give a brief overview of the work that has been done in this field.

2.4 Numerical Simulations

Numerical simulations can be grouped into three classes according to the shape of the computational domain (see Fig.2.4). The simplest (and most often used) type of setup is the unstratified shearing-box model in which a small rectangular domain near the midplane of the disc is simulated, with the vertical component of gravity neglected [Fig.2.4 (a)]. Stratified shearing-box models include the vertical component of gravity and cover a large fraction of the vertical extent of the disc [Fig.2.4 (b)]. Finally, there are global simulations [Fig.2.4 (c)] which extend over a large radial range (tens of AU). Global simulations are usually performed using cylindrical or spherical coordinates. It is not possible to include the full disc (which has a size on the order of hundreds of AU) in a numerical simulation, since then it would not be possible to resolve the MRI resolved.

2.4.1 Unstratified Shearing Box Simulations

The first three-dimensional simulations of the magnetorotational instability were performed by Hawley et al. (1995). The basic setup consists of a rectangular box representing a small volume located at the midplane of an accretion disc that is co-moving with the background Keplerian shear flow (Fig. 2.4). The vertical component of gravity is neglected; as a consequence the physical situation looks uniform in the whole box. The boundary conditions in the azimuthal and vertical directions are periodic. In the radial direction, so-called shear-periodic boundary conditions are used that are consistent with the background shear flow (see Chap. 4). A constant vertical magnetic field is imposed at the beginning, leading to rapid growth of the MRI and sustained magnetorotational turbulence. In a later work, the authors find sustained turbulence also in the case where the initial magnetic field is designed in such a way that it has zero net vertical flux (Hawley et al., 1996). The most important result of these early works is that the magnetorotational turbulence leads to outward angular momentum transport at a rate that is roughly compatible with observations (King et al., 2007), establishing the MRI as the most likely cause for enhanced angular momentum transport in astrophysical accretion discs.

These early simulations lacked the resolution to allow for a detailed study of the properties of magnetorotational turbulence. Also, a thorough resolution study was not possible with the computational resources available at that time. The first such study (Fromang and Papaloizou, 2007) found that for the case of magnetorotational turbulence in the absence of a net vertical magnetic flux, the turbulent transport scaled inversely proportional to the numerical resolution, suggesting zero transport at very high resolution. The

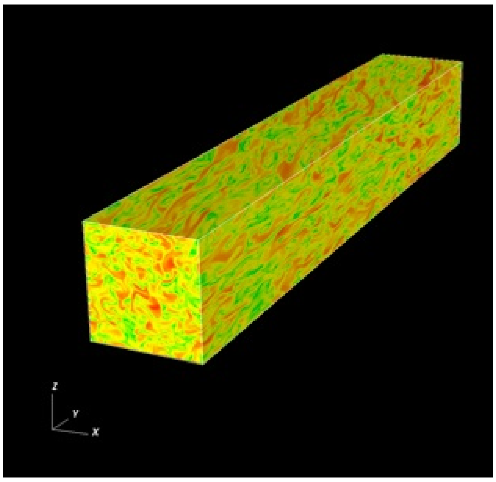

(a) *Unstratified shearing box:* A box of small radial and vertical extent located at the midplane of the accretion disc.

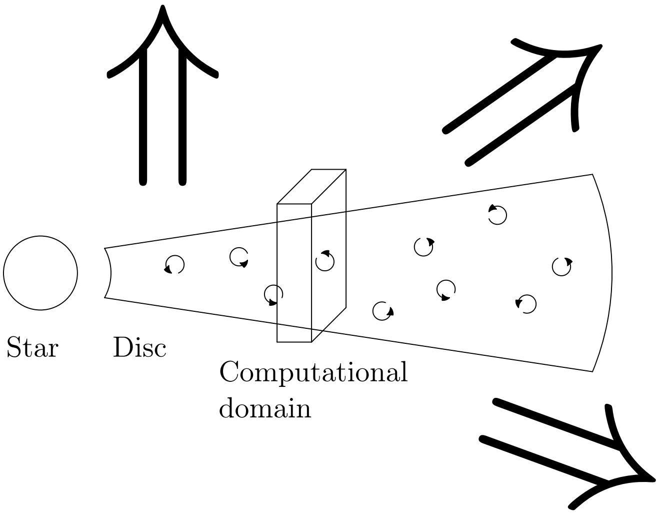

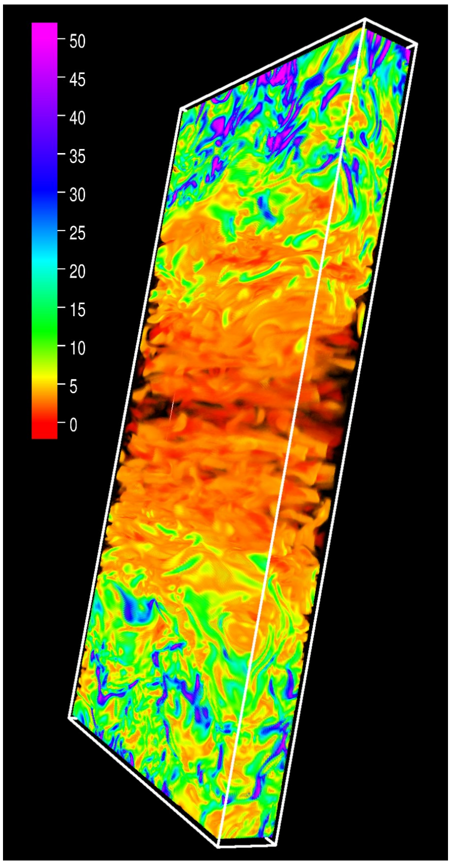

(b) *Stratified shearing box:* A box of small radial extent that covers the full vertical height of the disc.

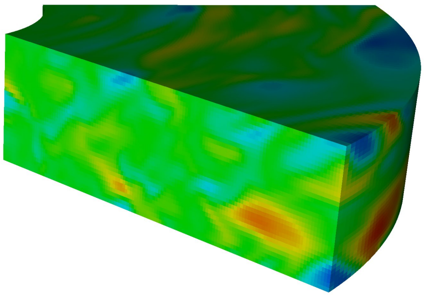

(c) *Global simulation:* Usually a "cake piece" that covers a large radial extent.

Fig. 2.4: The different setups used in numerical simulations of the magnetorotational instability in accretion discs. The unstratified shearing box, which is periodic and homogeneous, is the most widely used model but also the least realistic one. Stratified shearing box models offer a good compromise between computational complexity and physical realism. Global calculations are rare, since they are difficult to set up and very expensive computationally.

authors conclude that numerical effects occurring at the grid scale have a non-negligible influence on the simulation outcome. In order to quantify these effects, the authors estimate the numerical Prandtl number[4] of their code and find it to be of order unity or bigger. Later works found the same decrease of the turbulent saturation with increasing resolution using other codes (Guan et al., 2009; Simon et al., 2009). In a follow-up paper (Fromang et al., 2007), simulations with explicit physical dissipation were performed. This study found that the magnetic Prandtl number plays a decisive role in determining the fate of the magnetorotational turbulence: If it is too small the turbulence will die off.[5]

In a later work, the dependence of the turbulent saturation level on the numerical scheme was explored (Balsara and Meyer, 2010). The authors find that the results depend substantially on the numerical method employed. Depending on what type of Riemann solver one uses, the turbulence might not even be sustained, but instead the simulation converges to a laminar state in the zero net-flux case (see also Chap. 4). The highest resolution simulation performed as of today was reported in Fromang (2010). In this simulation, the inertial range of the turbulence could be resolved for the first time. The author finds that when using physical dissipation with a fixed magnetic Prandtl number, the turbulent transport does depend only very weakly on the Reynolds number, indicating that the decline of the turbulent activity with increasing resolution in a purely ideal simulation is indeed a numerical artifact.

The most recent work on the Prandtl number dependence of magnetorotational turbulence suggests that the turbulence found in unstratified shearing boxes is actually a transient phenomenon: Rempel et al. (2010) performed a parameter study of visco-resistive shearing box calculations using a pseudo-spectral MHD code. They find that the turbulence always dies at some time and the system converges towards a laminar state, no matter how big the value of the magnetic Prandtl number. At the present time it is not clear, however, if this behaviour can be reproduced with other codes.

Aside from all these considerations, the unstratified shearing box with zero net flux is an idealisation that will hardly be found in nature: In a real accretion disc, it is unlikely that the flux permeating a small volume picked out of the disc will be exactly zero; moreover, as we will see in the next section, when adding the vertical stratification, the problem of the resolution dependence of the turbulent activity vanishes.

---

[4] The Prandtl number is defined as the ratio of viscosity to resistivity.

[5] These results can be understood as follows: In the case of the unstratified shearing box with zero net flux, the fate of the magnetic field depends on the working of a small-scale dynamo. The magnetic field is wound up in the turbulent eddies at small scales and thereby amplified. If the ratio of resistivity to viscosity becomes too big, this process is destroyed by reconnection, and the magnetic field will decay [see also (Schekochihin et al., 2002a,b).]

2.4.2 Stratified Simulations

The first simulations including the vertical component of gravity were performed by Stone et al. (1996). As in the unstratified simulations, magnetorotational turbulence leads to sustained transport of angular momentum. However, in a stratified setup, the turbulent activity shows strong variations on scales of ~ 20 orbits, the reason for this being still a matter of debate (see Chap. 5).

Including the vertical stratification is a necessary prerequisite for including radiation transport in order to allow the disc to cool by emitting radiation through the vertical boundaries. The first stratified radiative accretion disc simulation was performed by Turner (2004), modelling a patch of a radiation-dominated accretion disc around a black hole. The maximum density contrast that was achieved in this simulation (as determined by the density floor) was 2% of the midplane density, which was not even enough to have the photosphere included in the computational domain.

The first gas-pressure dominated radiative accretion disc simulation was performed by Hirose et al. (2006). The simulation parameters where chosen according to a Galactic black hole binary, with a maximum density contrast of 10^{-5}. The photosphere, whose position was found to vary significantly during the course of the simulation, was always located very near the upper boundary or even outside the computational domain.

The first radiative simulations with parameters appropriate for a protoplanetary disc was described in Flaig et al. (2010). The simulations covered a larger domain in the vertical direction than any previous radiative simulations and achieved a density contrast of 10^{-6}. The photosphere was located well inside the computational domain for the whole time. One of the most interesting results of this study was that the turbulent Mach number at the location of the photosphere did actually match with previous observations of turbulent line broadening in protoplanetary discs.

2.4.3 Global Simulations

Global simulations of magnetorotational turbulence started with the works of Matsumoto and Shibata (1997), Armitage (1998), Hawley (2000), Hawley (2001) and Hawley and Krolik (2001). With the exception of Armitage (1998), these early works all simulated a thick accretion torus around a black hole. The advantage of this setup is that the whole disc can be made to fit into the computational domain, therefore avoiding the need for sophisticated boundary conditions in the radial direction. Essentially the global models gave results that were compatible with the results from the earlier local models. The model of Armitage (1998), however, yielded stresses one order of magnitude larger than corresponding local simulations.

A global stratified setup for a protoplanetary disc model was described in Fromang and Nelson (2006). The authors employed buffer zones at the radial boundaries where the turbulence was damped via viscosity and resistivity. In a latter paper (Fromang and Nelson, 2009) the authors investigated the settling of small dust particles under the influence of the turbulence. The first non-ideal global protoplanetary disc simulations were reported in Dzyurkevich et al. (2010), who used a prescribed resistivity profile that was held fixed during the whole course of the simulation. Global simulations including radiation transport and/or disc chemistry have not been reported so far.

2.5 Summary

In the present chapter, we were concerned with describing the physics of protoplanetary discs from a microscopic viewpoint. We summarise the most important points:

- The dynamics of the gas in protoplanetary discs is governed by the equations of radiation-magnetohydrodynamics. Since protoplanetary discs are for some part only poorly ionised, one has in general to include non-ideal MHD effects, namely Ohmic resistivity, the Hall effect and ambipolar diffusion. In the planet-forming region inside the first ten AU, resistivity will be the most important effect.

- Molecular viscosity is many orders of magnitude too small to account for the observed accretion rates. This leads to the heuristic idea of a *turbulent* viscosity, where turbulent eddies take the place of the molecules. Since the mean free path of the eddies will be much larger than the mean free path of the molecules, the corresponding eddy viscosity is be much larger.

- However, the effective viscosity generated by turbulence will in general be different from a classical shear viscosity. The effective stress tensor is determined by correlated fluctuations in the velocity and magnetic field components. This means that it is not sufficient to have just *some* sort of turbulence in order to achieve outward angular momentum transport; rather the turbulence must also have the right properties.

- Turbulence initiated by the magnetorotational instability is the most promising candidate to explain turbulent angular momentum transport in accretion discs. It operates under a broad range of conditions and leads to outward angular momentum transport at a rate that is compatible with observations.

Although magnetorotational turbulence is usually considered to be the most important physical factor determining the dynamics of protoplanetary discs, truly self-consistent models of MRI-turbulent protoplanetary discs have not been reported until recently. In the present thesis, we describe the first such models that include all the relevant physical factors. We will start our presentation with an analytical analysis of the linear growth phase of the MRI including radiation transport and resistivity (Chap. 3). After this, we move on to numerical simulations, where we investigate the influence of radiation transport on the turbulent saturation level of magnetorotational turbulence (Chap. 4). Finally, we will describe the first self-consistent numerical simulations of turbulent protoplanetary discs and discuss the connection to astrophysical observations (Chap. 5+6).

Chapter 3: Linear Growth Phase of the MRI

3.1 Local Stability Analysis

Before performing fully nonlinear numerical simulations of MRI-induced MHD turbulence, we will first study the linear growth phase of the instability, which can be investigated by analytical means. The aim of this study will mainly be to determine to what extend the two most important non-ideal physical processes acting in protoplanetary discs, namely resistivity and radiative diffusion, change the behaviour of the instability. The analytical results will not only help to better understand how the MRI will work in a protoplanetary disc, but they will also provide a useful analytical solution against which our numerical code (and especially the radiative diffusion and resistivity parts) can be tested.

Since the MRI is a local instability, it can be studied by means of a local analysis. This means we are seeking for solutions of the fluid-dynamical equations of the form

$$q = q_0 + \delta q, \tag{3.1}$$

where q is the vector of fluid variables. We take the δq to be plane-wave axisymmetric perturbations, i.e.

$$\delta q \propto \exp[\mathrm{i}(k_r r + k_z z) + \sigma t]. \tag{3.2}$$

We restrict ourselves to axisymmetric modes (i.e. $k_\phi = 0$) because the axisymmetric modes are the dominant ones (see Sec. 3.2) and the inclusion of non-axisymmetric modes would only complicate the analysis unnecessarily.

We consider a volume of the accretion disc that is small enough so that all the background variables q_0 except the velocity can be taken constant. We switch to a cylindrical coordinate system (R, ϕ, z) that is rotating with the local Keplerian angular frequency $\Omega_0 = \Omega(R_0)$ at a certain radius R_0 in the disc. In this system, the background Keplerian shear flow becomes locally

$$\boldsymbol{v}_0 \approx -\frac{3}{2}\Omega_0 r\,\hat{\boldsymbol{\phi}}. \tag{3.3}$$

We consider a situation where the initial radial magnetic field is zero, i.e. we take the magnetic field to be of the form

$$\boldsymbol{B}_0 = B_{0\phi}\,\hat{\boldsymbol{\phi}} + B_{0z}\,\hat{\boldsymbol{z}}. \tag{3.4}$$

The reason for this is that a configuration that has a radial field is not in equilibrium, because an initially radial field would rapidly be transformed into an azimuthal field due to the background shear flow.

3.2 Ideal MHD Dispersion Relation

We start our analysis by deriving the MRI dispersion relation in the limit of ideal MHD, i.e. neglecting non-ideal MHD effects and radiative diffusion. The equations that we want to solve are thus

$$\frac{\partial\rho}{\partial t} + \nabla\cdot(\rho\boldsymbol{v}) = 0, \tag{3.5a}$$

$$\frac{\partial\boldsymbol{v}}{\partial t} + \boldsymbol{v}\cdot\nabla\boldsymbol{v} + \frac{1}{\rho}\nabla\left(p + \frac{B^2}{4\pi}\right) - \frac{\boldsymbol{B}\cdot\nabla\boldsymbol{B}}{4\pi\rho} + \nabla\varPhi = 0, \tag{3.5b}$$

$$\frac{\partial\boldsymbol{B}}{\partial t} = \nabla\times(\boldsymbol{v}\times\boldsymbol{B}), \tag{3.5c}$$

$$\frac{\partial p}{\partial t} + \boldsymbol{v}\cdot\nabla p = -\gamma p\,\nabla\cdot\boldsymbol{v}. \tag{3.5d}$$

Inserting the ansatz (3.1, 3.2) into the above equations, we obtain the following linearised equations (dropping, from now on, the index ‘0’ on the background fluid variables and the orbital angular frequency):

$$\sigma\,\delta\rho = -\rho\,\mathrm{i}\boldsymbol{k}\cdot\delta\boldsymbol{v}, \tag{3.6a}$$

$$\sigma\,\delta\boldsymbol{v} - \frac{3}{2}\varOmega\,\delta v_r\,\hat{\boldsymbol{\phi}} + \frac{\mathrm{i}\boldsymbol{k}}{\rho}\cdot\left(\delta p + \frac{\delta\boldsymbol{B}\cdot\boldsymbol{B}}{4\pi}\right) - \frac{\mathrm{i}k_zB_z}{4\pi\rho}\,\delta\boldsymbol{B} + 2\varOmega\,\hat{\boldsymbol{z}}\times\delta\boldsymbol{v} = 0, \tag{3.6b}$$

$$\sigma\,\delta\boldsymbol{B} = -\mathrm{i}\boldsymbol{k}\cdot\delta\boldsymbol{v}\,\boldsymbol{B} + \mathrm{i}k_zB_z\left(\delta\boldsymbol{v} - \frac{3\varOmega}{2\sigma}\,\delta v_r\,\hat{\boldsymbol{\phi}}\right), \tag{3.6c}$$

$$\sigma\,\delta p = -\gamma p\,\mathrm{i}\boldsymbol{k}\cdot\delta\boldsymbol{v}. \tag{3.6d}$$

3.2.1 Incompressible Fluid

Making the simplifying assumption of incompressibility, $\boldsymbol{k}\cdot\delta\boldsymbol{v}=0$, we get $\delta\rho=\delta p=0$, leaving the following system of equations:

$$\sigma\,\delta\boldsymbol{v}-\frac{3}{2}\varOmega\,\delta v_r\,\hat{\boldsymbol{\phi}}+\frac{\mathrm{i}\boldsymbol{k}}{\rho}\frac{\delta\boldsymbol{B}\cdot\boldsymbol{B}}{4\pi}-\frac{\mathrm{i}k_zB_z}{4\pi\rho}\,\delta\boldsymbol{B}+2\varOmega\,\hat{\boldsymbol{z}}\times\delta\boldsymbol{v}=0, \tag{3.7a}$$

$$\sigma\,\delta\boldsymbol{B}=\mathrm{i}k_zB_z\left(\delta\boldsymbol{v}-\frac{3\varOmega}{2\sigma}\,\delta v_r\,\hat{\boldsymbol{\phi}}\right). \tag{3.7b}$$

Next, we insert Eq. (3.7b) into Eq. (3.7a) in order to eliminate $\delta\boldsymbol{B}$, yielding

$$\begin{aligned}\sigma^2\,\delta\boldsymbol{v}-\frac{3}{2}\sigma\varOmega\,\delta v_r\,\hat{\boldsymbol{\phi}}-\boldsymbol{k}k_zv_{\mathrm{A}z}\left(\delta\boldsymbol{v}\cdot\boldsymbol{v}_\mathrm{A}-\frac{3\varOmega}{2\sigma}\,\delta v_r v_{\mathrm{A}\phi}\right)&\\+k_z^2v_{\mathrm{A}z}^2\left(\delta\boldsymbol{v}-\frac{3\varOmega}{2\sigma}\,\delta v_r\,\hat{\boldsymbol{\phi}}\right)+2\sigma\varOmega\,\hat{\boldsymbol{z}}\times\delta\boldsymbol{v}=0;&\end{aligned} \tag{3.8}$$

where we have defined the Alfvén speed according to

$$\boldsymbol{v}_\mathrm{A}\equiv\frac{\boldsymbol{B}}{\sqrt{4\pi\rho}}. \tag{3.9}$$

Adding the x-component and $-k_r/k_z$ times the z-component of this equation and making use of the relation $\delta v_z=-(k_r/k_z)\,\delta v_r$ gives

$$(\sigma^2+k_z^2v_{\mathrm{A}z}^2)\frac{k^2}{k_z^2}\,\delta v_r-2\sigma\varOmega\,\delta v_\phi=0. \tag{3.10}$$

Together with the y-component of Eq. (3.8),

$$(\sigma^2+k_z^2v_{\mathrm{A}z}^2)\,\delta v_\phi+\frac{\varOmega\sigma}{2}\left(1-3\frac{k_z^2v_{\mathrm{A}z}^2}{\sigma^2}\right)\delta v_r=0. \tag{3.11}$$

We now have two equations that contain only two unknowns, namely δv_r and δv_ϕ. Note that the toroidal magnetic field component, B_ϕ has dropped out of the equations. The dispersion relation now follows as

$$\tilde{\sigma}^4+\varOmega^2\tilde{\sigma}^2-4\varOmega^2\frac{k_z^4v_{\mathrm{A}z}^2}{k^2}=0, \tag{3.12}$$

where we have defined $\tilde{\sigma}^2\equiv\sigma^2+k_z^2v_{\mathrm{A}z}^2$. The dispersion relation Eq. (3.12) is equivalent to the dispersion relation derived in the seminal paper of Hawley et al. (1995) (their

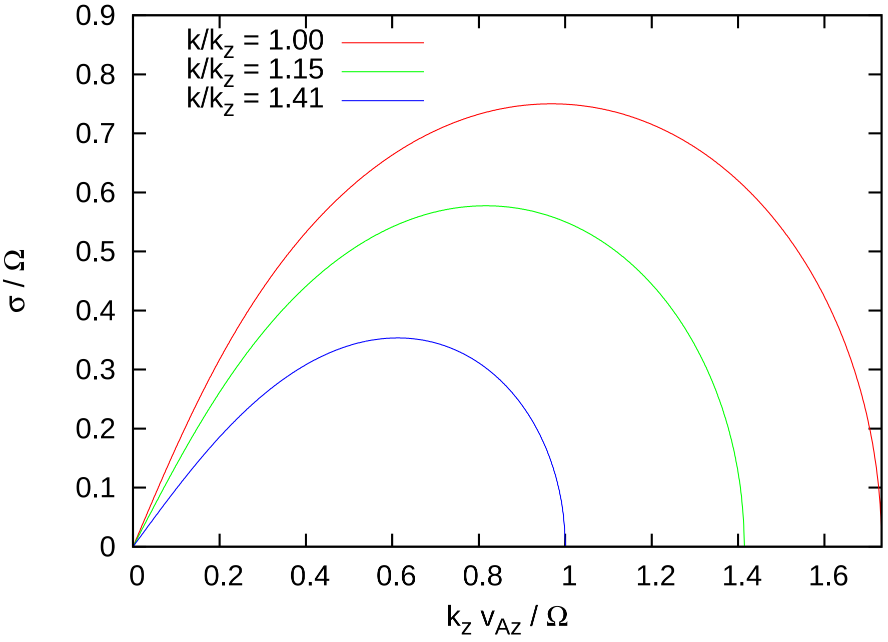

Fig. 3.1: Plots of the MRI growth rates σ/Ω as a function of the non-dimensional wave number $k_z v_{\mathrm{A}z}/\Omega$, obtained under the assumption of incompressibility. The growth rates are largest for vertical modes, which have $k_r = 0$.

Eq. 2.5) except that they included gradients in the background density and pressure, which we do not. The quartic equation Eq. (3.12) contains only even powers of $\tilde{\sigma}$ so the solution can immediately be written down:

$$\frac{\sigma^2}{\Omega^2} = -\frac{k_z^2 v_{\mathrm{A}z}^2}{\Omega^2} - \frac{1}{2} \pm \sqrt{\frac{1}{4} + 4\frac{k_z^4 v_{\mathrm{A}z}^2}{k^2 \Omega^2}}. \tag{3.13}$$

In Fig. 3.1 we plot the resulting MRI growth rates as a function of wavenumber for different values of the ratio k/k_z. As the ratio k/k_z increases, the growth rates decrease. The fastest growth rates are thus obtained for the case $k = k_z$, and from Eq. (3.13) it can be deduced that the fastest growth occurs at wavenumber

$$k_{z,\mathrm{max}} = \sqrt{\frac{15}{16}}\frac{\Omega}{v_{\mathrm{A}z}}, \tag{3.14}$$

and the corresponding maximum growth rate is

$$\sigma_{\max} = \frac{3}{4}\Omega. \tag{3.15}$$

The critical wavenumber k_{crit} beyond which the instability ceases to exist is found to be

$$k_{\text{crit}} = \sqrt{3}\frac{\Omega}{v_{\text{A}z}}. \tag{3.16}$$

To summarise, the most important properties of the magnetorotational instability are that it operates at wavelengths $k_z \sim \Omega/v_{\text{A}z}$ and that it grows fast, on an orbital timescale.

3.2.2 Including Compressibility

We now calculate the MRI dispersion relation retaining the terms containing $\boldsymbol{k}\cdot\delta\boldsymbol{v}$ in equations Eqs. (3.6), i.e. we include the effects of a finite compressibility. Eq. (3.8) now becomes

$$\sigma^2\,\delta\boldsymbol{v} - \frac{3}{2}\sigma\Omega\,\delta v_r\,\hat{\boldsymbol{\phi}} - \boldsymbol{k}k_z v_{\text{A}z}\left(\boldsymbol{v}_{\text{A}}\cdot\delta\boldsymbol{v} - \frac{3\Omega}{2\sigma}\,v_{\text{A}\phi}\,\delta v_r\right) + \boldsymbol{k}(c_{\text{s}}^2 + v_{\text{A}}^2)\,\boldsymbol{k}\cdot\delta\boldsymbol{v}$$
$$- k_z v_{\text{A}z}\boldsymbol{v}_{\text{A}}\,\boldsymbol{k}\cdot\delta\boldsymbol{v} + k_z^2 v_{\text{A}z}^2\left(\delta\boldsymbol{v} - \frac{3\Omega}{2\sigma}\,\delta v_r\,\hat{\boldsymbol{\phi}}\right) + 2\sigma\Omega\,\hat{\boldsymbol{z}}\times\delta\boldsymbol{v} = 0, \tag{3.17}$$

where we have defined the gas sound speed as $c_{\text{s}}^2 \equiv \gamma p/\rho$. We now introduce a new quantity K via the definition

$$K\,\delta v_r \equiv \boldsymbol{k}\cdot\delta\boldsymbol{v}. \tag{3.18}$$

Physically, the quantity K can be interpreted to measure the amount of compressibility of the perturbations.

Now, using the same strategy as above for the incompressible case, we find that Eqs. (3.10) and (3.11) become

$$\left(\sigma^2 + k_z^2 v_{\text{A}z}^2 - \frac{Kk_r}{k^2}\sigma^2\right)\frac{k^2}{k_z^2}\,\delta v_r - 2\sigma\Omega\,\delta v_\phi = 0, \tag{3.19a}$$

$$(\sigma^2 + k_z^2 v_{\text{A}z}^2)\,\delta v_\phi + \left[\frac{\Omega\sigma}{2}\left(1 - 3\frac{k_z^2 v_{\text{A}z}^2}{\sigma^2}\right) - k_z v_{\text{A}z} v_{\text{A}\phi} K\right]\delta v_r = 0. \tag{3.19b}$$

In each of the two equations one additional term containing the quantity K has appeared, leading to two additional terms (as compared to Eq. (3.12)) in the general dispersion relation as it follows from Eqs. (3.19):

$$\left(\tilde{\sigma}^2 - \frac{k_r K}{k^2}\sigma^2\right)\frac{k^2}{k_z^2}\,\tilde{\sigma}^2 + \Omega^2\tilde{\sigma}^2 - 4\Omega^2 k_z^2 v_{\text{A}z}^2 - 2\Omega\sigma v_{\text{A}\phi} v_{\text{A}z} k_z K = 0. \tag{3.20}$$

As said, however, we still have to calculate K. This is done by looking at the z-component of Eq. (3.17):

$$\sigma^2\,\delta v_z - k_z^2 v_{\mathrm{A}\phi} v_{\mathrm{A}z}\,\delta v_\phi + k_z^2 v_{\mathrm{A}z}\frac{3\Omega}{2\sigma} v_{\mathrm{A}\phi}\,\delta v_r + K k_z (c_\mathrm{s}^2 + v_{\mathrm{A}y}^2)\,\delta v_r = 0. \tag{3.21}$$

Note that in order to obtain the above equation we have made use of Eq. (3.18). Combining Eq. (3.19a) with Eq. (3.20), we obtain the following expression relating δv_ϕ and δv_r:

$$\delta v_\phi = \left(-\frac{\Omega}{2\sigma} + 2\frac{\Omega}{\sigma}\frac{k_z^2 v_{\mathrm{A}z}^2}{\tilde{\sigma}^2} + \frac{K k_z v_{\mathrm{A}\phi} v_{\mathrm{A}z}}{\tilde{\sigma}^2} \right) \delta v_r. \tag{3.22}$$

This relation can now be used to eliminate δv_ϕ from Eq. (3.21) yielding the following expression for K,

$$K = \frac{\tilde{\sigma}^2 \sigma^2 k_r - 2\sigma\Omega k_z^3 v_{\mathrm{A}\phi} v_{\mathrm{A}z}}{\tilde{\sigma}^2(\sigma^2 + k_z^2 c_\mathrm{s}^2) + \sigma^2 k_z^2 v_{\mathrm{A}\phi}^2}, \tag{3.23}$$

which completes our derivation of the compressible MRI dispersion relation.

Comparison to the Blaes and Balbus (1994) dispersion relation

The first paper in which the effects of a finite compressibility were included is the paper by Blaes and Balbus (1994). However, they restricted their analysis to vertical modes. Defining

$$\omega \equiv \mathrm{i}\sigma, \tag{3.24a}$$

$$\tilde{\omega}^2 = -\tilde{\sigma}^2, \tag{3.24b}$$

$$D_\mathrm{ms} \equiv \omega^2 - k_z^2 (c_\mathrm{s} + v_{\mathrm{A}\phi}^2), \tag{3.24c}$$

$$D_\mathrm{BH} \equiv \frac{k^2}{k_z^2}\tilde{\omega}^4 - \Omega^2\tilde{\omega}^2 - 4\Omega^2 k_z^2 v_{\mathrm{A}z}^2, \tag{3.24d}$$

we can write Eq. (3.20) in an alternative way as

$$D_\mathrm{ms} D_\mathrm{BH} - k_z^2 v_{\mathrm{A}\phi}^2 v_{\mathrm{A}z}^2 (k^2 \tilde{\omega}^2 + 3k_z^2 \Omega^2) - \frac{k_r^2}{k_z^2}\tilde{\omega}^2\omega^4 = 0. \tag{3.25}$$

Written in this form, and if we set $k_r = 0$, our dispersion relation becomes equivalent to the dispersion relation given in their paper, as can be verified by comparing Eq. (3.25) to their Eq. (64).

Applicability of Incompressibility Approximation

Next, we may ask under what conditions the assumption of negligible compressibility is a good approximation; for simplicity we consider now only vertical modes, i.e. we set $k_r = 0$. Compressibility is negligible if the last term in Eq. (3.20) is small compared to the second last term, which is equivalent to

$$\sigma^2 k_z^2 v_{\mathrm{A}\phi}^2 \ll \tilde{\sigma}^2(\sigma^2 + k_z^2 c_\mathrm{s}^2) \tag{3.26}$$

It therefore turns out that a sufficient condition for the approximation of incompressibility to hold is that the azimuthal magnetic field is sufficiently subthermal, i.e. $v_{\mathrm{A}\phi} \ll c_\mathrm{s}$.

Effect of Compressibility on the Growth Rates

Since in the dispersion relation Eq. (3.20) the terms containing K vanish when $\sigma \to 0$, the critical wavelength is not changed due to compressibility and is still given by Eq. (3.16). This means that compressibility does not change the range in which the instability operates, it only modifies the growth rates. To calculate the effects which a finite compressibility has on the growth rates, we differentiate Eq. (3.20) with respect to $|K|$ to obtain

$$\frac{\mathrm{d}\sigma}{\mathrm{d}|K|} = \mathrm{sgn}(K)\frac{2\sigma \Omega v_{\mathrm{A}\phi} v_{\mathrm{A}z} k_z}{4(k^2/k_z^2)\tilde{\sigma}^3 + 2\tilde{\sigma}\Omega^2 - 2\Omega v_{\mathrm{A}\phi} v_{\mathrm{A}z} k_z K}. \tag{3.27}$$

From Eq. (3.23) we see that for vertical modes $K < 0$, from which it follows that $\mathrm{d}\sigma/\mathrm{d}|K| < 0$. This means that for vertical modes, compressibility reduces the growth rates if there is an azimuthal field present. This behaviour is depicted in Fig. 3.2, where the growth rates are plotted for different values of the ratio B_ϕ/B_z. For non-vertical modes, K might actually become positive, implying the possibility of $\mathrm{d}\sigma/\mathrm{d}|K| > 0$, i.e. an increase of the growth rates.

3.3 General Dispersion Relation

3.3.1 Linearised Equations

We now proceed to calculate a more general dispersion relation, suitable for accretion discs in which the ambipolar diffusion and Hall term can be neglected. The corresponding dispersion relation can be applied to the inner, more denser regions of protoplanetary discs inside the first few ten AU. The set of equations that we want to solve is thus given by Eqs. (2.27a), (2.27b), (2.27c), (2.32) and (2.33), with the ambipolar diffusion and

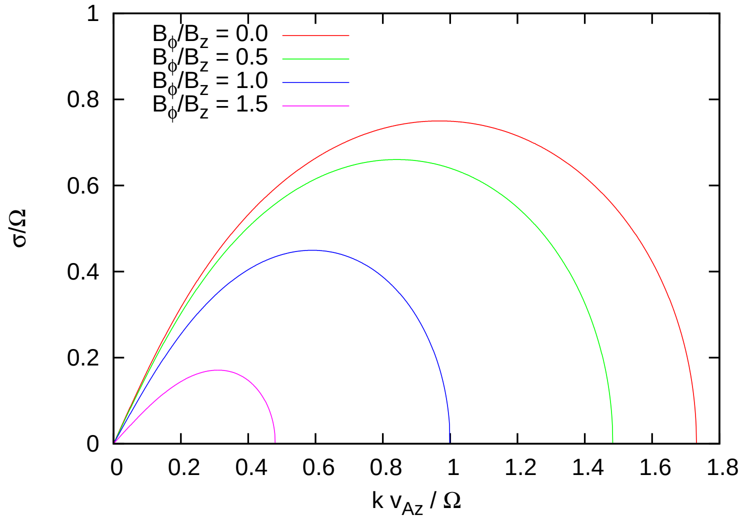

Fig. 3.2: MRI growth rates of vertical modes ($k_r = 0$) for the case $c_\mathrm{s} = 0$, i.e. highly superthermal magnetic fields. Plotted are the growth rates σ/Ω as a function of the non-dimensional wave number $k_z v_{\mathrm{A}z}/\Omega$, for different values of B_ϕ/B_z.

Hall terms dropped. In order to keep our calculation as general as possible, we relax the restriction that the disc be gas-pressure dominated, which means that we have to replace $\boldsymbol{\nabla} p$ by $\boldsymbol{\nabla} p + \lambda \nabla E$. We list the complete set of equations here for reference:

$$\frac{\partial \rho}{\partial t} + \boldsymbol{\nabla} \cdot (\rho \boldsymbol{v}) = 0, \tag{3.28a}$$

$$\rho \frac{\partial \boldsymbol{v}}{\partial t} + \rho \boldsymbol{v} \cdot \boldsymbol{\nabla} \boldsymbol{v} = -\boldsymbol{\nabla} p - \lambda \boldsymbol{\nabla} E + \frac{(\boldsymbol{\nabla} \times \boldsymbol{B}) \times \boldsymbol{B}}{4\pi} + \rho \boldsymbol{\nabla} \varPhi, \tag{3.28b}$$

$$\frac{\partial \boldsymbol{B}}{\partial t} = \boldsymbol{\nabla} \times (\boldsymbol{v} \times \boldsymbol{B} - \eta \boldsymbol{\nabla} \times \boldsymbol{B}), \tag{3.28c}$$

$$\frac{\partial e}{\partial t} + \boldsymbol{\nabla} \cdot (e \boldsymbol{v}) = -p \boldsymbol{\nabla} \cdot \boldsymbol{v} + \frac{\eta}{4\pi} |\boldsymbol{\nabla} \times \boldsymbol{B}|^2 - \kappa_\mathrm{P} \rho (4\pi B - cE), \tag{3.28d}$$

$$\frac{\partial E}{\partial t} + \boldsymbol{\nabla}(E \boldsymbol{v}) = -\frac{E}{3} \boldsymbol{\nabla} \cdot \boldsymbol{v} + \kappa_\mathrm{P} \rho (4\pi B - cE) - \boldsymbol{\nabla} \cdot \boldsymbol{F}, \tag{3.28e}$$

$$\boldsymbol{F} = -\frac{\lambda c}{\kappa_\mathrm{F} \rho} \boldsymbol{\nabla} E. \tag{3.28f}$$

Assuming that the background resistivity η, the thermal energy e, the radiation energy E are constant, and that radiation and matter are in thermodynamical equilibrium, such that $E = aT^4$, the corresponding linearised equations become:

$$\sigma\,\delta\rho = -\rho\,\mathrm{i}\boldsymbol{k}\cdot\delta\boldsymbol{v}, \tag{3.29}$$

$$\sigma\,\delta\boldsymbol{v} - \frac{3}{2}\Omega\,\delta v_r\,\hat{\boldsymbol{\phi}} + \frac{\mathrm{i}\boldsymbol{k}}{\rho}\cdot\left(\delta p + \lambda\delta E + \frac{\delta\boldsymbol{B}\cdot\boldsymbol{B}}{4\pi}\right) - \frac{\mathrm{i}k_z B_z}{4\pi\rho}\,\delta\boldsymbol{B} + 2\Omega\,\hat{\boldsymbol{z}}\times\delta\boldsymbol{v} = 0, \tag{3.30}$$

$$\sigma_\eta\,\delta\boldsymbol{B} = -\mathrm{i}\boldsymbol{k}\cdot\delta\boldsymbol{v}\,\boldsymbol{B} + \mathrm{i}k_z B_z\left(\delta\boldsymbol{v} - \frac{3\Omega}{2\sigma_\eta}\,\delta v_r\,\hat{\boldsymbol{\phi}}\right), \tag{3.31}$$

$$\delta p = \gamma\frac{p}{\rho}\delta\rho - (\gamma-1)\alpha_{\mathrm{P}}E\left(4\frac{\delta T}{T} - \frac{\delta E}{E}\right), \tag{3.32}$$

$$\delta E = \frac{4E}{3\rho}\delta\rho + \alpha_{\mathrm{P}}E\left(4\frac{\delta T}{T} - \frac{\delta E}{E}\right) - \alpha_{\mathrm{F}}\,\delta E; \tag{3.33}$$

where we have defined

$$\sigma_\eta \equiv \sigma + \eta k^2, \tag{3.34}$$

$$\alpha_{\mathrm{P}} \equiv \frac{\kappa_{\mathrm{P}}\rho c}{\sigma}, \tag{3.35}$$

$$\alpha_{\mathrm{F}} \equiv \frac{k^2}{\sigma}\frac{\lambda c}{\kappa_{\mathrm{F}}\rho}. \tag{3.36}$$

The dimensionless quantity α_{P} describes the rate at which radiation and matter are thermally coupled with respect to the growth rate of the instability while α_{F} constitutes a non-dimensional diffusion coefficient. Note that Eq. (3.6c) ensures that the divergence-free constraint $\boldsymbol{k}\cdot\delta\boldsymbol{B} = 0$ be satisfied, as it should be.

3.3.2 Dispersion Relation

Introducing the *effective sound speed* C_{eff} via the definition

$$C_{\mathrm{eff}}^2 \equiv \frac{\delta p}{\delta\rho} + \lambda\frac{\delta E}{\delta\rho}, \tag{3.37}$$

the linearised momentum equation can be written in a form similar to Eq. (3.6b):

$$\sigma\,\delta\boldsymbol{v} - \frac{3}{2}\Omega\,\delta v_r\,\hat{\boldsymbol{\phi}} + \frac{\mathrm{i}\boldsymbol{k}}{\rho}\cdot\left(C_{\mathrm{eff}}^2\,\delta\rho + \frac{\delta\boldsymbol{B}\cdot\boldsymbol{B}}{4\pi}\right) - \frac{\mathrm{i}k_z B_z}{4\pi\rho}\,\delta\boldsymbol{B} + 2\Omega\,\hat{\boldsymbol{z}}\times\delta\boldsymbol{v} = 0. \tag{3.38}$$

Now, the equivalent of Eq. (3.17) becomes:

$$\begin{aligned}\sigma_\eta\sigma\,\delta\boldsymbol{v} &- \frac{3}{2}\sigma_\eta\Omega\,\delta v_r\,\hat{\boldsymbol{\phi}} - \boldsymbol{k}k_z v_{\mathrm{A}z}\left(\boldsymbol{v}_{\mathrm{A}}\cdot\delta\boldsymbol{v} - \frac{3\Omega}{2\sigma_\eta}\,v_{\mathrm{A}\phi}\,\delta v_r\right) + \boldsymbol{k}K\left(\frac{\sigma_\eta}{\sigma}C_{\mathrm{eff}}^2 + v_{\mathrm{A}}^2\right)\delta v_r\\ &- Kk_z v_{\mathrm{A}z}\boldsymbol{v}_{\mathrm{A}}\,\delta v_r + k_z^2 v_{\mathrm{A}z}^2\left(\delta\boldsymbol{v} - \frac{3\Omega}{2\sigma_\eta}\,\delta v_r\,\hat{\boldsymbol{\phi}}\right) + 2\sigma_\eta\Omega\,\hat{\boldsymbol{z}}\times\delta\boldsymbol{v} = 0.\end{aligned} \tag{3.39}$$

In the same manner as we derived Eqs.(3.19), we now obtain

$$\left(\sigma_\eta\sigma + k_z^2 v_{\mathrm{A}z}^2 - \frac{Kk_r}{k^2}\sigma_\eta\sigma\right)\frac{k^2}{k_z^2}\,\delta v_r - 2\sigma_\eta\Omega\,\delta v_\phi = 0, \tag{3.40a}$$

$$(\sigma_\eta\sigma + k_z^2 v_{\mathrm{A}z}^2)\,\delta v_\phi + \left[\frac{\Omega\sigma_\eta}{2}\left(1 - 3\frac{k_z^2 v_{\mathrm{A}z}^2}{\sigma_\eta^2}\right) - Kk_z v_{\mathrm{A}\phi} v_{\mathrm{A}z}\right]\delta v_r = 0. \tag{3.40b}$$

From this two equations, the dispersion relation thus follows as:

$$\left(\tilde\sigma_\eta^2 - \frac{k_r K}{k^2}\sigma_\eta\sigma\right)\frac{k^2}{k_z^2}\,\tilde\sigma_\eta^2 + \Omega^2(\sigma_\eta^2 + k_z^2 v_{\mathrm{A}z}^2) - 4\Omega^2 k_z^2 v_{\mathrm{A}z}^2 - 2\Omega\sigma_\eta v_{\mathrm{A}\phi} v_{\mathrm{A}z} K k_z = 0; \tag{3.41}$$

with the definition $\tilde\sigma_\eta^2 \equiv \sigma_\eta\sigma + k_z^2 v_{\mathrm{A}z}^2$. The quantity K can again be calculated in the same manner as in the ideal case. We use the z-component of Eq. (3.39),

$$\sigma_\eta\sigma\,\delta v_z - k_z^2 v_{\mathrm{A}\phi} v_{\mathrm{A}z}\,\delta v_\phi + \frac{3\Omega}{2\sigma_\eta}k_z^2 v_{\mathrm{A}\phi} v_{\mathrm{A}z}\,\delta v_r + Kk_z\left(\frac{\sigma_\eta}{\sigma}C_{\mathrm{eff}}^2 + v_{\mathrm{A}\phi}^2\right)\delta v_r = 0, \tag{3.42}$$

as well as the analogue of Eq. (3.22),

$$\delta v_\phi = \left(-\frac{\Omega(s_\eta^2 + k_z^2 v_{\mathrm{A}z}^2)}{2\sigma_\eta\tilde\sigma_\eta^2} + 2\frac{\Omega}{\sigma_\eta}\frac{k_z^2 v_{\mathrm{A}z}^2}{\tilde\sigma_\eta^2} + \frac{Kk_z v_{\mathrm{A}\phi} v_{\mathrm{A}z}}{\tilde\sigma_\eta^2}\right)\delta v_r, \tag{3.43}$$

to obtain the following expression for K:

$$K = \frac{\tilde\sigma_\eta^2\sigma^2 k_r - \Omega\sigma k_z^3 v_{\mathrm{A}\phi} v_{\mathrm{A}z}(\sigma_\eta^2 + 3\tilde\sigma_\eta^2)/2\sigma_\eta^2}{\tilde\sigma_\eta^2(\sigma^2 + k_z^2 C_{\mathrm{eff}}^2) + \sigma^2 k_z^2 v_{\mathrm{A}\phi}^2}. \tag{3.44}$$

The only task that is left is the determination of the effective sound speed C_{eff}. Using the linearised equations (3.32) and (3.33), we find after some algebra

$$\frac{\delta p}{\delta\rho} = \frac{(1+\alpha_{\mathrm{P}}+\alpha_{\mathrm{F}})\left(\gamma + \frac{4E}{3e}\right) - \frac{4E}{3e}(1-3\alpha_{\mathrm{P}})(1+\alpha_{\mathrm{F}})}{1+\alpha_{\mathrm{P}}+\alpha_{\mathrm{F}}+4\alpha_{\mathrm{P}}\frac{E}{e}(1+\alpha_{\mathrm{F}})}\frac{p}{\rho}, \tag{3.45a}$$

$$\frac{\delta E}{\delta\rho} = \frac{1+4\alpha_{\mathrm{P}}\left(\gamma - 1 + \frac{4E}{3e}\right)}{1+\alpha_{\mathrm{P}}+\alpha_{\mathrm{F}}+4\alpha_{\mathrm{P}}\frac{E}{e}(1+\alpha_{\mathrm{F}})}\frac{E}{\rho}, \tag{3.45b}$$

from which C_{eff} immediately follows. The general dispersion that we have calculated, is applicable over a wide range of physical conditions, encompassing both the case of a gas-pressure dominated disc, such as a protoplanetary disc, and the opposite extreme of a radiation-pressure dominated system like an accretion disc around a black hole.

3.3.3 Eigenfunctions

The corresponding eigenfunctions in terms of the radial velocity perturbation δv_r are readily obtained and can be expressed as follows:

$$\delta\rho = -\mathrm{i}\rho\frac{K}{\sigma}\cdot\delta v_r, \tag{3.46a}$$

$$\delta v_\phi = \frac{\sigma}{2\Omega k_z^2}\left(k^2\frac{\tilde{\sigma}_\eta^2}{\sigma_\eta\sigma} - k_r K\right)\cdot\delta v_r, \tag{3.46b}$$

$$\delta v_z = \frac{K - k_r}{k_z}\cdot\delta v_r, \tag{3.46c}$$

$$\delta B_r = \mathrm{i}\frac{k_z B_z}{\sigma_\eta}\cdot\delta v_r, \tag{3.46d}$$

$$\delta B_\phi = \mathrm{i}\left\{\frac{k_z B_z}{2\Omega}\left(\frac{k^2}{k_z^2}\frac{\tilde{\sigma}_\eta^2}{\sigma_\eta^2} - \frac{\sigma}{\sigma_\eta}\frac{k_r K}{k_z^2} - 3\frac{\Omega^2}{\sigma_\eta^2}\right) - \frac{K B_\phi}{\sigma_\eta}\right\}\cdot\delta v_r, \tag{3.46e}$$

$$\delta B_z = -\mathrm{i}\frac{k_r B_z}{\sigma_\eta}\cdot\delta v_r, \tag{3.46f}$$

$$\delta p = -\mathrm{i}p\frac{(1+\alpha_\mathrm{P}+\alpha_\mathrm{F})\left(\gamma+\frac{4E}{3e}\right) - \frac{4E}{3e}(1-3\alpha_\mathrm{P})(1+\alpha_\mathrm{F})}{1+\alpha_\mathrm{P}+\alpha_\mathrm{F}+4\alpha_\mathrm{P}\frac{E}{e}(1+\alpha_\mathrm{F})}\frac{K}{\sigma}\cdot\delta v_r, \tag{3.46g}$$

$$\delta E = -\mathrm{i}E\frac{1+4\alpha_\mathrm{P}\left(\gamma-1+\frac{4E}{3e}\right)}{1+\alpha_\mathrm{P}+\alpha_\mathrm{F}+4\alpha_\mathrm{P}\frac{E}{e}(1+\alpha_\mathrm{F})}\frac{K}{\sigma}\cdot\delta v_r. \tag{3.46h}$$

In the incompressible ideal limit (setting $C_\mathrm{eff} = \infty$, $\eta = 0$) the eigenfunctions for the vertical modes ($k_r = 0$) take the following simple form:

$$\delta v_\phi = \frac{\tilde{\sigma}^2}{2\Omega\sigma}\cdot\delta v_r, \tag{3.47a}$$

$$\delta B_r = \mathrm{i}\frac{k_z B_z}{\sigma}\cdot\delta v_r, \tag{3.47b}$$

$$\delta B_\phi = \mathrm{i}\frac{k_z B_z}{2\Omega\sigma^2}\left(\tilde{\sigma}^2 - 3\Omega^2\right)\cdot\delta v_r, \tag{3.47c}$$

$$\delta\rho = \delta v_z = \delta B_z = \delta p = \delta E = 0. \tag{3.47d}$$

This solution has the peculiar property that it is an exact solution to the incompressible ideal MHD equations, since the nonlinear terms

$$\delta\boldsymbol{v}\cdot\boldsymbol{\nabla}\delta\boldsymbol{v}, \quad \delta\boldsymbol{B}\cdot\boldsymbol{\nabla}\delta\boldsymbol{B} \quad \text{and} \quad \boldsymbol{\nabla}\times(\delta\boldsymbol{v}\times\delta\boldsymbol{B}) \tag{3.48}$$

all vanish, as one can easily verify. As a consequence, the mode (3.47) has the potential to grow beyond the linear regime. However, the mode itself is subject to secondary non-axisymmetric instabilities related to the Kelvin-Helmholtz instability, that will eventually terminate its growth (Goodman and Xu, 1994). Since the mode develops characteristic channels it is also termed "channel mode".

3.4 Effect of Resistivity and Radiation Transport

3.4.1 Resistivity

Comparison to Resistive Dispersion Relations in the Literature

In the incompressible limit $C_{\mathrm{eff}} \to \infty$, the dispersion relation Eq. (3.41) reduces to the following simple form:

$$\frac{k^2}{k_z^2}\tilde{\sigma}_\eta^4 + \Omega^2(\sigma_\eta^2 + k_z^2 v_{\mathrm{A}z}^2) - 4\Omega^2 k_z^2 v_{\mathrm{A}z}^2 = 0. \tag{3.49}$$

By defining

$$\omega_\eta \equiv \mathrm{i}\sigma_\eta, \tag{3.50a}$$

$$\tilde{\omega}_\eta^2 \equiv -\tilde{\sigma}_\eta^2, \tag{3.50b}$$

$$D_{\mathrm{Jin}} = \frac{k^2}{k_z^2}\tilde{\omega}_\eta^4 - \Omega^2(\omega_\eta^2 - k_z^2 v_{\mathrm{A}z}^2) - 4\Omega^2 k_z^2 v_{\mathrm{A}z}^2; \tag{3.50c}$$

we do then recover the incompressible resistive dispersion relation

$$D_{\mathrm{Jin}} = 0 \tag{3.51}$$

of Jin (1996). Using the above definitions as well as Eq. (3.24c), we can write Eq. (3.41) as

$$\begin{aligned}\omega^2 &\left[(\omega_\eta\omega - k^2 v_{\mathrm{A}z}^2)(\omega_\eta\omega - k_z^2 v_{\mathrm{A}z}^2) - \Omega^2(\omega_\eta^2 - k_z^2 v_{\mathrm{A}z}^2) - 4\Omega^2 k_z^2 v_{\mathrm{A}z}^2\right] - k_z^2 C_{\mathrm{eff}}^2 D_{\mathrm{Jin}} \\ &- k^2 v_{\mathrm{A}\phi}^2 \left[\omega^2(\omega_\eta\omega - k_z^2 v_{\mathrm{A}z}^2) - \Omega^2\omega_\eta\omega\frac{k_z^2}{k^2}\right] - \frac{3}{2}\eta\omega^2\Omega k_r k_z k^2 v_{\mathrm{A}\phi} v_{\mathrm{A}z} = 0.\end{aligned} \tag{3.52}$$

Written in this form, it can be verified that our dispersion relation reduces to the isothermal dispersion relation derived by Sano and Miyama (1999), provided that we replace C_{eff} by the isothermal sound speed c_{s} (see their Eq. (17)).

Effect on Wavenumber Range

In order to see how resistivity effects the range of wavelength over which the instability operates, we set $\sigma = 0$ in Eq. (3.51) and obtain

$$k_{\mathrm{crit}} = \sqrt{3}\frac{\Omega}{v_{\mathrm{A}z}}\left(1 + \frac{\eta^2\Omega^2}{v_{\mathrm{A}z}^2}\frac{k^2}{k_z^2}\right)^{-1/2}. \tag{3.53}$$

Comparing this with Eq. (3.16), we see that resistivity reduces the range of unstable wavenumbers.

Effect on Growth Rates

In order to investigate the effect that resistivity has on the growth rates of the MRI modes, we differentiate Eq. (3.51) with respect to η and obtain

$$\frac{\mathrm{d}\sigma}{\mathrm{d}\eta} = -\frac{\tilde{\sigma}_\eta^2\sigma k^4 - \Omega^2\sigma_\eta k^2 k_z^2}{\tilde{\sigma}_\eta^2(\sigma + \sigma_\eta)k^2 + \Omega^2\sigma_\eta k_z^2} \tag{3.54}$$

from which it follows that $\mathrm{d}\sigma/\mathrm{d}\eta < 0$. This means that resistivity does not only change the range over which the MRI operates, but it also reduces the growth rates of the MRI modes.

3.4.2 Radiation Transport

Comparison to Radiative Dispersion Relations in the Literature

The effect of radiative diffusion on the growth of the MRI was considered in the paper by Blaes and Socrates (2001). Defining

$$\omega \equiv \mathrm{i}\sigma, \tag{3.55a}$$

$$\tilde{\omega}^2 = -\tilde{\sigma}^2, \tag{3.55b}$$

$$D_{\mathrm{ms}} \equiv \omega^2 - k_z^2(C_{\mathrm{eff}}^2 + v_{\mathrm{A}\phi}^2), \tag{3.55c}$$

$$D_{\mathrm{BH}} \equiv \frac{k^2}{k_z^2}\tilde{\omega}^4 - \Omega^2\tilde{\omega}^2 - 4\Omega^2 k_z^2 v_{\mathrm{A}z}^2; \tag{3.55d}$$

and setting $\eta = 0$, we can write Eq. (3.20) in a form similar to the dispersion relation given in their paper:

$$D_{\mathrm{ms}}D_{\mathrm{BH}} - k_z^2 v_{\mathrm{A}\phi}^2 v_{\mathrm{A}z}^2(k^2\tilde{\omega}^2 + 3k_z^2\Omega^2) - \frac{k_r^2}{k_z^2}\tilde{\omega}^2\omega^4 = 0. \tag{3.56}$$

Blaes and Socrates (2001) considered the case of a radiation-dominated disc where matter and radiation interact only by momentum exchange. This means that in order to compare our result with theirs, we should take the limit $\alpha_{\mathrm{P}} \to 0$. In this limit the effective sound speed C_{eff} becomes

$$C_{\mathrm{eff}}^2 = \frac{\gamma p}{\rho} + \frac{4\lambda E/3\rho}{1+\alpha_{\mathrm{F}}}. \tag{3.57}$$

In this particular limit (and with setting $\lambda = 1/3$, the dispersion relation Eq. (3.41) becomes indeed identical to the Blaes and Socrates (2001) dispersion relation.

Gas-pressure Dominated Disc

For a gas-pressure dominated disc, with strong coupling between matter and radiation (like in a protoplanetary disc), the effective sound speed follows by applying the limits $\alpha_{\mathrm{P}} \to \infty$ and $E/e \to 0$ to be

$$C_{\mathrm{eff}}^2 = \frac{\gamma + 4aT^4\alpha_{\mathrm{F}}/e}{1 + 4aT^4\alpha_{\mathrm{F}}/e}\frac{p}{\rho}. \tag{3.58}$$

By introducing a dimensional diffusion coefficient D via the definition

$$D \equiv 4\frac{aT^4}{e}\frac{\lambda c}{\kappa_{\mathrm{F}}\rho}, \tag{3.59}$$

we can write C_{eff} as the $C_{\mathrm{eff}} = \gamma_{\mathrm{eff}}\, p/\rho$ where the effective adiabatic index γ_{eff} is defined by

$$\gamma_{\mathrm{eff}} \equiv \frac{\gamma + k^2 D/\sigma}{1 + k^2 D/\sigma}. \tag{3.60}$$

With increasing radiative diffusion coefficient D, the effective adiabatic index is reduced towards the isothermal value $\gamma_{\mathrm{eff}} = 1$ for $D \to \infty$. This reduction happens mostly in the regime where the non-dimensional diffusion coefficient $k^2 D/\sigma \sim 1$, as can be seen from Fig. 3.3, where the effective adiabatic index is plotted as a function of D.

Since radiative diffusion enters only via the effective sound speed C_{eff}, it only changes the compressibility, and nothing else. This means that the range of wavenumbers over which the instability operates is not changed by radiative diffusion, however, since the compressibility is changed, the growth rates are also changed.

Change of Growth Rates Due to Radiative Diffusion

In order to quantify the effects of radiative diffusion on the growth rates, we first look at the vertical modes ($k_r = 0$) which have the largest growth rates. By differentiating the

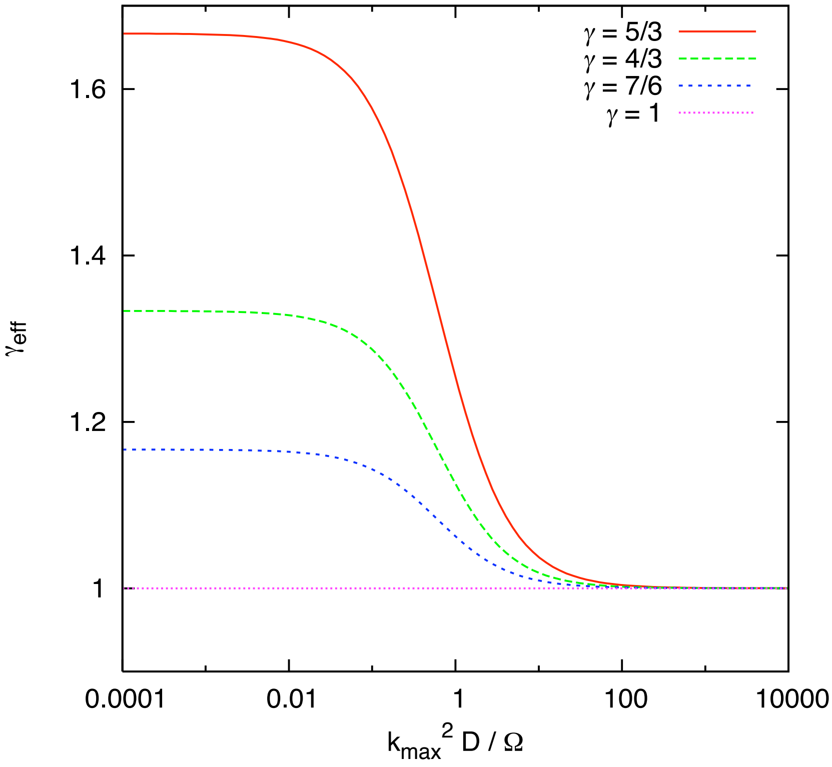

Fig. 3.3: Effective adiabatic index $\gamma_{\rm eff}$ as a function of $k^2_{\rm max}D/\Omega$, where $k_{\rm max}$ is the wavenumber of the fastest growing mode. In this plot, the azimuthal Alfvén speed is taken equal to the isothermal sound speed, $v^2_{{\rm A}\phi} = p/\rho$ (the global features of this plot are not sensitive to this particular choice).

dispersion relation (3.20) with respect to C_{eff}^{-2}, we find for the change of the growth rate σ with respect to a change in the effective sound speed:

$$\frac{1}{\sigma}\left(\frac{\mathrm{d}\sigma}{\mathrm{d}C_{\text{eff}}^{-2}}\right)_{C_{\text{eff}}=\infty} = -\frac{2k^2 v_{\mathrm{A}z}^2/\tilde{\sigma}^2}{1+2\tilde{\sigma}^2/\Omega^2}\, v_{\mathrm{A}\phi}^2. \tag{3.61}$$

From this result we conclude that for vertical modes the effect radiative diffusion leads to a decrease of the growth rates in the presence of a nonzero azimuthal field. For the fastest growing mode, which, for $C_{\text{eff}} = \infty$, has a growth rate $\sigma_{\max} = 3/4\,\Omega$ with wavenumber $k_{\max} = (\sqrt{15}/4)\,\Omega/v_{\mathrm{A}z}$, this means that the change $\Delta\sigma_{\max}$ in the growth rate as compared to the incompressible case $C_{\text{eff}} = \infty$ is approximately:

$$\frac{\Delta\sigma_{\max}}{\sigma_{\max}} \approx -\frac{1}{5}\frac{v_{\mathrm{A}\phi}^2}{C_{\text{eff}}^2}. \tag{3.62}$$

The relative dampening of the growth rates is, thus, in this case of the order of $O(v_{\mathrm{A}\phi}^2/C_{\text{eff}}^2)$. In Fig. 3.4 and also 3.5, main part, we plot the growth rates of vertical modes for different values of radiative diffusion coefficient D.

Curiously, if we consider non-vertical modes ($k_r \neq 0$) and a vanishing azimuthal field, we discover the opposite. In this case we find by an analogous analysis:

$$\frac{1}{\sigma}\left(\frac{\mathrm{d}\sigma}{\mathrm{d}C_{\text{eff}}^{-2}}\right)_{C_{\text{eff}}=\infty} = \frac{k_r^2}{2k_z^2}\frac{\tilde{\sigma}^2\sigma^2/k_z^2\Omega^2}{1+2k^2\tilde{\sigma}^2/k_z^2\Omega^2}. \tag{3.63}$$

The corresponding shift of the maximum growth rate becomes:

$$\frac{\Delta\sigma_{\max}}{\sigma_{\max}} \approx \frac{27k_r^2}{240k^2}\frac{v_{\mathrm{A}}^2}{C_{\text{eff}}^2}. \tag{3.64}$$

Plots of growth rates illustrating this effect can be found in the inset of Fig. 3.5. As long as the azimuthal magnetic field is subthermal, this effect should not be considered too important, because the growth of the MRI will be dominated by the fastest growing modes, which are in this case the vertical ones. In both cases considered, radiative diffusion contributes a fraction of $(\gamma p/\rho)/C_{\text{eff}}^2 - 1 = \gamma/\gamma_{\text{eff}} - 1$ to the total shift in the growth rates.

In gas-pressure dominated discs, the growth rates will never be dramatically changed by radiative diffusion, since the variation in C_{eff}^2 covers only a factor of γ. This is different from the situation encountered in a radiation dominated disc, where the analog of C_{eff}^2

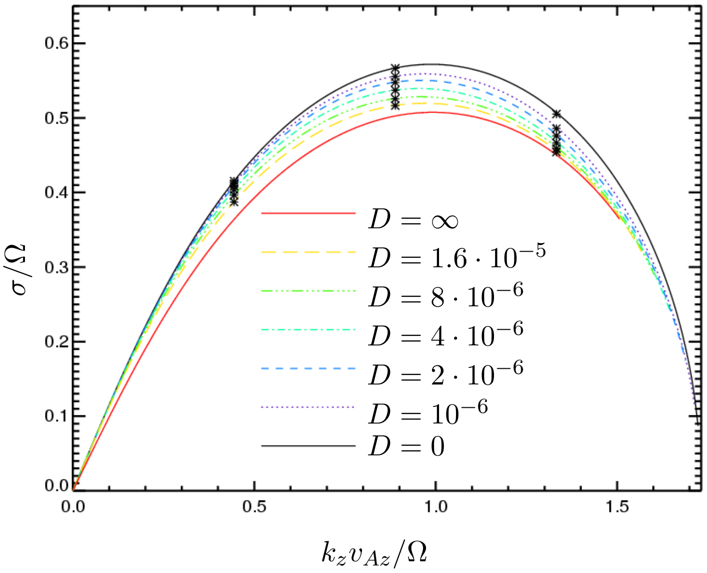

Fig. 3.4: Comparison of the numerical growth rates (black crosses) to the analytical results (lines). All simulations have $B_\phi = 25 B_z$ and a vertical magnetic field corresponding to a plasma beta $\beta = 400$. The curve for $D = \infty$ has been inserted to show the maximum possible change in the growth rates. The data has been obtained from simulations using an explicit numerical implementation of the radiation transport.

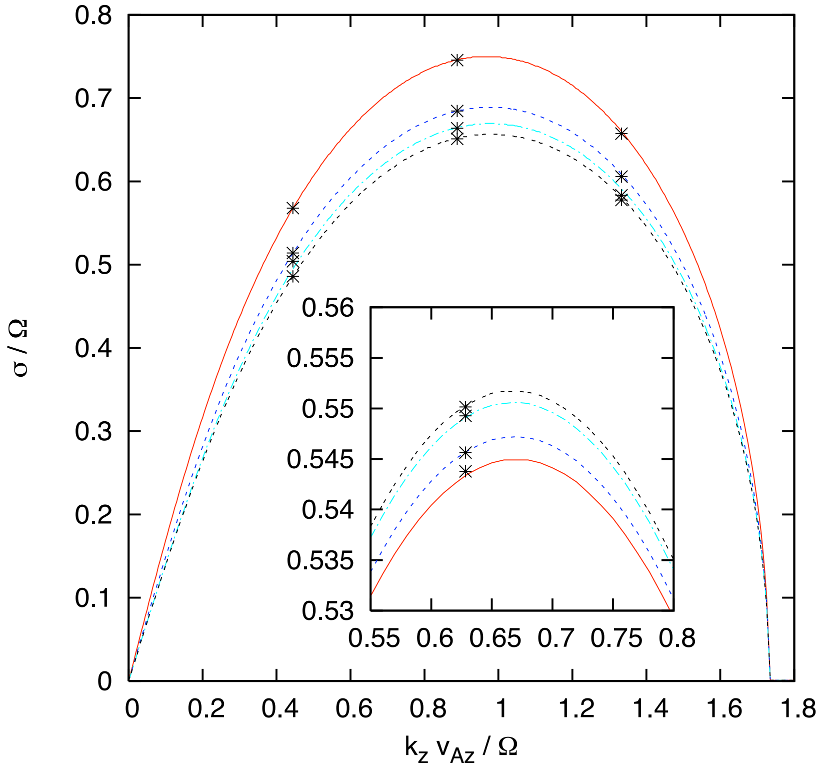

Fig. 3.5: *Change of MRI Growth Rates Due to Radiative Diffusion.* The curves in the main part of the graphic are for vertical modes ($k_r = 0$), where the growth rates are reduced by radiative diffusion. From top to bottom, they represent the following cases, $B_\phi = D = 0$; $B_\phi = 20B_z, D = 10^{-5}$; $B_\phi = 20B_z, D = 10^{-4}$; $B_\phi = 20B_z, D = 1$. The vertical magnetic field in terms of the plasma beta, $\beta = 2\mu_0 p/B^2$, is chosen such that $\beta = 400$, which means that $v_{Az}/\sqrt{p/\rho} \simeq 0.1$. The inset shows simulation results for non-vertical modes with no azimuthal magnetic field, where radiative diffusion increases the growth rates. We chose $k_r = k_z$, $B_\phi = 0$ and B_z such that $v_{Az} = \sqrt{p/\rho}$. From bottom to top, we have $D = 0$, $D = 10^{-5}$, $D = 10^{-4}$, $D = 1$. The asterisks represent the results of numerical simulations of single MRI modes, using an implicit implementation of radiation transport, which is described in more detail in Chap. 4.

may vary greatly. In the presence of a enough azimuthal field, the growth rates of the vertical modes may thus be severely reduced Turner et al. (2002).

In order to understand the change of the growth rates due to radiative diffusion in a qualitative manner, let us consider two cases: First, the case of a vertical mode ($\boldsymbol{k} = k_z \boldsymbol{e}_z$) in the presence of an azimuthal field. In the incompressible limit ($C_{\mathrm{eff}} \to \infty$), the motion of the fluid is confined to the plane perpendicular to the perturbation wavevector, so that $\delta v_z = 0$ (Fig. 3.6 (a)). When the compressibility is nonzero, the Lorentz force due to the azimuthal magnetic field causes a fluid flow in the vertical direction (Fig. 3.6 (b)). The higher the compressibility (and the smaller therefore the gas pressure), the more vertical will the velocity vector become. This in turn makes the buildup of the magnetic field less effective, resulting in a smaller growth rate. Radiative diffusion increases the compressibility, and therefore decreases the growth rate.

Next consider the case of a non-vertical mode ($k_r \neq 0$), with no background azimuthal field. If we now start with the limit of maximum compressibility ($C_{\mathrm{eff}} = 0$), we have $\delta v_z = 0$ (Fig. 3.6 (c)), since the z-component of the Lorentz force vanishes. When now increasing C_{eff}, the gas pressure will act to push the velocity vector into the plane perpendicular to the perturbation wavevector, this effect becoming stronger and stronger as the compressibility is further decreased (Fig. 3.6 (d)). Therefore, this time *increasing* the compressibility makes the buildup of the magnetic field more effective, which means that the growth rate increases due to radiative diffusion.

When considering the general case of a non-vertical mode in the presence of a nonzero azimuthal field, both effects are present and the result will be either an increase or a decrease of the growth rate, depending on the strength of the azimuthal field and the direction of the perturbation wavevector.

Numerical Simulations

In order to test our analytical calculations numerically, we set up 2D simulations of single MRI mode using the `CRONOS` code, a conservative MHD code which we describe in some detail in the next chapter. We initialise the simulations using the formula for the eigenfunctions given in Eqs. 3.46. The measured growth rates are plotted as asterisks in Figs. (3.4)+(3.5). As can be seen, the calculated growth rates are nicely reproduced by the numerical simulation, even in the case where the where the the shift in the growth rates is very small, as in the inset of Fig. (3.5).

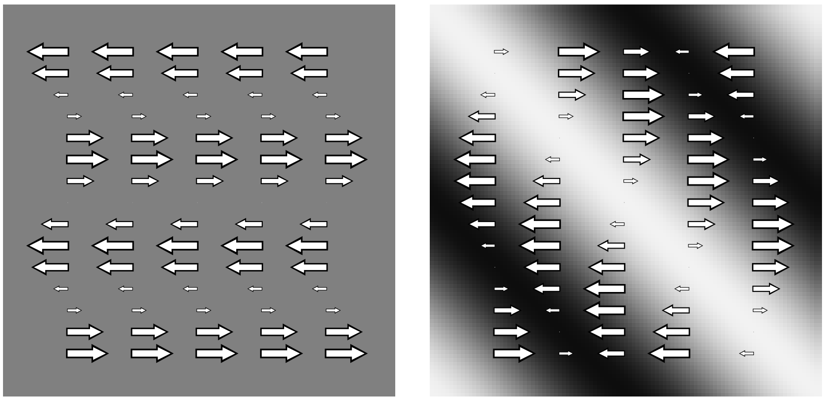

(a) k = kz, Ceff >> vA

(c) kr = kz, Ceff << vA

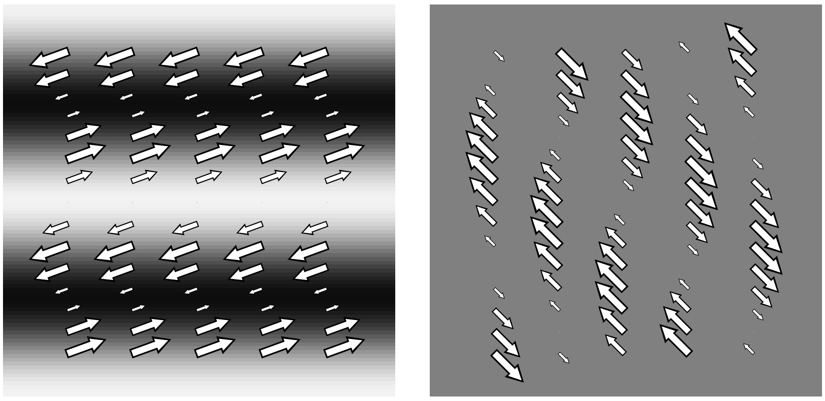

(b) k = kz, Ceff << vA

(d) kr = kz, Ceff >> vA

Fig. 3.6: Sketch of the MRI eigenmodes. Plotted is the density perturbation $\delta\rho$ (grayscale) and the velocity perturbation $\delta\boldsymbol{v}$ (arrows) in the r-z plane. The plots on the left show the case of a vertical mode in the presence of a background azimuthal magnetic field; where (a) corresponds to the incompressible case, while (b) is for finite compressibility. The plots on the right show the case of a non-vertical mode with $k_r = k_z$ where no azimuthal magnetic field is present. Here, (c) corresponds to the case of maximum compressibility and (d) to the incompressible case.

3.5 Summary

The topic of the present chapter was a linear analysis of the magnetorotational instability. The analysis was carried out by analytical means. Additionally, we performed numerical simulations of single MRI modes and measured the growth rates, thereby proving the correctness of the analytical calculation. We summarise the most important points of the work presented in this chapter:

- We have derived the most general MRI dispersion relation to date. We include both the effect of an Ohmic resistivity as well as an elaborate description of radiation transport. This makes our solution applicable to a wide range of astrophysical objects, including both the extremes of a cool protoplanetary disc and a hot accretion flow around a compact object.
- Radiative diffusion changes the growth rates of the MRI modes, leading to a decrease of the growth rates of the fastest growing modes. In addition, we find that there exists a class of modes whose growth rates are increased as a consequence of radiative diffusion. In contrast to this, resistivity always decreases the growth of the MRI for all modes.

In the next chapter, we will continue our study of the influence of radiation transport on the MRI by setting up 3D numerical simulations of magnetorotational turbulence. We will test different numerical schemes and check how much numerical effects affect the results. Finally, we will investigate how radiation transport affects the saturation level of the turbulence.

Chapter 4: Local Shearing Box Simulations

4.1 Numerical Schemes

While in principle it is always desirable to obtain an analytical solution to a particular problem, this is in practice often not possible. As we have seen in the last chapter, for example, the evolution of a single MRI mode can be calculated analytically, but this is no longer possible if we want to consider the problem of fully evolved 3D magnetorotational turbulence where many modes interact with each other in a non-linear fashion. Instead we have to resort to numerical methods, where the equations of magnetohydrodynamics are integrated numerically on a computer. With the exponential rise in computing power over the last decades, numerical methods have become ever more important in many fields of science, and astrophysics is no exception here. Concerning the problem of magnetorotational turbulence in accretion discs, numerical simulations are almost the only means of investigation, since analytical approaches are very limited and certain physical conditions that are present in accretion discs (like the very high Reynolds numbers) cannot be reproduced in laboratory experiments. Therefore, the rest of our work is reserved to the numerical solution of the fluid equations that have been derived in Chap. 1.

4.1.1 Finite Difference vs. Finite Volume

The numerical algorithms that are employed to solve the magnetohydrodynamical equations can be grouped into two classes, namely finite-difference and finite-volume schemes.[1] In finite-difference codes, the derivatives appearing in partial differential equations are replaced by finite differences. Such codes usually have to include some form of artificial viscosity for the proper treatment of shocks (von Neumann and Richtmyer, 1950).

---

[1] In addition to these two groups there exist also spectral codes which solve the incompressible MHD equations in Fourier space. While these codes are very important for the study of incompressible turbulence, their applicability to actual astrophysical problems is, however, quite limited.

Finite-volume schemes, on the other hand, are based on the *integral* formulation of a set of conservation equations, rather than the original differential form. This means that they are naturally well suited for calculating weak solutions to the original partial differential equations and usually need no artificial viscosity to get shock speeds and positions right. Moreover, they have the nice property of automatically conserving the values of the conserved variables to round-off error. Finite-difference codes are still widely used for astrophysical problems, however, the more modern finite-volume codes become more and more common and will likely play a prominent role in the foreseeable future.

4.1.2 The ZEUS code

The `ZEUS` code invented by Stone and Norman (1992) is the most widely used finite-difference code in the field of theoretical astrophysics. The code solves the equations of ideal magnetohydrodynamics, i.e. Eqs. (2.27a), (2.27b), (2.27c) and (2.32) written in the form

$$\frac{\partial \rho}{\partial t} + \boldsymbol{\nabla} \cdot (\rho \boldsymbol{v}) = 0, \tag{4.1a}$$

$$\rho \frac{\partial \boldsymbol{v}}{\partial t} + \boldsymbol{v} \cdot \boldsymbol{\nabla} \boldsymbol{v} = -\nabla p + \frac{(\boldsymbol{\nabla} \times \boldsymbol{B}) \times \boldsymbol{B}}{4\pi} - \rho \nabla \Phi - \boldsymbol{\nabla} \cdot \boldsymbol{Q} \tag{4.1b}$$

$$\frac{\partial e}{\partial t} + \boldsymbol{v} \cdot \boldsymbol{\nabla} e = -p \nabla \cdot \boldsymbol{v} - \boldsymbol{Q} : \boldsymbol{\nabla} \boldsymbol{v}, \tag{4.1c}$$

$$\frac{\partial \boldsymbol{B}}{\partial t} = \nabla \times (\boldsymbol{v} \times \boldsymbol{B}), \tag{4.1d}$$

where the tensor $\boldsymbol{Q}$ describes the artificial viscosity. `ZEUS` uses a staggered mesh, where the scalar variables (ρ and e) are located at the cell centers and the vector variables ($\boldsymbol{v}$ and $\boldsymbol{B}$) are defined at cell interfaces. The code uses operator splitting to calculate the solution in two steps, namely the *source* step, where the equations

$$\rho \frac{\partial \boldsymbol{v}}{\partial t} = -\nabla p + \frac{(\boldsymbol{\nabla} \times \boldsymbol{B}) \times \boldsymbol{B}}{4\pi} - \rho \nabla \Phi - \boldsymbol{\nabla} \cdot \boldsymbol{Q}, \tag{4.2a}$$

$$\frac{\partial e}{\partial t} = -p \nabla \cdot \boldsymbol{v} - \boldsymbol{Q} : \boldsymbol{\nabla} \boldsymbol{v}, \tag{4.2b}$$

are solved, and the *transport* step, where the advection of the fluid variables is calculated based on the integral equations

$$\frac{\mathrm{d}}{\mathrm{d}t}\int_V \rho \,\mathrm{d}V = -\int_{\partial V} \rho \boldsymbol{v} \cdot \mathrm{d}\boldsymbol{A}, \tag{4.3a}$$

$$\frac{\mathrm{d}}{\mathrm{d}t}\int_V \rho \boldsymbol{v} \,\mathrm{d}V = -\int_{\partial V} \rho \boldsymbol{v}\boldsymbol{v} \cdot \mathrm{d}\boldsymbol{A}, \tag{4.3b}$$

$$\frac{\mathrm{d}}{\mathrm{d}t}\int_V e \,\mathrm{d}V = -\int_{\partial V} e \boldsymbol{v} \cdot \mathrm{d}\boldsymbol{A}; \tag{4.3c}$$

where V denotes the volume of one grid cell. The way the transport step is performed means that although technically `ZEUS` is a finite-difference code, it does also contain elements of a finite-volume code. The `ZEUS` code is characterised by a high degree of simplicity, robustness and speed, making it ideally suited for astrophysical applications. A special advantage of the `ZEUS` code is the fact that it's operator split nature makes it very easy to add new physics, something that in general cannot be said of finite-volume codes. For some applications, a disadvantage of the `ZEUS` code is that in its original form it is not energy conserving: Kinetic and magnetic energy that is lost on the grid scale due to numerical dissipation simply gets lost, while in a real physical system the energy would cascade down to smaller scales and finally be converted into heat. For our project, where we intend to calculate the transport of energy that comes from turbulent dissipation, energy conservation is essential, so the `ZEUS` code is not well suited for the problem we have in mind.[2] However, we will nevertheless use the `ZEUS` code for test simulations in order to compare the results of different codes.

4.1.3 A Simple Finite Volume Scheme

The MHD Equations in Conservative Form

We will now proceed to derive a simple finite-volume scheme suitable for the problem that we are considering. To do so, we first have to write the MHD equations[3] in the form of a system of conservation laws, i.e.

$$\frac{\partial \mathbf{u}}{\partial t} + \frac{\partial \mathbf{f}_x}{\partial x} + \frac{\partial \mathbf{f}_y}{\partial y} + \frac{\partial \mathbf{f}_z}{\partial z} = 0, \tag{4.4}$$

---

[2] Note, however, that the `ZEUS` code can be changed so that part or all of the dissipated energy is correctly transformed into heat, see, for example Turner (2004); Hirose et al. (2006).

[3] For simplicity, here we restrict ourselves to the ideal MHD equations, i.e. Eqs. (2.42) with $\eta = 0$ and the radiative diffusion term $\boldsymbol{\nabla} \cdot \boldsymbol{F}$ dropped. The radiation transport is treated implicitly anyway, see Sec. 4.1.6

where $\mathbf{u}$ denotes the vector of conserved variables and $\mathbf{f}_x$, $\mathbf{f}_y$, $\mathbf{f}_z$ are the fluxes. The continuity and induction equations,

$$\frac{\partial \rho}{\partial t} + \boldsymbol{\nabla} \cdot (\rho \boldsymbol{v}) = 0, \tag{4.5}$$

$$\frac{\partial \boldsymbol{B}}{\partial t} = \boldsymbol{\nabla} \times (\boldsymbol{v} \times \boldsymbol{B}), \tag{4.6}$$

already have the desired form. By adding the continuity equation to Eq. (2.27b) and applying standard vector identities, we can also write the momentum equation in an conservative form:

$$\frac{\partial (\rho \boldsymbol{v})}{\partial t} + \boldsymbol{\nabla} \cdot \left[\rho \boldsymbol{v}\boldsymbol{v} + p_{\mathrm{tot}} \mathsf{I} - \frac{\boldsymbol{B}\boldsymbol{B}}{4\pi} \right] = 0, \tag{4.7}$$

where $p_{\mathrm{tot}} \equiv p + B^2/8\pi$. Defining the total energy E_{tot} as $E_{\mathrm{tot}} = e + \rho v^2/2 + B^2/8\pi$ and multiplying Eq. (4.7) with $\boldsymbol{v}$ and Eq. (4.6) with $\boldsymbol{B}$ and adding the two resulting equations to the thermal energy equation, we get

$$\frac{\partial E_{\mathrm{tot}}}{\partial t} + \boldsymbol{\nabla} \cdot \left[(E_{\mathrm{tot}} + p_{\mathrm{tot}})\, \boldsymbol{v} - \frac{\boldsymbol{B}(\boldsymbol{B} \cdot \boldsymbol{v})}{4\pi} \right] = 0. \tag{4.8}$$

Note that by including the radiation transport term $\boldsymbol{\nabla} \cdot \boldsymbol{F}$ in the thermal energy equation, and by adding the gravitational energy to the definition of E_{tot} we could have arrived at a conservative formulation of the total energy equation including radiation transport and gravity. However, we prefer to include these terms later as source terms.

We have now indeed arrived at a conservative formulation of the ideal MHD equations, i.e. we can write them in the form of Eq. (4.4), with the the vector of conserved variables, $\mathbf{u}$, defined as

$$\mathbf{u} \equiv \begin{bmatrix} \rho \\ \rho v_x \\ \rho v_y \\ \rho v_z \\ B_x \\ B_y \\ B_z \\ E_{\mathrm{tot}} \end{bmatrix}, \tag{4.9}$$

and the fluxes $\mathbf{f}_x, \mathbf{f}_y, \mathbf{f}_z$ given by

$$\mathbf{f}_x \equiv \begin{bmatrix} \rho v_x \\ \rho v_x^2 + p_{\text{tot}} - B_x^2 \\ \rho v_x v_y - B_x B_y \\ \rho v_x v_z - B_x B_z \\ 0 \\ B_y v_x - B_x v_y \\ B_z v_x - B_x v_z \\ (E_{\text{tot}} + p_{\text{tot}}) v_x - (\boldsymbol{B} \cdot \boldsymbol{v}) B_x \end{bmatrix}, \tag{4.10}$$

$$\mathbf{f}_y \equiv \begin{bmatrix} \rho v_y \\ \rho v_y v_x - B_y B_x \\ \rho v_y^2 + p_{\text{tot}} - B_y^2 \\ \rho v_y v_z - B_y B_z \\ B_x v_y - B_y v_x \\ 0 \\ B_z v_y - B_y v_z \\ (E_{\text{tot}} + p_{\text{tot}}) v_y - (\boldsymbol{B} \cdot \boldsymbol{v}) B_y \end{bmatrix}, \tag{4.11}$$

$$\mathbf{f}_z \equiv \begin{bmatrix} \rho v_z \\ \rho v_z v_x - B_z B_x \\ \rho v_z v_y - B_z B_y \\ \rho v_z^2 + p_{\text{tot}} - B_z^2 \\ B_x v_z - B_z v_x \\ B_y v_z - B_z v_y \\ 0 \\ (E_{\text{tot}} + p_{\text{tot}}) v_z - (\boldsymbol{B} \cdot \boldsymbol{v}) B_z \end{bmatrix}. \tag{4.12}$$

1D Version of the Scheme

For simplicity, let us begin with the 1D version of Eq. (4.4), i.e. we want to discretise the equation

$$\frac{\partial \mathbf{u}}{\partial t} + \frac{\partial \mathbf{f}}{\partial x} = 0, \tag{4.13}$$

with $\mathbf{f} \equiv \mathbf{f}_x$. Integrating Eqs. (4.4) over one interval in space $\mathcal{I} = [x_{\text{l}}, x_{\text{r}}]$ and one interval in time $[t_n, t_{n+1}]$ yields:

$$\mathbf{u}_{\mathcal{I}}^{n+1} = \mathbf{u}_{\mathcal{I}}^{n} + \frac{\delta t}{\delta x} \big(\mathbf{f}_{\text{r}}^{n+\frac{1}{2}} - \mathbf{f}_{\text{l}}^{n+\frac{1}{2}} \big), \tag{4.14}$$

where $\delta x \equiv x_\mathrm{r} - x_\mathrm{l}$ and $\delta t \equiv t_{n+1} - t_n$. The sliding average $\mathbf{u}^n_\mathcal{I}$ is defined as

$$\mathbf{u}^n_\mathcal{I} \equiv \frac{1}{x_\mathrm{r} - x_\mathrm{l}} \int_\mathcal{I} \mathbf{u}(x, t_n)\,\mathrm{d}x \tag{4.15}$$

and the time-averaged fluxes $\mathbf{f}_\mathrm{l}^{n+1/2}$ and $\mathbf{f}_\mathrm{r}^{n+1/2}$ through the left/right boundary of the cell are given by

$$\mathbf{f}_\mathrm{l}^{n+\frac{1}{2}} \equiv \int_{t_n}^{t_{n+1}} \mathbf{f}(x_\mathrm{l}, t)\,\mathrm{d}t, \tag{4.16}$$

$$\mathbf{f}_\mathrm{r}^{n+\frac{1}{2}} \equiv \int_{t_n}^{t_{n+1}} \mathbf{f}(x_\mathrm{r}, t)\,\mathrm{d}t. \tag{4.17}$$

Note that Eq. (4.14) is an exact expression and does not involve any approximations. Starting from the volume averages

$$\mathbf{u}^n_i = \mathbf{u}^n_{[x_{i-\frac{1}{2}}, x_{i+\frac{1}{2}}]}, \tag{4.18}$$

we perform a piecewise linear reconstruction[4]

$$\mathbf{u}^n(x) = \mathbf{u}^n_i + s^n_i(x - x_i), \quad x_{i-\frac{1}{2}} < x < x_{i+\frac{1}{2}} \quad \forall i. \tag{4.19}$$

For the stability of the numerical scheme it is important that the reconstruction does not introduce any new extrema, a property that is usually achieved using suitable slope limiters (LeVeque 2002). Next, we want to advance the solution in time over a small interval δt, using Eq. (4.14). The reconstruction Eq. (4.19) contains discontinuities at the interfaces $x_{i\pm1/2}$, which propagate away from the interface. It is easy to provide upper bounds for the right- and left-sided propagation speeds, which we denote by $a^+_{i\pm1/2}$ and $a^-_{i\pm1/2}$, respectively (Kurganov et al., 2001). Following Kurganov et al. (2001), we define

$$x_{i+\frac{1}{2},\mathrm{l}} \equiv x_{i+\frac{1}{2}} + a^-_{i+\frac{1}{2}}\delta t, \tag{4.20}$$

$$x_{i+\frac{1}{2},\mathrm{r}} \equiv x_{i+\frac{1}{2}} + a^+_{i+\frac{1}{2}}\delta t. \tag{4.21}$$

The solution is thus continuous in the intervals $\mathcal{I}_i \equiv [x_{i-1/2,\mathrm{r}}, x_{i+1/2,\mathrm{l}}]$, but contains discontinuities in the intervals $\mathcal{I}_{i+1/2} \equiv [x_{i+1/2,\mathrm{l}}, x_{i+1/2,\mathrm{r}}]$ (cf. Fig. 4.1). Since the solution is continuous at the boundaries of both the intervals $\mathcal{I}_i$ and $\mathcal{I}_{i+1/2}$, we can apply Eq. (4.14)

---

[4] Actually, the following derivation is not restricted to a reconstruction of second order, but may be a conservative, non-oscillatory polynomial of any order (Kurganov et al., 2001).

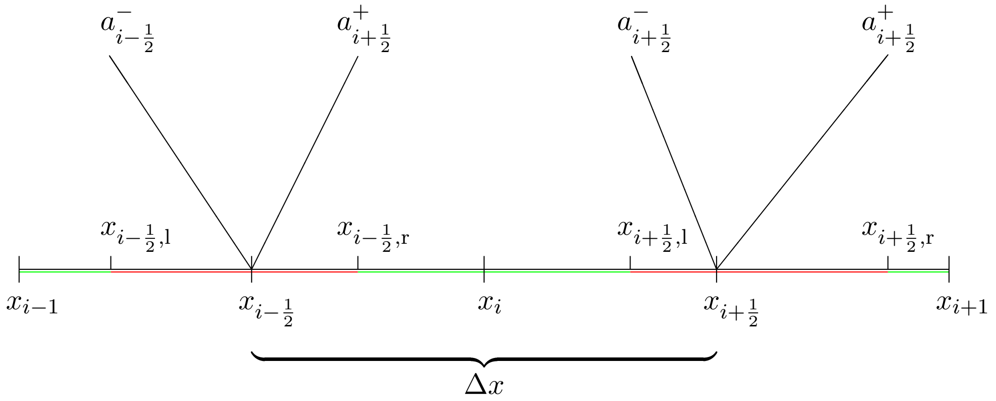
$a^-_{i-\frac{1}{2}}$
$a^+_{i+\frac{1}{2}}$
$a^-_{i+\frac{1}{2}}$
$a^+_{i+\frac{1}{2}}$
$x_{i-\frac{1}{2},\mathrm{l}}$
$x_{i-\frac{1}{2},\mathrm{r}}$
$x_{i+\frac{1}{2},\mathrm{l}}$
$x_{i+\frac{1}{2},\mathrm{r}}$
x_{i-1}
$x_{i-\frac{1}{2}}$
x_i
$x_{i+\frac{1}{2}}$
x_{i+1}
Δx

Fig. 4.1: Sketch showing the structure of the computational grid. The cell centers are labeled x_i, where the index i runs from 1 to N, the number of grid points. Cell faces are labeled using fractional indices, such that $x_{i\pm1/2}$ refers to the point at $x_i \pm \Delta x/2$, where Δx denotes the width of one grid cell. The solution is continuous in the green intervals but may contain discontinuities in the red intervals. These discontinuities propagate away from the interface $x_{i+1/2}$ with signal speeds $a^{\pm}_{i+1/2}$. The location of these discontinuities at a certain instant in time is denoted by $x_{i+1/2,\mathrm{l/r}}$.

on both intervals $\mathcal{I}_i$ and $\mathcal{I}_{i+1/2}$. We will denote the corresponding volume averages over the interval $\mathcal{I}_i$ and $\mathcal{I}_{i+1/2}$ by

$$\tilde{\mathbf{u}}_i(t) \equiv \mathbf{u}_{\mathcal{I}_i}(t) \quad \text{and} \quad \tilde{\mathbf{u}}_{i+\frac{1}{2}}(t) \equiv \mathbf{u}_{\mathcal{I}_{i+\frac{1}{2}}}(t) \tag{4.22}$$

respectively. Using now the decomposition

$$\mathbf{u}_i^{n+1} = \frac{1}{\Delta x}\int_{x_{i-\frac{1}{2}}}^{x_{i-\frac{1}{2},\mathrm{r}}} \mathbf{u}^{n+1}(x)\,\mathrm{d}x + \frac{x_{i+\frac{1}{2},\mathrm{l}} - x_{i-\frac{1}{2},\mathrm{r}}}{\Delta x}\mathbf{u}_i^n + \frac{1}{\Delta x}\int_{x_{i+\frac{1}{2},\mathrm{l}}}^{x_{i+\frac{1}{2}}} \mathbf{u}^{n+1}(x)\,\mathrm{d}x, \tag{4.23}$$

we can calculate the time derivative of $\mathbf{u}_i$,

$$\begin{aligned}\frac{\mathrm{d}}{\mathrm{d}t}\mathbf{u}_i(t) &= \lim_{\Delta t\to 0}\frac{\mathbf{u}_i^{n+1} - \mathbf{u}_i^n}{\Delta t}\\ &= \frac{a^+_{i-\frac{1}{2}}}{\Delta x}\lim_{\Delta t\to 0}\tilde{\mathbf{u}}^{n+1}_{i-\frac{1}{2}} + \lim_{\Delta t\to 0}\frac{1}{\Delta t}\left(\frac{x^n_{i+\frac{1}{2},\mathrm{l}} - x^n_{i-\frac{1}{2},\mathrm{r}}}{\Delta x}\tilde{\mathbf{u}}_i^{n+1} - \mathbf{u}_i^n\right) + \frac{a^-_{i+\frac{1}{2}}}{\Delta x}\lim_{\Delta t\to 0}\tilde{\mathbf{u}}^{n+1}_{i+\frac{1}{2}}.\end{aligned} \tag{4.24}$$

The three limits in this equation can be calculated independently. For the term in the middle, we get (using Eq. (4.14) with $\mathcal{I} = \mathcal{I}_i$)

$$\begin{aligned}\lim_{\Delta t\to 0}\frac{1}{\Delta t}\left(\frac{x^n_{i+\frac{1}{2},\mathrm{l}} - x^n_{i-\frac{1}{2},\mathrm{r}}}{\Delta x}\tilde{\mathbf{u}}_i^{n+1} - \mathbf{u}_i^n\right) &= -\lim_{\Delta t\to 0}\frac{1}{\Delta t\Delta x}\int_{x_{i-\frac{1}{2}}}^{x_{i-\frac{1}{2},\mathrm{r}}}\mathbf{u}^n(x)\,\mathrm{d}x\\ -\lim_{\Delta t\to 0}\frac{1}{\Delta t\Delta x} + \int_{x_{i+\frac{1}{2},\mathrm{l}}}^{x_{i+\frac{1}{2}}}\mathbf{u}^n(x)\,\mathrm{d}x - \lim_{\Delta t\to 0}\frac{1}{\Delta t\Delta x}&\int_{t_n}^{t_{n+1}}\Big[\mathbf{f}\big(\mathbf{u}_{x_{i+\frac{1}{2},\mathrm{l}}}(t)\big) - \mathbf{f}\big(\mathbf{u}_{x_{i-\frac{1}{2},\mathrm{r}}}(t)\big)\Big]\,\mathrm{d}t.\end{aligned} \tag{4.25}$$

Introducing the following shorthand notation for the interface states to the left/right side of the interface at $x_{i+1/2}$,

$$\mathbf{u}^-_{i+\frac{1}{2}} \equiv \mathbf{u}_i^n + s_i^n\frac{\Delta x}{2}, \tag{4.26}$$

$$\mathbf{u}^+_{i+\frac{1}{2}} \equiv \mathbf{u}_{i+1}^n - s_{i+1}^n\frac{\Delta x}{2}, \tag{4.27}$$

the result can be expressed as

$$= \frac{a^-_{i+\frac{1}{2}}\mathbf{u}^-_{i+\frac{1}{2}} - a^+_{i-\frac{1}{2}}\mathbf{u}^+_{i-\frac{1}{2}}}{\Delta x} - \frac{\mathbf{f}\big(\mathbf{u}^-_{i+\frac{1}{2}}\big) - \mathbf{f}\big(\mathbf{u}^+_{i-\frac{1}{2}}\big)}{\Delta x}. \tag{4.28}$$

The calculation of the other two limits proceeds in a similar fashion, where again we make use of Eq. (4.14), this time with $I = I_{i+1/2}$:

$$\begin{aligned}\lim_{\Delta t\to 0}\tilde{\mathbf{u}}^{n+1}_{i-\frac{1}{2}} &= \lim_{\Delta t\to 0}\frac{1}{x_{i-\frac{1}{2},\mathrm{r}}-x_{i-\frac{1}{2},\mathrm{l}}}\left[\int_{x_{i-\frac{1}{2},\mathrm{l}}}^{x_{i-\frac{1}{2}}}\mathbf{u}^n(x)\,\mathrm{d}x+\int_{x_{i-\frac{1}{2}}}^{x_{i-\frac{1}{2},\mathrm{r}}}\mathbf{u}^n(x)\,\mathrm{d}x\right]\\ &\quad-\lim_{\Delta t\to 0}\frac{1}{\Delta x}\int_{t_n}^{t_{n+1}}\Big[\mathbf{f}(\mathbf{u}_{x_{i-\frac{1}{2},\mathrm{r}}}(t))-\mathbf{f}(\mathbf{u}_{x_{i-\frac{1}{2},\mathrm{l}}}(t))\Big]\,\mathrm{d}t\\ &=\frac{a^+_{i-\frac{1}{2}}\mathbf{u}^+_{i-\frac{1}{2}}-a^-_{i-\frac{1}{2}}\mathbf{u}^-_{i-\frac{1}{2}}}{a^+_{i-\frac{1}{2}}-a^-_{i-\frac{1}{2}}}-\frac{\mathbf{f}(\mathbf{u}^+_{i-\frac{1}{2}})-\mathbf{f}(\mathbf{u}^-_{i-\frac{1}{2}})}{a^+_{i-\frac{1}{2}}-a^-_{i-\frac{1}{2}}},\end{aligned} \tag{4.29}$$

and, analogously,

$$\lim_{\Delta t\to 0}\tilde{\mathbf{u}}^{n+1}_{i+\frac{1}{2}}=\frac{a^+_{i+\frac{1}{2}}\mathbf{u}^+_{i+\frac{1}{2}}-a^-_{i+\frac{1}{2}}\mathbf{u}^-_{i+\frac{1}{2}}}{a^+_{i+\frac{1}{2}}-a^-_{i+\frac{1}{2}}}-\frac{\mathbf{f}(\mathbf{u}^+_{i+\frac{1}{2}})-\mathbf{f}(\mathbf{u}^-_{i+\frac{1}{2}})}{a^+_{i+\frac{1}{2}}-a^-_{i+\frac{1}{2}}}. \tag{4.30}$$

Substitution of Eqs. (4.28),(4.29) and (4.30) completes the calculation of the time derivative of $\mathbf{u}_i(t)$, which can be expressed in conservative form as

$$\frac{\mathrm{d}}{\mathrm{d}t}\mathbf{u}_i(t)=-\frac{\boldsymbol{\mathcal{F}}_{i+\frac{1}{2}}(t)-\boldsymbol{\mathcal{F}}_{i-\frac{1}{2}}(t)}{\Delta x}, \tag{4.31}$$

where the numerical fluxes $\boldsymbol{\mathcal{F}}_{i+\frac{1}{2}}$ are defined by

$$\boldsymbol{\mathcal{F}}_{i+\frac{1}{2}}(t)\equiv\frac{a^+_{i+\frac{1}{2}}\mathbf{f}(\mathbf{u}^-_{i+\frac{1}{2}})-a^-_{i+\frac{1}{2}}\mathbf{f}(\mathbf{u}^+_{i+\frac{1}{2}})}{a^+_{i+\frac{1}{2}}-a^-_{i+\frac{1}{2}}}+\frac{a^+_{i+\frac{1}{2}}a^-_{i+\frac{1}{2}}}{a^+_{i+\frac{1}{2}}-a^-_{i+\frac{1}{2}}}\left(\mathbf{u}^+_{i+\frac{1}{2}}-\mathbf{u}^-_{i+\frac{1}{2}}\right). \tag{4.32}$$

By replacing the differentials on the left hand side of Eq. (4.31) with finite differences, we arrive at the following scheme:

$$\mathbf{u}^{n+1}_i=\mathbf{u}^n_i-\frac{\Delta t}{\Delta x}\big[\boldsymbol{\mathcal{F}}_{i+\frac{1}{2}}(t)-\boldsymbol{\mathcal{F}}_{i-\frac{1}{2}}(t)\big]. \tag{4.33}$$

Generalisation to 3D

The scheme Eq. (4.33) can be straightforwardly generalised to multiple dimensions. Since this does not introduce any new concepts, we will omit the somewhat lengthy derivation here. Details can be found in Kurganov et al. (2001). The result is that Eq. (4.33) is replaced by

$$\begin{aligned}\mathbf{u}_i^{n+1} = \mathbf{u}_i^n &- \frac{\Delta t}{\Delta x}\left[\boldsymbol{\mathcal{F}}^x_{i+\frac{1}{2}jk}(t) - \boldsymbol{\mathcal{F}}^x_{i-\frac{1}{2}jk}(t)\right] \\ &- \frac{\Delta t}{\Delta y}\left[\boldsymbol{\mathcal{F}}^y_{ij+\frac{1}{2}k}(t) - \boldsymbol{\mathcal{F}}^y_{ij-\frac{1}{2}k}(t)\right] - \frac{\Delta t}{\Delta z}\left[\boldsymbol{\mathcal{F}}^z_{ijk+\frac{1}{2}}(t) - \boldsymbol{\mathcal{F}}^z_{ijk-\frac{1}{2}}(t)\right]\Big], \end{aligned} \tag{4.34}$$

where

$$\begin{aligned}\boldsymbol{\mathcal{F}}^x_{i+\frac{1}{2}jk}(t) &= \frac{a^+_{i+\frac{1}{2}jk}\mathbf{f}(\mathbf{u}^-_{i+\frac{1}{2}jk}) - a^-_{i+\frac{1}{2}jk}\mathbf{f}(\mathbf{u}^+_{i+\frac{1}{2}jk})}{a^+_{i+\frac{1}{2}jk} - a^-_{i+\frac{1}{2}jk}} + \frac{a^+_{i+\frac{1}{2}jk}a^-_{i+\frac{1}{2}jk}}{a^+_{i+\frac{1}{2}jk} - a^-_{i+\frac{1}{2}jk}}\left(\mathbf{u}^+_{i+\frac{1}{2}jk} - \mathbf{u}^-_{i+\frac{1}{2}jk}\right), \\ \boldsymbol{\mathcal{F}}^y_{ij+\frac{1}{2}k}(t) &= \frac{b^+_{ij+\frac{1}{2}k}\mathbf{f}(\mathbf{u}^-_{ij+\frac{1}{2}k}) - b^-_{ij+\frac{1}{2}k}\mathbf{f}(\mathbf{u}^+_{ij+\frac{1}{2}k})}{b^+_{ij+\frac{1}{2}k} - b^-_{ij+\frac{1}{2}k}} + \frac{b^+_{ij+\frac{1}{2}k}b^-_{ij+\frac{1}{2}k}}{b^+_{ij+\frac{1}{2}k} - b^-_{ij+\frac{1}{2}k}}\left(\mathbf{u}^+_{ij+\frac{1}{2}k} - \mathbf{u}^-_{ij+\frac{1}{2}k}\right), \\ \boldsymbol{\mathcal{F}}^z_{ijk+\frac{1}{2}}(t) &= \frac{c^+_{ijk+\frac{1}{2}}\mathbf{f}(\mathbf{u}^-_{ijk+\frac{1}{2}}) - c^-_{ijk+\frac{1}{2}}\mathbf{f}(\mathbf{u}^+_{ijk+\frac{1}{2}})}{c^+_{ijk+\frac{1}{2}} - c^-_{ijk+\frac{1}{2}}} + \frac{c^+_{ijk+\frac{1}{2}}c^-_{ijk+\frac{1}{2}}}{c^+_{ijk+\frac{1}{2}} - c^-_{ijk+\frac{1}{2}}}\left(\mathbf{u}^+_{ijk+\frac{1}{2}} - \mathbf{u}^-_{ijk+\frac{1}{2}}\right); \end{aligned} \tag{4.35}$$

with $a^{\pm}_{i+1/2jk}$, $b^{\pm}_{ij+1/2k}$, $c^{\pm}_{ijk+1/2}$ being the signal speeds in the x, y and z directions, respectively. We note the following advantages of the scheme Eq. (4.33) that we have just derived:

1. The scheme is simple and easy to implement.
2. It enjoys the usual advantages of finite-volume schemes, namely exact conservation of conservative variables and correct treatment of shocks.
3. It does not require a (computationally expensive) Riemann solver.
4. It is general and can in principle be applied to any set of conservative partial differential equations.

From the above mentioned points we conclude that the scheme is very well suited for the applications that we have in mind. The scheme has been implemented in the `CRONOS` code (Kissmann, 2006), and we will apply this code for most of our work. In the `CRONOS` code, the prescription Eq. (4.34) is evolved using either a second or third order Runge-Kutta scheme in order to obtain a solution that is second/third order accurate in time. For comparison, we will also use the `NIRVANA` code which employs a very similar numerical scheme (Ziegler, 2004).

4.1.4 Godunov Schemes

The scheme that we derived in the last section belongs to the class of Godunov schemes. The general algorithm proposed by Godunov (1959), which is also called the *REA* algorithm for "reconstruct-evolve-average" (LeVeque 2002) works as follows:

1. Use the volume-averages $\mathbf{u}_i^n$ to calculate the left and right interface states $\mathbf{u}_{i-1/2,\mathrm{r}}$ and $\mathbf{u}_{i+1/2,\mathrm{l}}$. This step may include a time advance.
2. Calculate the fluxes $\boldsymbol{\mathcal{F}}_{i+1/2}$ at the cell interfaces using an (approximate) Riemann solver.
3. Apply the flux-differencing formula Eq. (4.14),
$$\mathbf{u}_i^{n+1} = \mathbf{u}_i^n + \frac{\delta t}{\delta x}\big(\boldsymbol{\mathcal{F}}_{i+\frac{1}{2}} - \boldsymbol{\mathcal{F}}_{i+\frac{1}{2}}\big),$$
to obtain the solution at the next timestep $\mathbf{u}_i^{n+1}$.

The scheme that we derived in the last section is usually referred to as a central scheme (Kurganov et al., 2001), which, in contrast to the upwind Godunov schemes described in the REA algorithm above, does not need a Riemann solver, we can nevertheless interpret these scheme in the context of upwind Godunov schemes, since Eq. (4.32) essentially describes an approximate solution to the Riemann problem. Indeed, if we compare Eq. (4.32) equation with Eq. (10) in Miyoshi and Kusano (2005) we see that the flux defined by this equation is identical to the flux defined by the HLL Riemann solver. This means that we can easily extend the scheme implemented in the `CRONOS` code to include any desired Riemann solver by simply changing the prescription Eq. (4.32) for the calculation of the flux accordingly. A similar change has also been made to the `NIRVANA` code (see Gressel 2010).

As an example of a genuine upwind Godunov scheme, we consider the scheme implemented in the `ATHENA` code (Stone and Gardiner, 2010), which is based on the piecewise-parabolic method of Colella and Woodward (1984). The one-dimensional integration scheme follows the REA algorithm described above. Step 1 includes a time advance by $\delta t/2$ using characteristic variables. The steps 1-3 in the REA algorithm are performed only once per timestep and are not coupled to a Runge-Kutta scheme. Due to the time advance performed in step one, the code is nevertheless second order in time.

4.1.5 Evolution of the Magnetic Field

An important requirement for magnetohydrodynamical codes is that they evolve the magnetic field in manner such that the divergence free constrained $\boldsymbol{\nabla}\cdot\boldsymbol{B} = 0$ is satisfied. Otherwise the forces arising from magnetic monopoles will cause the simulation to produce unphysical results. Obviously, the algorithms discussed so far will in general not preserve the divergence of the magnetic field. A possibility to overcome this problem is to use the method of constrained transport (CT) invented by Evans & Hawley 1988. The idea behind this method is to integrate the induction equation

$$\frac{\partial \boldsymbol{B}}{\partial t} = \boldsymbol{\nabla} \times (\boldsymbol{v} \times \boldsymbol{B}) = \boldsymbol{\nabla} \times \boldsymbol{E} \tag{4.36}$$

over the cell faces resulting in a scheme that automatically preserves the value of $\boldsymbol{\nabla} \cdot \boldsymbol{B}$ in each cell. This *hybrid* ansatz (using volume averaged values of the magnetic field for the hydro part and area-averaged values for constrained transport part) is very common, and all of the four above-mentioned codes use one or the other flavour of CT for the magnetic field evolution.[5] The constrained transport scheme implemented in the `CRONOS` code is based on the works of Balsara and Spicer (1999); Londrillo and Del Zanna (2000).

4.1.6 Radiation Transport

Explicit Discretisation

The easiest method to include radiative transfer is to simply add the radiation flux $\boldsymbol{F}$ to the total energy flux. The problem with this method, where the radiation transport is treated explicitly, is that this imposes a severe restriction on the time step, since for a diffusion process the maximum possible time step scales $\propto \Delta x^2/\Delta t$. Furthermore, in optically thin regions, the diffusion coefficients can become very high, leading to prohibitively small timesteps even at low resolutions. Although the explicit treatment of the radiation transport is not really practicable for our project, we have nevertheless included it in the `CRONOS` code for use in test simulations.

Implicit Discretisation

In order to overcome the problem of the prohibitively small timestep in optically thin regions, we implemented an implicit treatment of the radiation transfer, which is used in almost all calculations presented in this thesis. We use operator splitting and calculate the radiation transport step separately from the hydro part using an implicit scheme which will be described in a moment. We start by adding the thermal energy equation

$$\frac{\partial e_{\mathrm{th}}}{\partial t} + \boldsymbol{\nabla} \cdot (e_{\mathrm{th}} \boldsymbol{v}) = -p \boldsymbol{\nabla} \cdot \boldsymbol{v} - \kappa_{\mathrm{P}} \rho (4\pi B - c E_{\mathrm{rad}}) \tag{4.37}$$

---

[5] Note that variants of CT using cell-centered fields also exist (for example Toth 2000), but these are far less common.

and the radiation energy equation

$$\frac{\partial E_{\mathrm{rad}}}{\partial t} + \boldsymbol{\nabla} \cdot (E_{\mathrm{rad}} \boldsymbol{v}) = -\frac{E_{\mathrm{rad}}}{3} \boldsymbol{\nabla} \cdot \boldsymbol{v} + \kappa_{\mathrm{P}} \rho (4\pi B - c E_{\mathrm{rad}}) - \boldsymbol{\nabla} \cdot \boldsymbol{F}, \tag{4.38}$$

in order to obtain an equation that describes the evolution of the combined (gas+radiation) energy:

$$\frac{\partial (e_{\mathrm{th}} + E_{\mathrm{rad}})}{\partial t} + \boldsymbol{\nabla} \cdot [(e_{\mathrm{th}} + E_{\mathrm{rad}}) \boldsymbol{v}] = -p_{\mathrm{tot}} \boldsymbol{\nabla} \cdot \boldsymbol{v} - \boldsymbol{\nabla} \cdot \boldsymbol{F}, \tag{4.39}$$

where $p_{\mathrm{tot}} = p + E_{\mathrm{rad}}/3 \approx p$, since in our simulations the radiation pressure is small compared to the gas pressure. Splitting off the radiation diffusion part and making use of the flux-limited diffusion approximation (Levermore and Pomraning, 1981), the radiation transport step becomes:

$$\frac{\partial (e_{\mathrm{th}} + E_{\mathrm{rad}})}{\partial t} = -\boldsymbol{\nabla} \cdot \frac{\lambda c}{\kappa \rho} \boldsymbol{\nabla} E_{\mathrm{rad}}. \tag{4.40}$$

Using the ideal gas law $e_{\mathrm{th}} = c_{\mathrm{V}} \rho T$ and assuming thermal equilibrium between matter and radiation, $E_{\mathrm{rad}} = aT^4$, we close our system of equations and end up with the following diffusion equation for the radiation energy:

$$\left(\frac{e_{\mathrm{th}}}{4E_{\mathrm{rad}}} + 1 \right) \frac{\partial E_{\mathrm{rad}}}{\partial t} = -\boldsymbol{\nabla} \cdot \frac{\lambda c}{\kappa \rho} \boldsymbol{\nabla} E_{\mathrm{rad}}. \tag{4.41}$$

From this we can estimate the timescale to reach thermal balance according to $\tau \sim H^2/D_{\mathrm{rad}}$, where H is the scale height and

$$D_{\mathrm{rad}} = \left(\frac{e_{\mathrm{th}}}{4E_{\mathrm{rad}}} + 1 \right)^{-1} \frac{\lambda c}{\kappa \rho}. \tag{4.42}$$

Note that in the radiation pressure dominated case, D_{rad} is simply given by $D_{\mathrm{rad}} = \lambda c/\kappa\rho$. However, for the gas pressure dominated case that we are considering, we actually have $D_{\mathrm{rad}} = 4E_{\mathrm{rad}}\lambda c/e_{\mathrm{th}}\kappa\rho$, which means that τ is bigger by a factor of $4E_{\mathrm{rad}}/e_{\mathrm{th}}$ and it takes thus much longer to reach thermal balance.

When working in the gas-pressure dominated regime, it is natural to replace the radiation energy E_{rad} in Eq. (4.41) by aT^4 and then solve the following diffusion equation for the temperature:

$$(c_{\mathrm{V}} \rho + 4aT^3) \frac{\partial T}{\partial t} = -\boldsymbol{\nabla} \cdot \frac{\lambda c}{\kappa \rho} 4aT^3 \boldsymbol{\nabla} T. \tag{4.43}$$

This equation is straightforwardly discretised in the following manner:

$$
\begin{aligned}
T_{ijk}^{n+1} = T_{ijk}^{n} + \frac{\Delta t}{c_V \rho_{ijk}^{n} + 4a(T_{ijk}^{n})^3} \Bigg\{ \\
\frac{1}{\Delta x^2}\left[D_{i+\frac{1}{2}jk}^{n}\Delta T_{i+\frac{1}{2}jk}^{n+1} - D_{i-\frac{1}{2}jk}^{n}\Delta T_{i-\frac{1}{2}jk}^{n+1}\right] + \\
\frac{1}{\Delta y^2}\left[D_{ij+\frac{1}{2}k}^{n}\Delta T_{ij+\frac{1}{2}k}^{n+1} - D_{ij-\frac{1}{2}k}^{n}\Delta T_{ij-\frac{1}{2}k}^{n+1}\right] + \\
\frac{1}{\Delta z^2}\left[D_{ijk+\frac{1}{2}}^{n}\Delta T_{ijk+\frac{1}{2}}^{n+1} - D_{ijk-\frac{1}{2}}^{n}\Delta T_{ijk-\frac{1}{2}}^{n+1}\right] \Bigg\},
\end{aligned}
$$

where $\Delta T_{i+\frac{1}{2}jk}^{n+1} = T_{i+1jk}^{n+1} - T_{ijk}^{n+1}$,

$$
D_{i+\frac{1}{2}jk}^{n} = \frac{1}{2}\left[\left(\frac{\lambda c}{\kappa\rho}4aT^3\right)_{i+1jk}^{n} + \left(\frac{\lambda c}{\kappa\rho}4aT^3\right)_{ijk}^{n}\right], \tag{4.44}
$$

and so on. The resulting matrix equation, which involves a diagonally dominant matrix, can in principle be solved by any standard sparse matrix solver. For the calculations reported in this work we use the method of successive overrelaxation.

4.2 Code Tests

4.2.1 Convergence Tests

As a simple test problem for our numerical code, we simulate single MRI modes. The analytical formulae for these modes have been derived in the last chapter (see Eq. (3.46)). By simulating these modes numerically, we do at the same time verify the analytical calculations that were presented there. We perform these calculations in an axisymmetric 2D (r-z) domain, where in accordance with the local instability analysis we assume that the radial domain is small enough so that geometrical curvature can be neglected. The calculations are thus performed in Cartesian coordinates with x and y corresponding to the radial and azimuthal coordinates, respectively. The computational domain has size $[-L/2, L/2] \times [-L/2, L/2]$, with $L = H$, where H is the pressure scaleheight. The vertical boundary conditions are periodic. For the radial boundary condition we choose shearing-sheet boundary conditions (Balbus & Hawley 1990b), which are identical to periodic boundary conditions except for the azimuthal velocity, where the velocity offset coming from the background shear flow is subtracted:

$$v_y(-L/2, y, z) = v_y(L/2, y, z) + \frac{3}{2}\Omega \cdot \frac{L}{2} \tag{4.45}$$

We initialise the simulations using the formulae given in Eq. (3.46). The perturbation amplitude is set to $\delta v_x = 0.001 c_\mathrm{s}$. The initial vertical magnetic field has a value corresponding to a plasma beta of $\beta = 84.33$. The simulations run for one orbit. Growth rates are measured by performing a least-squares fit to the function $\ln(\sqrt{\langle \delta v_r(t)^2 \rangle} / \sqrt{\langle \delta v_r(0)^2 \rangle})$, where the angular brackets $\langle \ \rangle$ denote a spatial average. We run simulations with ideal MHD and also simulations where radiation transport or resistivity are switched on order to test these two extensions to the ideal MHD equations also. We perform simulations both with the original central scheme (i.e. using the HLL Riemann solver) and with the modified scheme where the numerical flux in Eq. (4.32) has been replaced with the flux provided by the more sophisticated HLLD Riemann solver (Miyoshi and Kusano, 2005).

The results are shown in Fig. 4.2, where the relative difference between the theoretical growth rate as predicted by Eq. (3.41) is plotted. We find good convergence in all three cases, meaning that neither the inclusion of radiation transport (which is only first order) nor the inclusion of resistivity affect the convergence properties of the scheme for this particular test case. From panel (a) of Fig. 4.2, we see that the error is about ten times smaller when using the HLLD solver as compared to the HLL solver of the original scheme. For the case of the HLL solver, we need about as double the resolution to achieve the same accuracy. Looking at the radiative case (panel (b)), which includes an azimuthal field also and where the perturbations are no longer incompressible, we see that the performance of the HLL solver does get even much more worse, while the HLLD solver shows about the same performance as in the ideal case. In the resistive case, the convergence of both solvers is roughly similar to the ideal case. The conclusion taken from this test is that the HLLD solver performs significantly better than the HLL solver, and it does so at only a slightly higher computational cost. This strongly suggests using the HLLD solver for future calculations.

4.2.2 Code Comparison

In the last section we verified that our numerical code accurately reproduces the growth of single MRI modes, for which an analytical solution is available. This suggests that our code is indeed an appropriate tool for investigating magnetorotational turbulence, which can not be done by analytical means. The simplest setup to study 3D magnetorotational turbulence is the unstratified local shearing box (Hawley et al., 1995; Stone and Gardiner, 2010). This setup is an extension to the shearing-sheet setup that we encountered

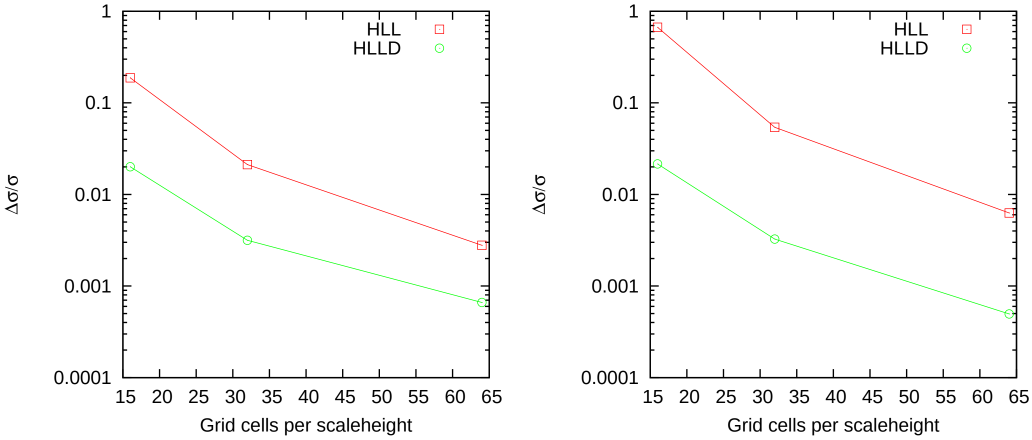

(a) *Ideal Case:* $k_r = B_y = D = \eta = 0$.

(b) *Radiative Case:* $B_y = 10B_z, D \neq 0$.

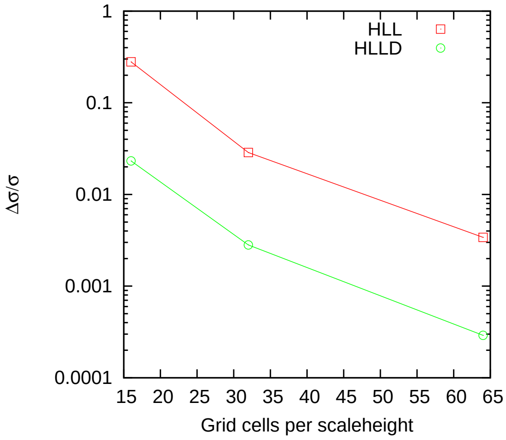

(c) *Resistive Case:* $\eta \neq 0$.

Fig. 4.2: *Single MRI Mode Convergence Test.* A single axisymmetric MRI mode with wavelength $\lambda = H$ is simulated in a domain of size $1H \times 1H$ and an initial vertical magnetic field corresponding to a plasma beta of $\beta = 84.33$. The resulting growth rate in the ideal MHD case (panel (a)) is $\sigma = 0.75$ (i.e. the maximum growth rate). Panel (b) shows the radiative case which possesses also an azimuthal magnetic field $B_y = 10B_z$. The growth rate in this case is $\sigma = 0.53$. The setup for the resistive case (panel (c)) is the same as in the ideal case, except that resistivity is switched on, with the value of η chosen such that the magnetic Reynolds number is $\mathrm{Re}_\mathrm{m} = c_\mathrm{s}H/\eta = 100$. The growth rate in this case is $\sigma = 0.52$. Plotted is the relative error between the theoretical growth rate and the growth rate measured in the simulation vs. the number of grid cells per scaleheight. The label 'HLL' refers to simulations performed with the HLL Riemann solver, while 'HLLD' refers to simulations where the HLLD Riemann solver is used.

in the last section. The simulation domain is a rectangular box, where the Cartesian coordinates (x, y, z) correspond to the radial, azimuthal and vertical directions, respectively. The boundary conditions in the azimuthal and vertical directions are periodic. The radial boundary conditions are so-called shear-periodic boundary conditions, which are consistent with the background shear flow. We set up a fiducial model which takes place in a box of size $1H \times 6H \times 1H$ and that has as its initial condition the state describe in Sec. 3.1, with $B_y = 0$ and an initial vertical magnetic field B_z corresponding to a plasma beta of $\beta = 400$. The simulation is seeded with random velocity perturbations of order $0.01c_\mathrm{s}$.

In order to look how different codes compare in simulations of magnetorotational turbulence we run the fiducial model described in the previous paragraph with all of our four codes, `ZEUS`, `NIRVANA`, `CRONOS` and `ATHENA`. We choose a resolution of $32 \times 64 \times 32$ grid cells. We find that in most of the variables, the codes actually produce rather similar results, see for example the evolution of the magnetic energy depicted in panel (a) of Fig. 4.3. The similarity in the result is likely to a large part due to the fact that we have a strong magnetic background field. As a consequence, the dynamics is dominated by the fastest growing channel mode. In a period of several orbits, the mode grows, is destroyed, and grows again (Sano and Inutsuka, 2001).[6] The periodic reappearance of the channel mode can clearly be seen in movie of, for example, the magnetic energy and also in the oscillations in panel (a) of Fig. 4.3. It is clear that once the channel mode is sufficiently resolved, the simulation is essentially converged, so the similarity of the results of the different codes is not too surprising.

A remarkable difference shows up, however, if we look at the heating rates. These can be measured directly by looking at the total thermal energy in the box, since due to the periodic boundary conditions, energy cannot escape from the box. Therefore, the turbulent dissipation leads to an approximately steady increase of the thermal energy. By looking at panel (b) of Fig. 4.3, we see that the heating rate for the `ZEUS` code is much lower than for the other codes. The reason for this is that the `ZEUS` code evolves the thermal energy, meaning that the compressional heating is the only factor that contributes to the increase in internal energy. On the contrary, the other codes involve the total energy, which means that the losses in magnetic and kinetic energy are also captured and automatically transferred into gas internal energy. However, the three other codes also show significant differences concerning the heating rates, with the `ATHENA` code producing about as twice as much heating as `NIRVANA` and `CRONOS`. This shows that at least at low resolutions the heating rate may depends on numerical effects.

---

[6] Possible mechanisms responsible for the destruction of the channel mode include parasitic modes, mode-mode interactions and magnetic reconnection.

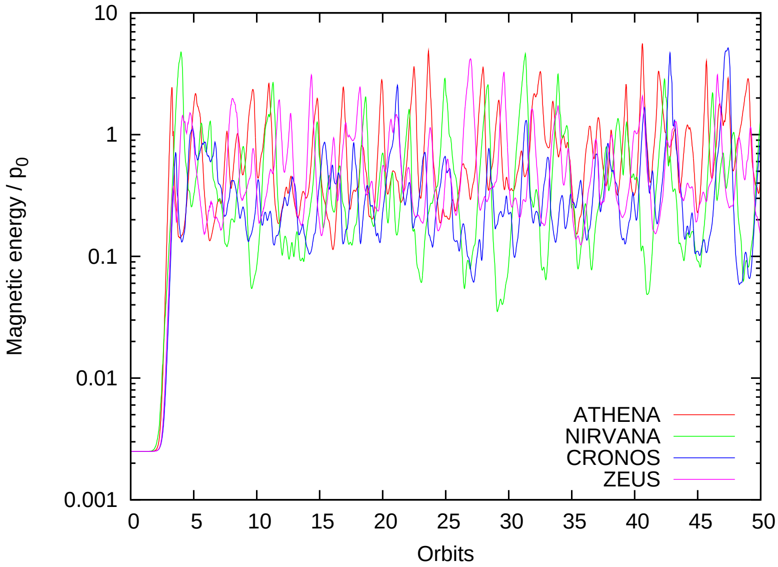

(a) Plot of the magnetic energy $E_{\rm mag} = B^2/2$ normalised to the initial gas pressure p_0.

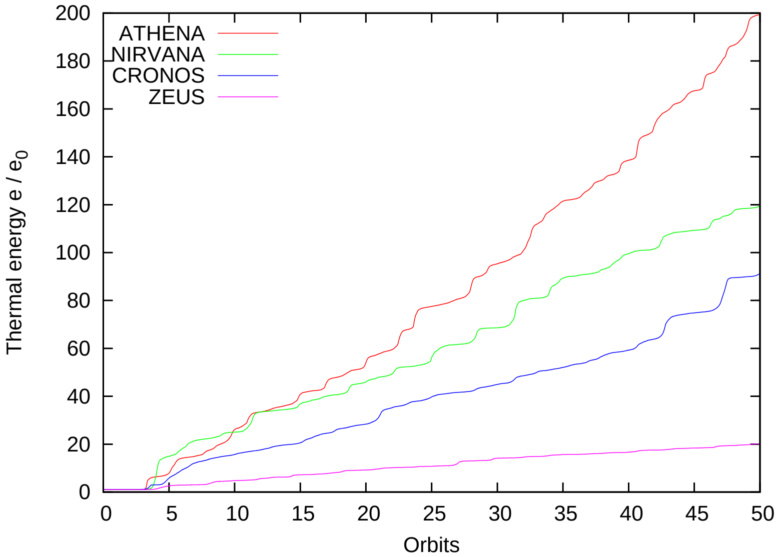

(b) Plot of the thermal energy e normalised to the initial thermal energy e_0.

Fig. 4.3: *Plot of Shearing-box results for different MHD codes.* Shown are the volume-averaged magnetic and thermal energy, obtained with the MHD codes `ZEUS`, `NIRVANA`, `CRONOS` and `ATHENA`.

Name	Solver	Resolution	$\langle\langle\alpha_{\mathrm{R}}\rangle\rangle$	$\langle\langle\alpha_{\mathrm{M}}\rangle\rangle$	$\langle\langle\alpha\rangle\rangle$
`rs16.hll`	HLL	16x32x16	no sustained turbulence		
`rs32.hll`	HLL	32x64x32	no sustained turbulence		
`rs64.hll`	HLL	64x128x64	no sustained turbulence		
`rs128.hll`	HLL	128x256x128	no sustained turbulence		
`rs16.hlld`	HLLD	16x32x16	$4.4 \cdot 10^{-5}$	$1.1 \cdot 10^{-4}$	$1.6 \cdot 10^{-4}$
`rs32.hlld`	HLLD	32x64x32	0.004	0.011	0.015
`rs64.hlld`	HLLD	64x128x64	0.006	0.018	0.024
`rs128.hlld`	HLLD	128x256x128	0.004	0.012	0.016

Tab. 4.1: Overview of the simulation runs performed for the resolution study. 'HLL'/'HLLD' means that the HLL/HLLD Riemann solver has been used for that particular run. All runs were restarted using the data from model `rs16.hlld` at $t = 100$ orbits and have been run until $t = 140$ orbits. The last three columns show the values of the Reynolds, Maxwell and total stress, averaged over 40 orbits. For further information, see the text.

4.2.3 Resolution Study

Model

In order to further test our numerical code and investigate the influence of numerical effects on the outcome of the MRI, we also run a model that has zero net magnetic flux in the vertical direction. The simulation box has a size of $1H \times 6H \times 1H$ and the simulation is initialised with a magnetic field of the form

$$\boldsymbol{B} = B_0 \sin(2\pi x/H)\, \hat{\boldsymbol{e}}_z, \tag{4.46}$$

where the strength of B_0 is chosen such that it corresponds to a plasma beta of $\beta = 100$. As has already been remarked earlier, with this type of magnetic field configuration there is no driving of the turbulence by an imposed background field; instead it depends on the working of an internal dynamo if the magnetic field can be sustained or not. We perform runs at different resolutions, using either the HLL or the HLLD Riemann solver. Tab. 4.1 gives an overview of the runs performed. We first run model `rs16.hlld` until $t = 100$ orbits. All other runs are then initialised using the data from this simulation, and are then run until $t = 140$ orbits. The time-averaged values for the turbulent stresses have been measured during this period from $t = 100 - 140$ orbits. The stresses are measured according to the following prescription:

$$\alpha = \langle T_{\mathrm{R}} + T_{\mathrm{M}} \rangle / p_0, \tag{4.47}$$

where p_0 is the initial gas pressure, $T_{\mathrm{R}} = \rho\delta v_r \delta v_\phi$ denotes the Reynolds stress and $T_{\mathrm{M}} = -\delta B_r \delta B_\phi$ is the Maxwell stress. The angular brackets $\langle\cdots\rangle$ indicate a spatial average. We also use the dimensionless stresses α_{R} and α_{M} defined as

$$\alpha_{\mathrm{R}} = \langle T_{\mathrm{R}}\rangle/p_0, \quad \alpha_{\mathrm{M}} = \langle T_{\mathrm{M}}\rangle/p_0. \tag{4.48}$$

Results

We find that when using the HLL solver no sustained dynamo action occurs. At the beginning, the magnetic field is amplified due to transients perturbations, but these always decay after a few orbits and the simulations converges towards a laminar state. This behaviour is the same for all resolutions, and the magnetic field decays even for the highest resolution simulation which uses 128 grid cells per pressure scaleheight in the radial and vertical directions. The same behaviour has also been reported recently by Balsara and Meyer (2010).

In contrast to this, the HLLD solver shows sustained magnetic field amplification even for a resolution as low as 16x32x16, however, for this low resolution, the saturation level is more than one order of magnitude smaller as for the simulation using the double resolution (see Fig. 4.4 and Table 4.1). The simulations that use 32/64 grid cells per scaleheight yield approximately the same saturation level. When increasing the resolution further, the saturation level decreases. This indicates that at high resolutions our codes shows the same behaviour as it has been reported for the `ZEUS` code (Fromang et al., 2007) and for the `ATHENA` code (Simon et al., 2009), namely a decrease of the turbulent saturation with increasing resolution. However, we would have to perform simulations at still higher resolutions to fully validate this result.

4.3 Investigating the Influence of Radiation Transport on Magnetorotational Turbulence

In Chap. 3 we have seen that radiation transport changes the growth rates of the MRI. The next question to ask is then: Does radiation transport also affect the saturation level of the magnetorotational turbulence? As has been shown in Flaig et al. (2009), the answer is yes. For this study, we switch to a shearing box with a computational domain of size $1H \times 4H \times 1H$. Apart from this, all other parameters are the same as in the model used for the code comparison described in Sec. 4.2.2. Especially this means that we employ a magnetic field with nonzero net flux in the vertical direction, so that we can control the strength of the turbulence. Due to the fact that in our simulations the magnetic field possesses a net flux, the resulting α is quite large, $\alpha \gtrsim 0.1$.

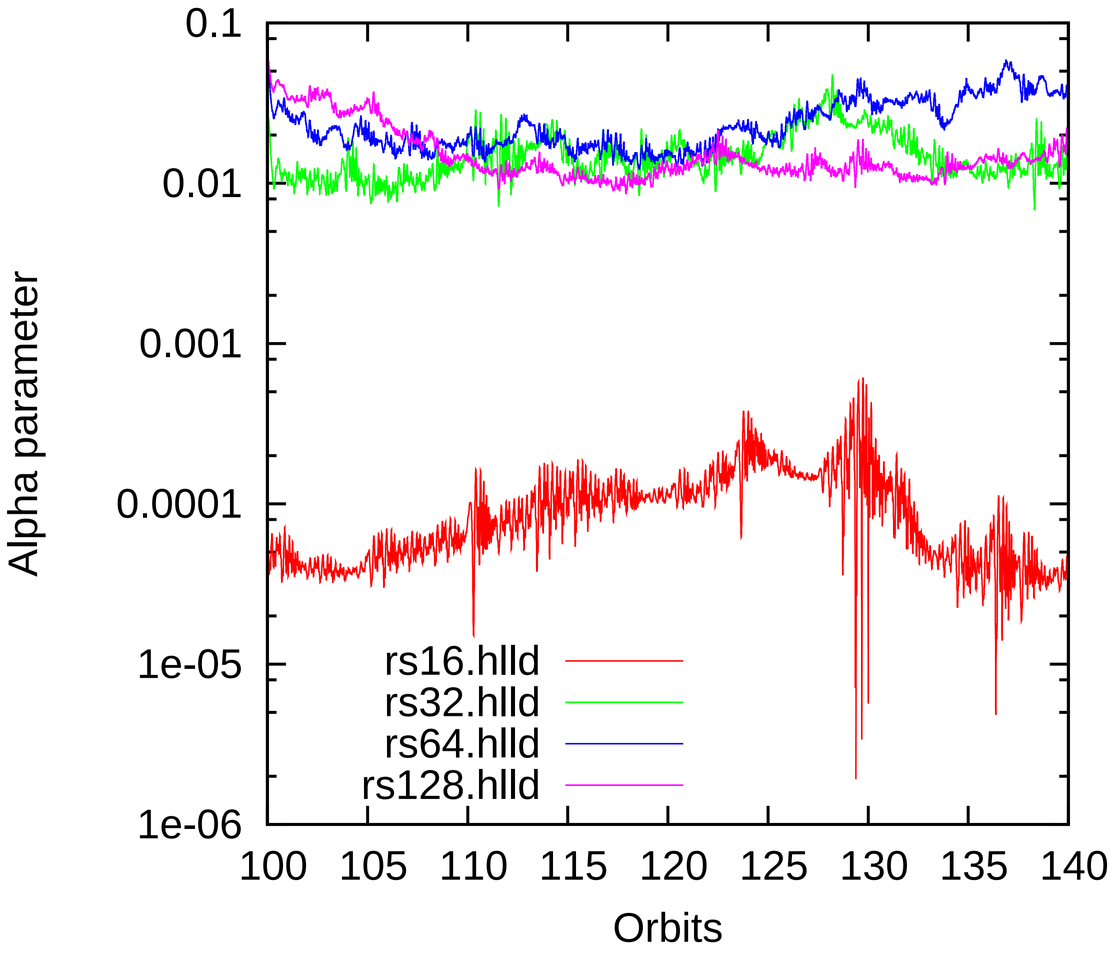

Fig. 4.4: Time evolution of the total stress, shown for the models which employ the HLLD solver. The parameters used in this simulation can be found in Table 4.1. For further information, see the text.

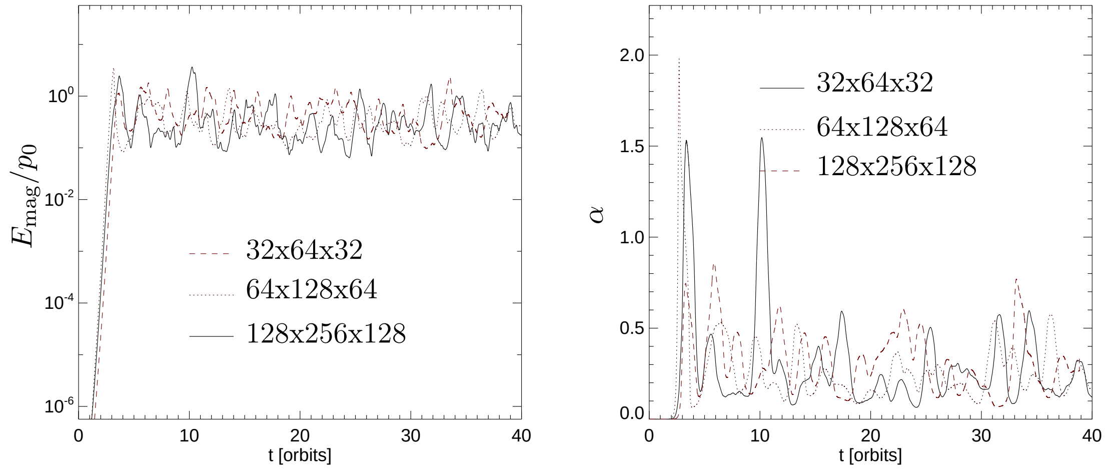

Fig. 4.5: Resolution dependence of the turbulent activity on the numerical resolution. The left and right panels show the time evolution of the perturbed magnetic energy and the alpha parameter, respectively. In case of the alpha parameter the curves have been smoothed over 1 orbit. When considering long-term averages of these quantities, there appears to be no trend with varying resolution.

Tab. 4.2: Time- and space-averaged quantities from 3D shearing box simulations performed with the `CRONOS` code. In all of the simulations $B_\phi = 0$. In the first three lines, only the resolution is varied, while the last three lines show the dependence on the strength of radiative diffusion. Averages were taken over 10 to 40 orbits.

Resolution	$D/H^2\Omega$	E_{mag}/p_0	α
32x64x32	0.001	0.400	0.278
128x256x128	0.001	0.505	0.299
64x128x64	0.001	0.337	0.226
64x128x64	0	1.007	0.719
64x128x64	10^{-8}	0.358	0.244
64x128x64	0.001	0.337	0.226

4.3.1 Saturation Level

In order to check if there exists a trend for the turbulent activity with different resolution, we performed three radiative runs using a constant radiative diffusion coefficient of $D = 0.001 H^2\Omega$, where the resolution was successively doubled. Fig. 4.5 shows the time evolution of the magnetic energy and the α-parameter for this runs. In Table 4.2 long-term averages of this quantities as well as of the Maxwell and Reynold stresses can be found. The results displayed in Fig. 4.5 and Tab. 4.2 indicate no net trend for the change of the saturation level with resolution (the first three lines in the table).

In order to investigate the influence of radiation transport on the saturation level of the MRI-induced turbulence, we perform simulations with varying radiative diffusion coefficient, where we pick a resolution of 64x128x64. The results show a *decrease* of the turbulent activity with increasing radiative diffusion coefficient D, see last 3 entries in Tab. 4.2. A qualitative explanation for this phenomenon is given below.

In order to check this results with a different numerical scheme, we also perform simulations with the `ZEUS` code. We use the same setup as in the simulations done with the `CRONOS` code, except that the strength of the constant vertical magnetic field is taken as corresponding to a plasma beta of $\beta = 800$. We perform simulations with and without azimuthal magnetic field B_ϕ, using different resolutions (see Table 4.3). In Fig. 4.6, the magnetic energy is plotted for the high resolution simulations.

The results for the turbulent saturation level differ somewhat between these two different codes. For example, if we compare the simulations in lines 3 and 4 of Tab. 4.2 with the corresponding simulations done with the `ZEUS` code, lines 5 and 6 of Tab. 4.3, the ratio of the saturation levels in the case of the `ZEUS` code turns out to be about a factor of two smaller than in the simulations done with the `CRONOS` code. We have checked that

Tab. 4.3: 3D shearing-box simulations performed with `ZEUS`. In some of the simulations, a nonzero constant B_ϕ was used, leading to a higher saturation level. Averages were taken from 10 to 40 orbits.

Resolution	$D/H^2\Omega$	B_ϕ/B_z	E_{mag}/p_0	α	T_{M}	T_{R}
32x64x32	0	0	0.398	0.248	0.210	0.038
32x64x32	0.001	0	0.245	0.146	0.123	0.023
32x64x32	0	20	2.557	1.125	0.983	0.141
32x64x32	0.001	20	1.542	0.577	0.498	0.079
64x128x64	0	0	0.552	0.335	0.288	0.047
64x128x64	0.001	0	0.392	0.218	0.187	0.031
64x128x64	0	20	2.474	1.137	1.006	0.131
64x128x64	0.001	20	2.315	1.075	0.938	0.137

this fact remains true even if we choose the same initial plasma beta as in the runs with our code. Despite these issues, all runs unambiguously show that the saturation level decreases with increasing radiative diffusion.

A plausible explanation for the phenomenon of the reduction of the saturation level due to radiative diffusion can be given as follows: As has already been noted, in the case of an initial magnetic field with nonzero net flux, the turbulence in the saturated state is still partially pumped by the channel mode. In Chap. 3 we have seen that radiative transport tends to decrease the growth rates of vertical modes by effectively increasing the compressibility of the fluid and thus making it easier for the Lorentz force to push the velocity vectors out of the r-ϕ plane. Therefore, it is to be expected that radiative transport, by decreasing the growth rate of the recurrent channel mode, acts to reduce the turbulent activity.

4.3.2 Temperature Distribution

For the full 3D simulation the influence of the radiation transport can also be visualised by the temperature distribution. This is shown in Fig. 4.7 for a similar setup as described in the previous section. Here we used an extent of the computational domain of $1H \times 6H \times 1H$ with the same spatial resolution of 64x128x64. The z-component of the magnetic induction was initialised with $\beta = 800$, and we chose $B_\phi = 20B_z$. We followed the evolution for several orbits. In Fig. 4.8 we show the distribution in the density - thermal energy plane for one simulation without and one with radiative transport. Apparently the plasma gets more isothermal when radiation transport is present – for a fully isothermal simulation the thermal energy would depend linearly on the density, thus, yielding a

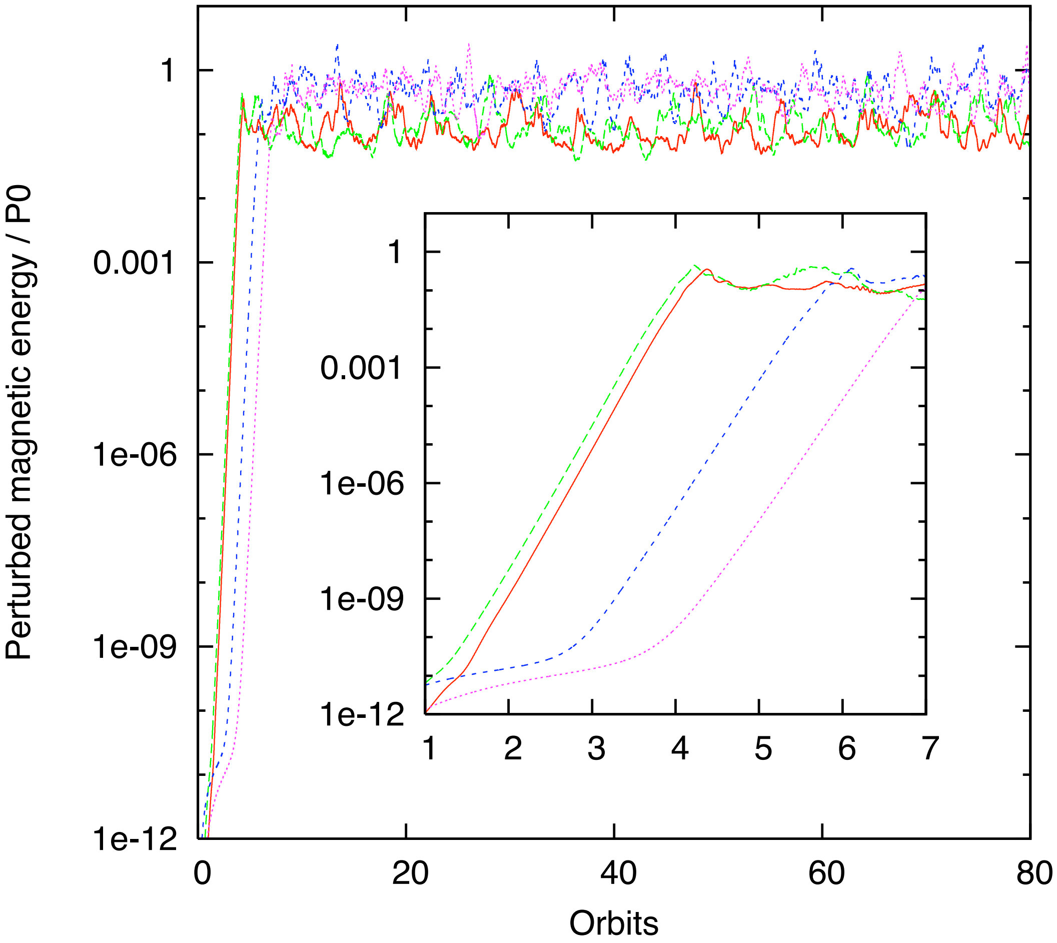

Fig. 4.6: 3D shearing box simulations performed with ZEUS at resolution 64x128x64. Shown is the perturbed magnetic energy normalised to the initial gas pressure. The solid, dashed, dot-dashed and dotted curves correspond to the combinations $B_\phi = 0/D = 0$, $B_\phi = 0/D = 0.001 H^2 \Omega$, $B_\phi = 20 B_z/D = 0$ and $B_\phi = 20 B_z/D = 0.001 H^2 \Omega$, respectively. In the linear phase, the obtained growth rates are only a few percent smaller than the growth rate of the fastest growing mode that fits in the box, which means that the initial growth is dominated by the fastest growing mode, as is to be expected.

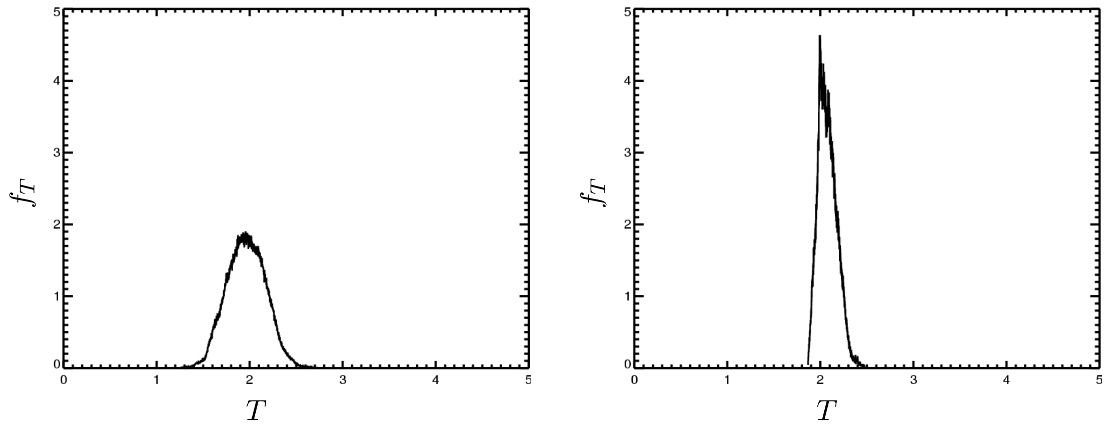

Fig. 4.7: Temperature distribution for two 3D simulations without radiation transport (left) and with radiative transport, $D = 4 \cdot 10^{-8} H^2 \Omega$ (right). In both plots, the distribution to the left corresponds to $t = 3.5$ orbits, while the right corresponds to $t = 4.1$ orbits. In the case with radiative transport, the width of the distribution function is smaller and the heating occurs less rapidly.

line in this plot. This fact also becomes apparent, when comparing the results for the temperature distribution function.

This is done in Fig. 4.7 for the same simulations. Here, the temperatures are normalised to the initial temperature (that is, initially we had a delta-peak at $T = 1$). The shift of the distribution functions with regard to the initial temperature results from the heating by (numerical) viscosity and resistivity. Obviously the distribution for the disc with radiation transport is considerably narrower. Note, however, that also for this case the temperature after several orbits differs markedly from the initial temperature. This conclusion is also strengthened by the fact that both distributions are centered at nearly the same temperature. This is due to the fact that the gas is still heated by viscosity and resistivity. In contrast to the case without radiation transport the local temperature enhancements are smoothed out by the radiation transport.

4.4 Summary

In the present chapter, we used 2D and 3D numerical simulations in order to investigate the growth of the MRI and the magnetorotational turbulence resulting from the instability. In this study, we were mainly concerned with the effects of radiation transport.

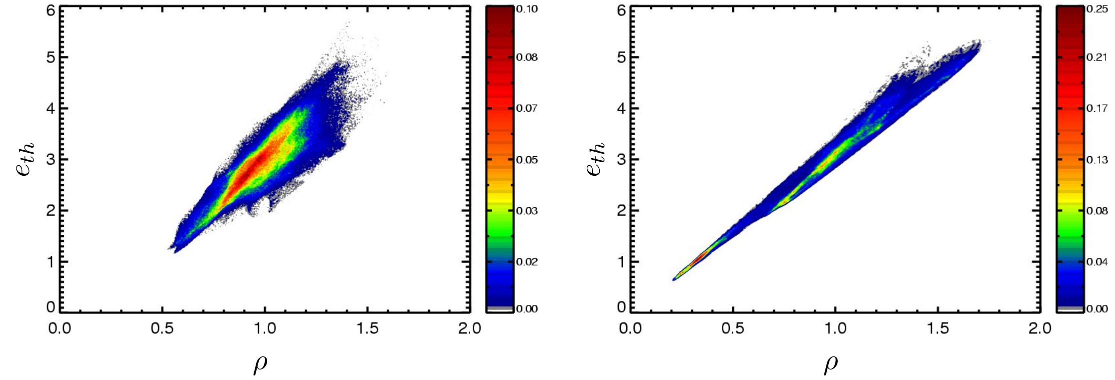

Fig. 4.8: Distribution in the density-thermal energy plane. Values are shown in normalised units. Here we show the distribution function for a simulation without radiative transport (left) and one where we used $D = 4 \cdot 10^{-8} H^2 \Omega$ (right). Both snapshots are taken at time $t = 4.1$ orbits.

- We performed a convergence study by simulating single MRI mode with resistivity and radiation transport, using the analytical formulae derived in Chap. 3. This study served to test our numerical code and also to validate the analytical calculation presented in Chap. 3.

- When comparing the HLL and HLLD Riemann solvers, we find that the HLLD solver yields a significantly higher effective resolution than the simpler HLL solver. This suggests using the HLLD solver for future calculations.

- In the simulations where resistivity or radiative diffusion was switched on, the convergence was about as good as in the ideal case. This test therefore validates our implementation of the resistivity and radiation transport parts of the code.

- In the turbulence simulations with radiative transport switched on, we find that radiative diffusion reduces the growth rates of the MRI. We can explain this interesting new result qualitatively by using the analytical results from Chap. 3.

From our tests we conclude that our numerical tool is well suited for simulations of turbulence protoplanetary discs. The next step is to include the vertical component of gravity, leading to vertically stratified simulations. The setup of this type of simulations will be the topic of the next chapter.

Chapter 5: Simulations Including Vertical Stratification

5.1 Stratified Local Shearingbox

The unstratified local shearing box setup that was the topic of the last chapter is a rather restricted model. Since it does not include the vertical component of gravity, the situation in the vertical direction is homogeneous, so nothing can be learned about the vertical structure of an accretion disc using such a simplified setup. As has been remarked earlier in Chap. 1, in the case where the net magnetic flux through the computational domain is zero, the system lacks a well-defined driving scale, and the fate of the turbulence depends critically on the working of a small-scale dynamo. Inconvenient consequences of this are the dependence of the turbulent saturation level on the Prandtl number and also on numerical effects (for example, no sustained turbulence when using the HLL Riemann solver).

Adding the vertical component of gravity is likely to alleviate such issues, since the vertical stratification does set a well-defined physical length scale, thus allowing the possibility of a large-scale dynamo. As we will see later, the turbulence that develops in the vertically stratified case is indeed qualitatively different from the unstratified one, with buoyancy effects leading to characteristic "butterfly"-cycles of the turbulence which are not present in an unstratified setup (see Sec. 6.3). For the reasons just mentioned, the physical relevance of the unstratified shearing box setup is indeed a bit questionable, and for a realistic model of magnetorotational turbulence in accretion discs, we should include the vertical stratification.

Numerical Setup

In this chapter, where we will describe the implementation and the testing of the stratified shearing box setup, we will restrict ourselves to isothermal calculations. Radiative calculations (as well as simulations including chemistry), will be reserved for the next chapter. Isothermal simulations are not only much cheaper computationally, but also less likely to cause numerical problems than radiative calculations. The isothermal models presented in this chapter will serve both as test and comparison runs for the radiative simulations. Especially, we are interested in possible differences concerning the vertical structure and the turbulent saturation level. The equations that are solved in the present chapter are given by

$$\frac{\partial \rho}{\partial t} + \boldsymbol{\nabla} \cdot (\rho \boldsymbol{v}) = 0, \tag{5.1a}$$

$$\frac{\partial (\rho \boldsymbol{v})}{\partial t} + \boldsymbol{\nabla} \cdot \left(\rho \boldsymbol{v}\boldsymbol{v} - \frac{\boldsymbol{B}\boldsymbol{B}}{4\pi} \right) = -c_{\mathrm{s}}^2 \boldsymbol{\nabla} \rho + \boldsymbol{f}, \tag{5.1b}$$

$$\frac{\partial \boldsymbol{B}}{\partial t} - \boldsymbol{\nabla} \times (\boldsymbol{v} \times \boldsymbol{B}) = 0. \tag{5.1c}$$

Going from the unstratified shearing box to the stratified one amounts to implementing the following changes to the numerical setup: First, one has to include the vertical component of gravity, which is done by adding the vertical component of the linearised gravitational force to the force term $\boldsymbol{f}$ appearing in the shearing-box equations, so that this term now becomes

$$\boldsymbol{f} = 3\rho\Omega^2 x\, \hat{\boldsymbol{x}} + 2\rho\Omega\, \boldsymbol{v} \times \hat{\boldsymbol{z}} - \rho\Omega^2 z\, \hat{\boldsymbol{z}}. \tag{5.2}$$

As a result, the density profile will no longer be uniform as in the unstratified case. Rather, as we have already seen in Chap. 1, it will resemble a Gaussian,

$$\rho \sim \exp\bigl(-z^2 c_{\mathrm{s}}^2 / 2\Omega^2\bigr), \tag{5.3}$$

Therefore, the initial conditions have also to be changed accordingly. Finally, one has to replace the periodic boundary conditions of the unstratified shearing box by more appropriate (open) boundary conditions in the vertical direction.

5.1.1 Boundary Conditions

As in the unstratified local shearing-box setup, we apply shear-periodic boundary conditions in the radial direction and periodic boundary conditions in the azimuthal direction. In the vertical direction, we will use outflow boundary conditions. Defining suitable vertical boundary conditions for stratified accretion disc simulations that are both physically meaningful and numerically stable can be a difficult task. We try the following types of boundary conditions:

Periodic Boundary Conditions

For reasons of numerical stability, many authors prefer to use periodic boundary conditions even in vertically stratified simulations [see, for example (Stone et al., 1996; Davis et al., 2010)]. Apart from lacking any physical motivation, this approach has further drawbacks. For example, in vertically stratified simulations, the magnetic field that is generated near the midplane rises to the upper layers. For the case of periodic boundary conditions the field cannot escape from the simulation domain, resulting in an unphysical pile-up of magnetic field in the upper layers of the simulation box. As a consequence, this also leads to a small timestep due to the corresponding high Alfvén speed. Apart from this considerations, the fact that periodic boundary conditions prevent radiation from escaping from the simulation domain, forbids their use in our project. However, since periodic boundary are very stable numerically, we still use them in some cases for test calculations.

Outflow Boundary Conditions

The simplest possibility to define open boundary conditions is to extrapolate all variables into the ghost zones by using zero slope extrapolation, i.e. simply copying the value of the outermost computational cell into the adjacent ghost zones. If we denote the outermost computational cell at the lower boundary by k_{min}, the outermost cell at the upper boundary by k_{max} and the number of ghost cells by n_{ghost}, then this can be mathematically expressed as

$$u_{ij,k_{\mathrm{min}}-k} = u_{ij,k_{\mathrm{min}}}, \quad u_{ij,k_{\mathrm{max}}+k} = u_{ij,k_{\mathrm{max}}}, \quad 1 \le k \le n_{\mathrm{ghost}}; \tag{5.4}$$

where u stands for any of the fluid variables. This simple approach does, however, not work for vertically stratified disc models, since these boundary conditions lead to a strong inflow of mass which quickly destroys the simulation.

This problem can be cured by modifying the boundary conditions such that *reflecting* boundary conditions are used whenever the velocity vector points into the computational domain.[1] For the lower boundary, this means that we replace the prescription Eq. (5.4) by

$$u_{ij,k_{\mathrm{min}}-k} = \left\{ \begin{array}{rl} u_{ij,k_{\mathrm{min}}+k}; & \text{if } v_z > 0 \text{ and } u \neq v_z \\ -u_{ij,k_{\mathrm{min}}+k}; & \text{if } v_z > 0 \text{ and } u = v_z \\ u_{ij,k_{\mathrm{min}}}; & \text{otherwise} \end{array} \right. , \quad 1 \le k \le n_{\mathrm{ghost}}; \tag{5.5}$$

---

[1] Note that with a Godunov-type numerical scheme, simply setting v_z to zero in this case does not guarantee that there is no inflow of mass into the computational domain.

and with an analogous expression for the upper boundary. Eq. (5.5) describes thus a very simple type of outflow boundary conditions.

Using this type of outflow boundary conditions, a stratified simulations may run stable for many orbits. However, occasionally there may still occur problems related with the magnetic field. We find that the numerical stability can be improved by using *pseudo-vacuum* boundary conditions for the magnetic field, which means extrapolating the z component and setting the other components to zero in the ghost cells. Mathematically, this is expressed as

$$u_{ij,k_{\min}-k} = \begin{cases} u_{ij,k_{\min}+k}; & \text{if } v_z > 0 \text{ and } u \notin \{v_z, \boldsymbol{B}\} \\ -u_{ij,k_{\min}+k}; & \text{if } v_z > 0 \text{ and } u = v_z \\ 0; & \text{if } u = B_x \text{ or } u = B_y \\ u_{ij,k_{\min}}; & \text{otherwise} \end{cases}, \quad 1 \le k \le n_{\text{ghost}}; \tag{5.6}$$

and with an analogous expression for the upper boundary. Although one might worry that simply setting two of the three magnetic field components to zero might distort the magnetic field structure near the vertical boundaries, we find that the influence of the boundaries on the magnetic field structure does not appear to be stronger as when using extrapolating boundary conditions for all three magnetic field components (as was done, for example, in Simon et al., 2010). See also Fig. 5.4 later in this chapter.

Transparent Boundary Conditions

We also try so-called *transparent* boundary conditions which consist of solving a characteristic equation at the boundaries which contains only outgoing waves. Such boundary conditions have been successfully used in the work of Suzuki and Inutsuka (2009). The idea behind this type of boundary condition can be explained as follows: Consider a system of conservation laws in one dimension, where $\mathbf{u}$ is the vector of conserved variables and $\mathbf{f}(\mathbf{u})$ is the flux vector, i.e. written in conservative form the system of equation reads

$$\frac{\partial \mathbf{u}}{\partial t} + \frac{\partial \mathbf{f}(\mathbf{u})}{\partial z} = 0. \tag{5.7}$$

For the case of the one dimensional MHD equations, we have $\mathbf{u} = \{\rho, \boldsymbol{v}, B_x, B_y\}$[2], where explicit formulas for the fluxes have been given in Chap. 4. By performing a transformation to primitive variables,[3] $\mathbf{u} = \mathbf{u}(\mathbf{v})$ and applying the chain rule in Eq. (5.7), we can write this system of equations as

---

[2] Note that, in one dimension, the longitudinal magnetic field component (B_z in our case) is constant.

[3] The choice of primitive variables is in principle arbitrary, for example one may simply choose $\mathbf{v} = \mathbf{u}$. In practice, one chooses a transformation such that the resulting equations become especially simple, for example in the case of MHD, the equations become simpler if we use the thermal energy or the pressure instead of the total energy.

$$\frac{\partial \mathbf{v}}{\partial t} + \mathsf{A}\frac{\partial \mathbf{v}}{\partial z} = 0, \tag{5.8}$$

where the matrix A is defined as

$$\mathsf{A} \equiv \frac{\partial \mathbf{f}(\mathbf{u}(\mathbf{v}))}{\partial \mathbf{u}}. \tag{5.9}$$

Next, we diagonalise the matrix $\mathbf{A}$ according to

$$\mathsf{A} = \mathsf{S}^{-1}\mathsf{D}\mathsf{S}, \tag{5.10}$$

where D is a diagonal matrix, and perform a transformation to *characteristic variables* defined by $\mathbf{w} \equiv \mathsf{S}\mathbf{v}$, by which we obtain our system of equations written in characteristic form:

$$\frac{\partial \mathbf{w}}{\partial t} + \mathsf{D}\frac{\partial \mathbf{w}}{\partial z} = 0. \tag{5.11}$$

When using equations of this form, the individual equations are now longer coupled, rather we have a system of independent advection equations

$$\frac{\partial w_i}{\partial t} + \lambda_i \frac{\partial w_i}{\partial z} = 0, \tag{5.12}$$

where $\lambda_i \equiv D_{ii}$ are the eigenvalues of the matrix A. In these equations, a positive value of λ_i means that information is propagating upwards, while a negative value means that information is propagating downwards.

In our simulations, we would like to have a situation where no information from outside (i.e. noise) enters the simulation domain. This can be achieved by solving a characteristic equation similar to (5.12) at the boundaries, where we discard all waves that propagate into the computational domain. For the specific case of the lower boundary, this would mean we perform the substitution $\lambda_i \to \lambda_i^- \equiv \min\{\lambda_i, 0\}$ in Eq. (5.12). The modified system of equations can be straightforwardly discretised according to

$$w_i^{n+1} = w_i^n - \frac{\lambda_i^- \Delta t}{\Delta z}(w_{i+1}^n - w_i^n); \tag{5.13}$$

and a similar formula for the upper boundary. We verify that the use of transparent boundary conditions does indeed produce much less unphysical reflections than the outflow boundary conditions Eq. (5.6). However, for the case of stratified MRI-simulations we find not much difference between simulations using transparent boundary conditions and simulations using outflow boundary conditions. Moreover, for large box sizes (larger than three pressure scaleheights) the transparent boundary conditions tend to be unstable. This problem can possibly be cured when using an implicit discretisation of Eq. (5.12), as was done by Suzuki and Inutsuka (2009). Since it is at the present stage not clear if the use of transparent boundary conditions really yields a significant advantage, we choose, however, not to investigate this further and rather adopt the outflow boundary conditions Eq. (5.6) for all the following simulations.

5.1.2 Initial Conditions

As the initial condition for the hydrodynamic variables we choose a state of approximate vertical hydrostatic equilibrium:

$$\begin{aligned} \rho(t=0) &= \rho_0 \exp(-z^2/2H_0^2), \\ \boldsymbol{v}(t=0) &= -\tfrac{3}{2}\Omega x\, \hat{\boldsymbol{y}} + \delta \boldsymbol{v}. \end{aligned} \tag{5.14}$$

The sound speed c_s is taken to be constant. We add small random velocity perturbations $\delta\boldsymbol{v}$ of order $5 \cdot 10^{-3}\, c_\mathrm{s}$ to the velocity. The initial magnetic field is derived from a vector potential,

$$B(t=0) = \boldsymbol{\nabla} \times \boldsymbol{A}(t=0), \tag{5.15}$$

in order to guarantee that the divergence-free condition $\boldsymbol{\nabla} \cdot \boldsymbol{B} = 0$ is satisfied. We perform simulations with different initial magnetic field configurations. At this point we note that due to the type of boundary conditions that we apply, the vertical magnetic flux is conserved to good accuracy throughout the simulation, however not exactly due to small interpolation errors at the shear-periodic radial boundaries.

Simulations that start from different magnetic field configurations with the same net vertical magnetic flux evolve towards the same turbulent state (Hawley et al., 1996). However, the time it takes for the disc to reach the fully turbulent state might vary significantly for different initial magnetic field configurations. Therefore, we search for a magnetic field configuration that lets the turbulence develop throughout the disc as quickly as possible.

Constant Vertical Magnetic Field

The simplest initial magnetic field configuration is that of a constant vertical magnetic field, which is described by the following vector potential:

$$\boldsymbol{A} = B_0 x\, \hat{\boldsymbol{y}}. \tag{5.16}$$

The magnetic field strength B_0 is most conveniently expressed in terms of the plasma beta $\beta = 8\pi p_0/B_0^2$. A simulation containing a net vertical flux leads to much more vigorous turbulence as compared to a zero net flux simulation. In the simulations of Suzuki & Inutsuka (2009) it has been found that a vertical magnetic field corresponding to a plasma beta as big as 10^6 is already sufficient to drive a significant disc wind, with the mass loss rate being dependent on the value of the magnetic net flux. We are able to reproduce this finding with our code. However, in the present work we will restrict ourselves to models that have zero net flux, which are in general more interesting due to the presence of self-sustained dynamo action. Another reason is that we want to investigate a possible resolution dependence of the turbulent saturation level. Such a dependence is likely to be less pronounced in net flux simulations, since the value of the magnetic flux controls the saturation level (as has already been discussed in Chap.1). Therefore, the case of zero net magnetic flux is more interesting also from the viewpoint of a resolution study.

Sinusoidal Vertical Magnetic Field

One of the simplest possibilities to construct a magnetic field with zero net flux is to use a sinusoidally varying vertical field, which is derived from the following vector potential (Hawley et al., 1996):

$$\delta \boldsymbol{A} = B_0 \frac{\sin(2\pi x/L_x)}{2\pi/L_x}\,\hat{\boldsymbol{y}}, \tag{5.17}$$

where L_x is the radial extent of the box. When performing simulations with a large vertical box size (12 or more pressure scale heights) it takes a long time for the whole disc to become turbulent, usually about 100 orbits or even more. The reason for this is that for this magnetic field configuration, the Alfvén speed scales as $v_\mathrm{A} \propto \exp(-z^2/2H_0^2)$. Since the fastest growing MRI mode fulfills $\lambda_\mathrm{max} \sim v_\mathrm{A}/\Omega$, it obeys the same scaling. Choosing B_0 in such a manner that the MRI is resolved in the upper layers of the disc, means that the midplane is initially stable, since the most unstable wavelength is much smaller there and cannot be resolved.[4] The MRI thus starts in the upper layers first and very slowly spreads towards the midplane. The midplane only becomes unstable when the magnetic field, which is pushed towards the midplane via the turbulent motions in the upper layers, has become strong enough. Since magnetic buoyancy works against this, this process can take a very long time, and we observe that in some cases simulations do not become fully turbulent even after very long integration times.

---

[4] Note that on the other hand we cannot choose B_0 to be so strong that the MRI is resolved initially at the midplane: Then the plasma beta in the upper layers would be extremely small, leading to the disruption of the disc, since the sinusoidally varying magnetic field is not an equilibrium configuration. Note also that the problem is the same in the case of the constant vertical magnetic field: Here again one can choose only a very high plasma beta, otherwise the disc will quickly loose most of its mass due to the very vigorous MRI turbulence.

Improved Initial Magnetic Field Configuration

The considerations of the previous paragraph lead us towards the following improvement: If we multiply Eq. (5.17) by a factor of $\exp(-z^2/2H_0^2)$, resulting in the vector potential

$$\delta \boldsymbol{A} = B_0 \frac{\sin(2\pi x/L_x)}{2\pi/L_x} \exp(-z^2/2H_0^2)\, \hat{\boldsymbol{y}}, \tag{5.18}$$

then the Alfvén speed (and, correspondingly, the fastest growing unstable wavelength) will both be approximately constant throughout the simulation domain, allowing the MRI to grow everywhere right from the beginning. We find that when choosing a value of $\beta = 100$, then the whole disc becomes turbulent in less than ten orbits. Therefore, the improved boundary conditions Eq. (5.18) can indeed save us a lot of integration time.

5.2 Simulation Runs

5.2.1 Overview

We set up vertically stratified, isothermal simulations using the outflow boundary conditions Eq. (6.2) and initial conditions given by Eq. (5.14) and Eq. (5.18) with a plasma beta of $\beta = 100$. We choose a box of size $L_x \times L_y \times L_z$, with $L_x = H_0$ and $L_y = 6H_0$.[5] We perform simulations with different vertical box sizes L_z and at different resolutions, and using different solvers. Tab. 5.1 provides an overview of the runs performed. Note that the simulations `rs32` and `rs64` have been restarted from the simulation `rs16` at $t = 100$ orbits.

Due to the special magnetic field configurations used, the MRI grows quickly and the whole disc is turbulent in less than ten orbits. The turbulent activity varies on a timescale of tens of orbits (see Fig. 5.1), therefore it is necessary to perform averages over at least several tens of orbits in order to calculate meaningful mean quantities.

---

[5] Note that in the isothermal case, the problem is already fully specified once values for β, L_x/H_0, L_y/H_0 and L_z/H_0 have been provided. In our code, we use a system of units such that $\Omega = \rho_0 = H_0 = 1$. The numerical value for the sound speed c_s follows then from $c_\mathrm{s} = H_0\Omega$, the magnetic field B_0 from $B_0^2 = 8\pi\rho_0 c_\mathrm{s}^2/\beta$, and the box lengths L_i from the ratios L_i/H_0.

Name	Solver	Resolution	L_z	n_z/H_0	Orbits	$\langle\langle \rho\, v_x v_y / p \rangle\rangle$	$\langle\langle -B_x B_y / p \rangle\rangle$	$\langle\langle (\rho\, v_x v_y - B_x B_y)/p \rangle\rangle$
`I6`	HLL	32x64x256	$12H_0$	21	200	0.001	0.003	0.004
`I5`	HLL	32x64x256	$10H_0$	25	80	0.003	0.011	0.014
`I7`	HLL	32x64x448	$14H_0$	32	70	0.004	0.013	0.017
`I6D`	HLL	64x128x512	$12H_0$	42	60	0.003	0.012	0.015
`rs16`	HLLD	16x32x128	$8H_0$	16	140	0.004	0.021	0.025
`rs32`	HLLD	32x64x256	$8H_0$	32	40	0.006	0.029	0.035
`rs64`	HLLD	64x128x512	$8H_0$	64	40	0.005	0.020	0.025

Tab. 5.1: Overview of the isothermal simulation runs. Runs labeled 'HLL'/'HLLD' use the HLL/HLLD Riemann solver, respectively. The box size (third column) is measured in scaleheights H_0 referring to the initial gas pressure $p = \rho c_\mathrm{s}^2$ at the midplane. Since the pressure (or the density) at the midplane does not change very much, this corresponds very well to the actual pressure scaleheight during the simulation. The fourth column gives the number of grid cells n_z per scale height in the vertical direction. The fifth column tells the number of orbits for which the simulation has been run. The last three columns contain the time-averaged values of the turbulent stresses as well as the standard deviation (the latter has been omitted for runs using the HLLD solver). The runs `rs32` and `rs64` have been restarted from simulation `rs16` at $t = 100$ orbits. For the runs using the HLL solver, averages have been performed from 10 orbits until the end of the simulation, while for the runs using the HLLD solver they have been performed from 100 orbits until the end of the simulation.

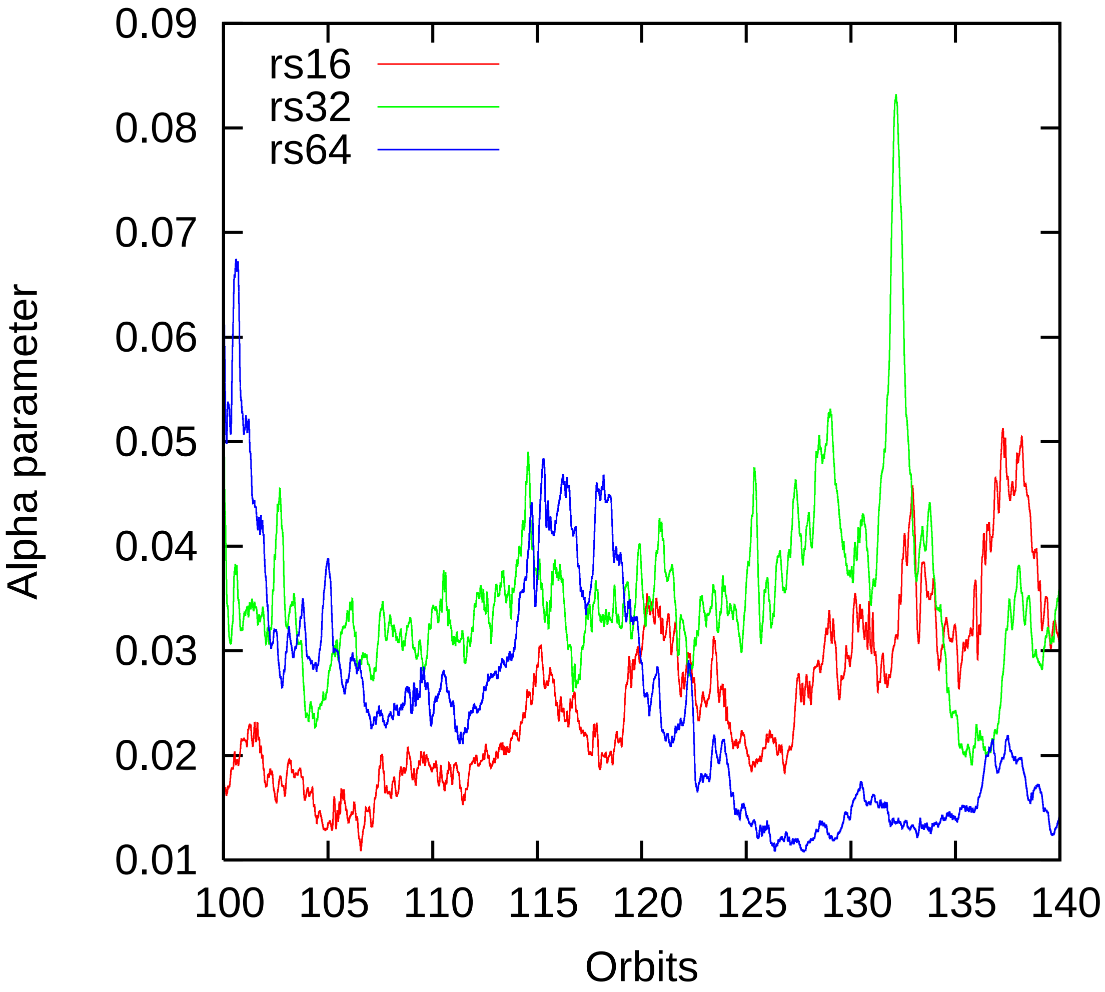

Fig. 5.1: Time history of the total turbulent stress for the models that use the HLLD Riemann solver. The simulations `rs32` and `rs64` have been restarted from the model `rs16` at $t = 100$ orbits, at twice and four times the resolution of model `rs16`, respectively.

5.2.2 Turbulent Saturation Level

We first consider the models using the HLL Riemann solver. It has been found that for stratified models of magnetorotational turbulence, the resolution in the vertical direction is critical for achieving convergence (Shi et al., 2010). The number of grid cells per scaleheight in the vertical direction is listed in the fifth column of Table 5.1. Model `I6` which has a resolution in the vertical direction of only 21 grid cells per scale height yields a significant lower saturation level than the other models, so this model is clearly under resolved. The better resolved models `I5, I7` and `I6D` yield very similar saturation levels of $\langle\alpha\rangle \approx 0.015$ with deviations of only $\sim 10\%$. This suggests that, when using the HLL solver, for isothermal simulations, a value of $\gtrsim 25$ grid cells per scale height in the vertical direction is sufficient to yield results that are reasonably converged.

Next we look at the models employing the HLLD solver. Here we choose a smaller box covering only four pressure scaleheights. We start at a resolution of 16x32x128 grid cells which is then doubled two times. All three simulations yield quite similar values for the total stress, with differences not bigger than 20%. This shows that when using the HLLD solver, already a simulation with a resolution as small as 16 grid cells per pressure scale height produces reasonable results. Taken together, our simulations support the conclusion that vertically stratified models do not suffer from the problem of diminishing turbulent activity with increasing resolution, but rather converge towards a specific value for the saturation level.

The saturation levels in the runs with the HLLD solver yield higher stresses than those using the HLL solver. This suggests that, as is the case in the unstratified case (Balsara and Meyer, 2010), the turbulent saturation level in the stratified case also does depend to some degree on the numerical scheme involved. (In addition, the smaller box size that was used in the runs using the HLLD solver, might also play a role).

5.2.3 Vertical Structure

Next we look at the vertical structure. Fig. 5.2, where gas and magnetic pressure are plotted, reveals that the vertical structure consists of two different layers: A gas-pressure dominated midplane region that extends up to 3-4 pressure scaleheights above the midplane, and a corona where the vertical support is mainly due to magnetic forces. The same two-layered structure is also reflected in the vertical profiles of the turbulent stresses, which are plotted in Fig. 5.3: In the region near the midplane, the stresses are approximately uniform, while in the corona they decline steeply and quickly become negligible.

In Fig. 5.4, we plot the magnetic field configuration found in model `rs32`. Near the midplane, the field is highly tangled. When going further away from the equator, we

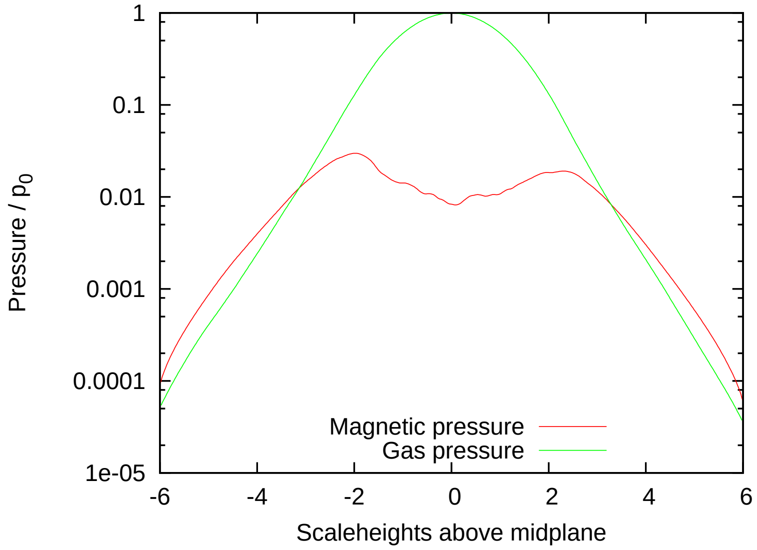

Fig. 5.2: Plot of gas pressure and magnetic pressure for model `I6D`.

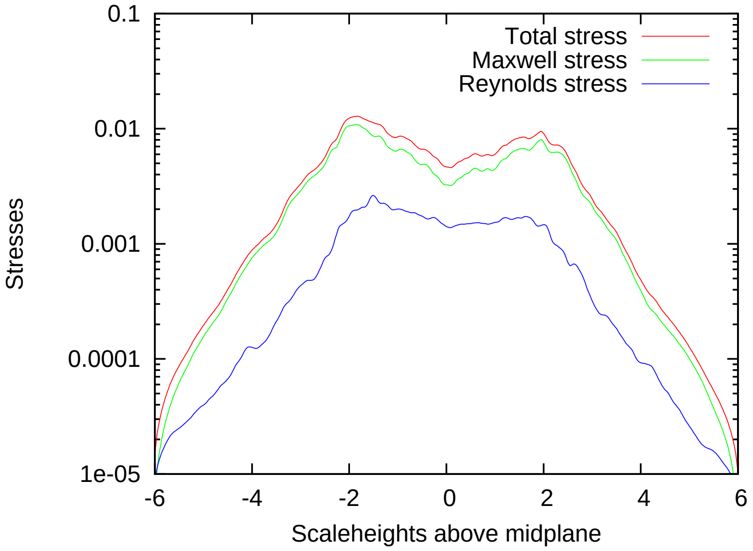

Fig. 5.3: Plots of the vertical stress profiles found in model `I6D`.

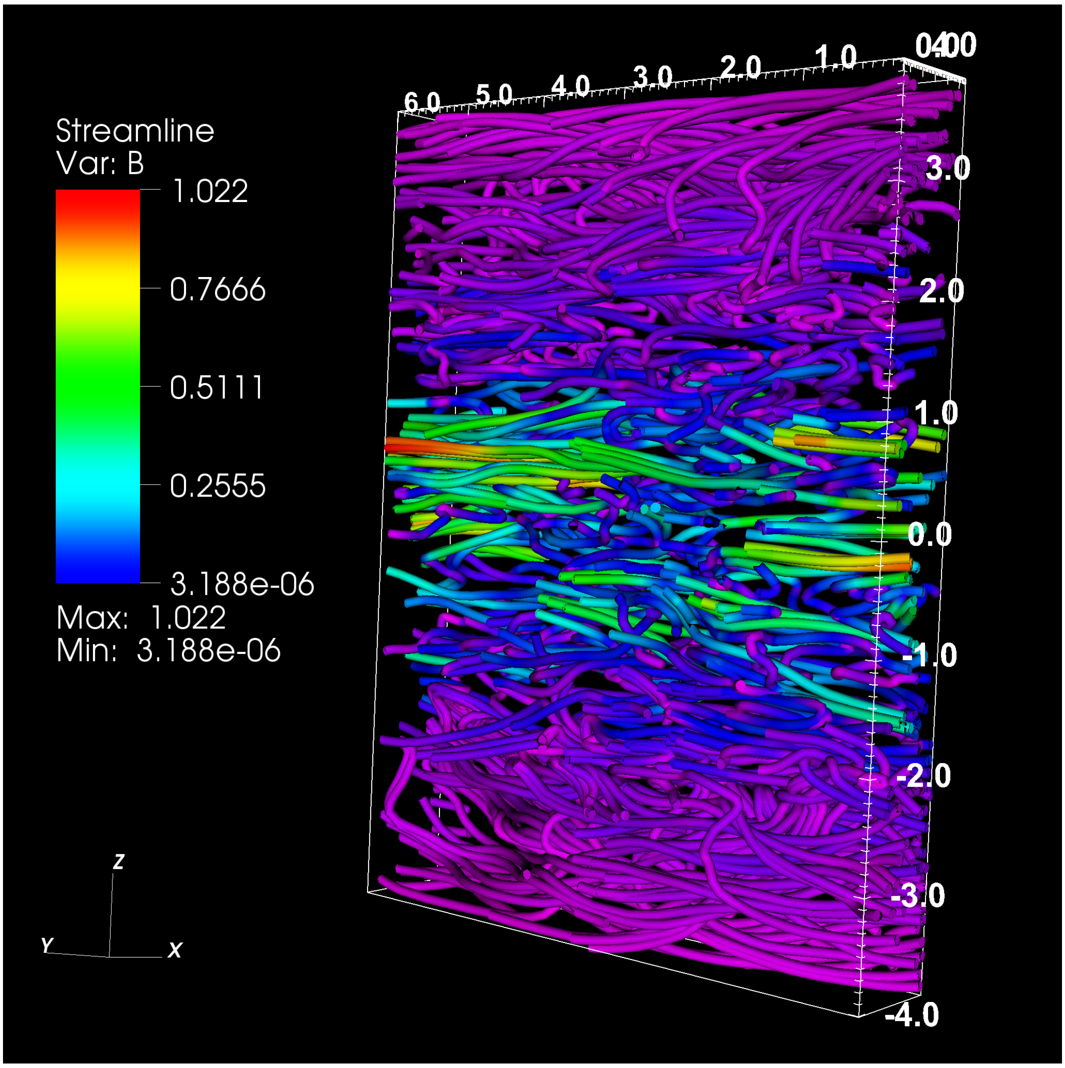
Streamline
Var: B
1.022
0.7666
0.5111
0.2555
3.188e-06
Max: 1.022
Min: 3.188e-06
Z
Y
X
6.0
5.0
4.0
3.0
2.0
1.0
0.0
0.00
3.0
2.0
1.0
0.0
-1.0
-2.0
-3.0
-4.0

Fig. 5.4: Magnetic field configuration in model `rs32` taken from a snapshot at $t = 5$ orbits. Color-coded is the magnetic field strength (in arbitrary units), while the field line density is arbitrary.

reach a region where the disc gas is stable to the MRI and the field is predominantly azimuthal. In simulation of larger boxes (Chap. 6), on finds that even further away from the midplane, the field becomes distorted again, which may be partially due to imperfections in the vertical boundary conditions (see also Simon et al., 2010). The vertical structure of a protoplanetary disc will be investigated in more detail in the context of the fully radiative models, which are the topic of the next chapter.

5.3 Summary

We have set up and tested vertically stratified models of turbulent accretion discs using an isothermal equation of state. Important ingredients to our setup are the outflow boundary conditions applied in the vertical direction and also the initial magnetic field configuration, which ensures a fast growth of the MRI throughout the whole disc. Concerning the results, we want to stress the following two points:

- Vertically stratified models do not suffer from the problem of diminishing turbulent activity when the resolution is increased, rather they show convergence once a sufficient resolution has been achieved. Our results suggest that a resolution of ~ 20 (~ 30) grid cells per pressure scaleheight is needed when using the HLLD (HLL) Riemann solver in order to achieve meaningful results.

- The vertical structure of the disc consists of a gas-pressure dominated midplane region inside the first three pressure scaleheights and a magnetically dominated corona above this region. In the corona, the MRI is quenched due to the high magnetic fields and angular momentum transport is negligible.

Due to the fact that protoplanetary disc are mostly optically thick, isothermal calculations like the ones that were described in the present chapter, are actually not a very realistic model for these systems. Rather, we have to include radiation transport. In the next chapter, where we will describe realistic radiative simulations, we will investigate the vertical structure in more detail.

Chapter 6: Radiative Models of Protoplanetary Discs

In this chapter, we move towards simulations of realistic protoplanetary disc models, which include all the relevant physical factors. We will stick to the local approximation, since due to the limited computing power, at the present time it is very difficult to include additional physics like radiation transport or non-ideal MHD effects like Ohmic diffusion into a global disc model. Indeed, all global MRI-turbulent disc models published so far employ an isothermal equation of state (for example Fromang and Nelson, 2009; Flock et al., 2010; Dzyurkevich et al., 2010). Such an ansatz is, however, not really appropriate for protoplanetary discs, since these are for a large part optically thick. For a realistic model, we have to include radiation transport.

Including radiation transport is very important in order to properly model the transport of radiation energy from the disc midplane, which is heated by turbulent dissipation, to the upper layers, where the radiation escapes into space. Without a proper treatment of radiation transport, we will not get the correct vertical structure, which will be determined by a dynamic balance between turbulent heating and radiative cooling. Including radiation transport is also an important step towards the goal of comparing numerical simulations to actual observations by modelling accretion disc spectra, and thereby deriving constraints on physical parameters (Blaes et al., 2006).

While such an attempt to include radiation transport in MRI-turbulent protoplanetary disc simulations has not been reported so far, there exist already a few works which include radiative transfer in simulations of accretion discs around compact objects (for example Turner, 2004; Krolik et al., 2007, for the case of radiation dominated discs). The gas-pressure dominated simulation of Hirose et al. (2006), is most closely related to our work, and will be the main source of reference.

When dealing with protoplanetary discs one has to consider that these are not only dense, but also cold, which means that for some part they will be only poorly ionised, leading to the formation of a “dead zone”, as has already been discussed in Chap. 2. The effects of a finite resistivity have already been studied in isothermal models (for example Sano et al., 2000; Turner and Sano, 2008; Dzyurkevich et al., 2010). The need to include non-ideal MHD effects can be circumvented by simulating a part of the protoplanetary disc that is located near to the star ($R \lesssim 1$ AU), and that is sufficiently massive, so that the disc is hot enough for collisional ionisation to be effective. The first such radiative turbulent protoplanetary disc model has been simulated by Flaig et al. (2010) and will be the main topic of this chapter. In addition, will also present simulations of a part of a protoplanetary disc which is located further away from the star, and where the effect of Ohmic resistivity is included.

6.1 Numerical Setup

We summarise the equations that will be used in this chapter: We calculate the dynamics of the disc gas by solving the equations of radiation magnetohydrodynamics in conservative form. We make the one-temperature approximation (i.e. we assume thermal equilibrium between matter and radiation), which means that we need not to solve an additional equation for the radiation energy. Radiative diffusion is treated within the flux-limited diffusion approach. Including the source terms that arise in shearing box framework, the resulting set of equations looks as follows:

$$\frac{\partial \rho}{\partial t} + \boldsymbol{\nabla} \cdot (\rho \boldsymbol{v}) = 0, \tag{6.1a}$$

$$\frac{\partial (\rho \boldsymbol{v})}{\partial t} + \boldsymbol{\nabla} \cdot \left(\rho \boldsymbol{v} \boldsymbol{v} - \frac{\boldsymbol{B}\boldsymbol{B}}{4\pi} \right) = -\boldsymbol{\nabla} p + \boldsymbol{f}, \tag{6.1b}$$

$$\frac{\partial \boldsymbol{B}}{\partial t} = \boldsymbol{\nabla} \times (\boldsymbol{v} \times \boldsymbol{B} - \eta \boldsymbol{\nabla} \times \boldsymbol{B}), \tag{6.1c}$$

$$\frac{\partial E_{\mathrm{tot}}}{\partial t} + \boldsymbol{\nabla} \cdot \left[\left(E_{\mathrm{tot}} + p + \frac{B^2}{8\pi} \right) \boldsymbol{v} - \frac{\boldsymbol{B}(\boldsymbol{B} \cdot \boldsymbol{v})}{4\pi} + \frac{\eta}{4\pi} (\boldsymbol{\nabla} \times \boldsymbol{B}) \times \boldsymbol{B}) \right] = \boldsymbol{f} \cdot \boldsymbol{v} - \boldsymbol{\nabla} \cdot \boldsymbol{F}; \tag{6.1d}$$

where $\boldsymbol{f}$ denotes the sum of the gravitational forces and the inertial forces arising in the shearing-box system [see Eq. (5.2)], $E_{\mathrm{tot}} = p/(\gamma - 1) + \rho v^2/2 + B^2/8\pi + E$ is the total energy, $\boldsymbol{F} = -(\lambda c / \kappa \rho) \boldsymbol{\nabla} E$ is the radiative energy flux, and the other symbols have their usual meaning. For most of the simulations presented in this chapter, the Ohmic resistivity is set to zero, $\eta = 0$. Note that by solving the total energy equation, rather than the thermal energy equation, all dissipative losses are automatically captured and transformed into gas internal energy. In this way the heating of the gas is consistent with the dissipation caused by the turbulence.

6.1.1 Boundary Conditions

We now turn to the boundary conditions in the vertical direction. For the fluid variables other than the temperature, we employ outflow boundary conditions similar to that used for the stratified simulations which were the topic of the last chapter. We have, however still to think about what type of boundary conditions to use for the temperature. Simply using zero-slope extrapolation for the temperature also, would not make any sense, since this would imply a radiation flux of zero at the boundary. In principle it is possible to set the temperature at the vertical boundaries in such a way that the radiation flux is approximately constant through the vertical boundaries (see Hirose et al., 2006, for the corresponding formulas). We have tested this type of boundary conditions, but we encountered problems with numerical stability. We therefore decided to use the simpler approach, of setting the temperature in the ghost cells to a value T_b much smaller than the temperature at the photosphere. As long as we are optically thin, then, by virtue of the flux limiter, the radiation flux will indeed be approximately constant through the boundary.[1] Including the boundary conditions for the temperature, our outflow boundary conditions become:

$$u_{ij,k_\mathrm{min}-k} = \begin{cases} u_{ij,k_\mathrm{min}+k}; & \text{if } v_z > 0 \text{ and } u \notin \{v_z, \boldsymbol{B}, e\} \\ -u_{ij,k_\mathrm{min}+k}; & \text{if } v_z > 0 \text{ and } u = v_z \\ 0; & \text{if } u = B_x \text{ or } u = B_y \\ T_\mathrm{b}; & \text{if } u = T \\ u_{ij,k_\mathrm{min}}; & \text{otherwise} \end{cases} , \quad 1 \le k \le n_\mathrm{ghost}. \tag{6.2}$$

An analogous expression holds for the upper boundary. The boundary conditions Eq. (6.2) match the requirements of being physically sensible and numerically stable, and we will use them for all simulations presented in this chapter. For the temperature at the boundary, we use the value $T_\mathrm{b} = 10\,\mathrm{K}$. By performing simulations with different values of T_b we verify that the results do not depend on the specific choice of T_b.

6.2 The Physical Model

As has been already mentioned, protoplanetary discs are likely for some part not well ionised, so that in principle one also has to include non-ideal MHD effects. In order to avoid this additional difficulty, we first start by modeling the region close to the star, where the gas is hot enough for collisional ionisation to be effective. Also, we choose a high surface density, corresponding to a protoplanetary disc in the earlier stages of its evolution. We call this model, where non-ideal MHD effects are neglected, the "hot" model. Later we also formulate a model corresponding to a cooler region further away from the central star, where, in addition to radiation transport, we also include Ohmic resistivity. The value of the resistivity is calculated by solving a chemical network. This latter model is called the "cool" model. We now start with the description of the "hot" model.

---

[1] Using this type of boundary conditions means, however, that we have to make our simulation box large enough so that the photosphere is well inside the computational domain. Also we have to check that the condition of a constant radiation flux through the vertical boundaries is actually fulfilled during the simulation.

6.2.1 Basic Parameters of the "Hot" Model

We simulate a model of a protoplanetary disc around a young solar-type star. We take the mass of the star to be equal to one solar mass, $M_\star = M_\odot$. The simulation box is placed at a distance of 1 AU from the central star. The disc gas is assumed to have solar chemical composition, which leads us to choose values of $\gamma = 1.4$ for the adiabatic index and $\mu = 2.35$ for the mean molecular weight. We choose a surface density $\Sigma_0 = 11\,356\ \mathrm{g\,cm^{-2}}$, corresponding to a number density at the midplane of $n_0 = 10^{15}\,\mathrm{cm^{-3}}$. This value is significantly higher than the value of $\Sigma_0 = 1700\ \mathrm{g\,cm^{-2}}$ used in the standard "minimum mass solar nebula" model (see, e.g. Weidenschilling, 1977, and also Fig. 6.1). However, the values discussed for the solar nebula may even be much higher; for example, the more recently proposed solar nebula model by Desch (2007) yields a value of $\Sigma_0 = 50\,500\ \mathrm{g\,cm^{-2}}$ at 1 AU. With the above choice of surface density, the temperatures that come out of our model are of the order of $\sim$ 1000 K in the body of the disc, so the assumption of ideal MHD is indeed justified (see, for example, Armitage, 2010).

We choose a radial box size of $L_x = 0.08\,\mathrm{AU}$. This size corresponds roughly to one pressure scaleheight (according to the typical temperatures at the midplane, that come out of our models, see Sec. 6.3.2). The azimuthal box size is $L_y = 6L_x$, and the vertical box size varies from $L_z =$ 12-16 L_x for the different simulations. For reference, the basic physical parameters are summarised in Table 6.1.

6.2.2 Stellar Irradiation

At visible wavelengths, the stellar irradiation will only be important in the very upper layers of a protoplanetary disc, where according to passively heated models, a temperature inversion will occur (Chiang and Goldreich, 1997). In the present work we are mainly interested in the temperature profile of an "actively" heated disc, which results from a balance between heating by turbulent dissipation and cooling by radiation transport. Therefore, we neglect the "passive" heating due to the stellar irradiation.

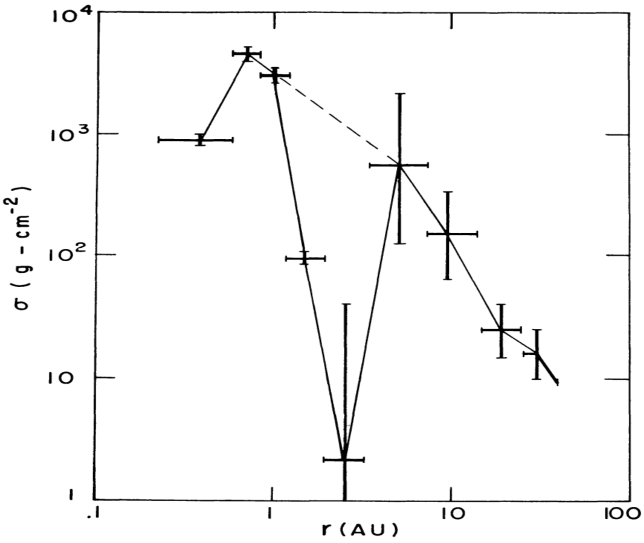

Fig. 6.1: Distribution of mass in the solar nebula according to Weidenschilling (1977). The surface densities are obtained by restoring the mass of the planets in the solar system to solar chemical composition and spreading the resulting masses in zones around their current orbits. The surface density at 1 AU is $\Sigma_0 \sim 3200$ g cm^{-2} originally, and becomes $\Sigma_0 \sim 1700$ g cm^{-2} after fitting the whole distribution with a power law.

Parameter	Symbol	Value
Radial box size	L_x	0.08 AU
Azimuthal box size	L_y	0.48 AU
Vertical box size	L_z	0.96 AU - 1.28 AU
Mass of central star	M_*	$1\,M_\odot$
Distance to central star	R_0	1 AU
Surface density	Σ_0	11 356 g cm^{-2}
Adiabatic index	γ	1.4
Mean molecular weight	μ	2.35

Tab. 6.1: Summary of basic physical parameters for the "hot" model. The vertical box size of $L_z = 0.96$ AU corresponds to a model which covers 12 pressure scale heights in the vertical direction, while $L_z = 1.28$ AU corresponds to a model with 16 scale heights.

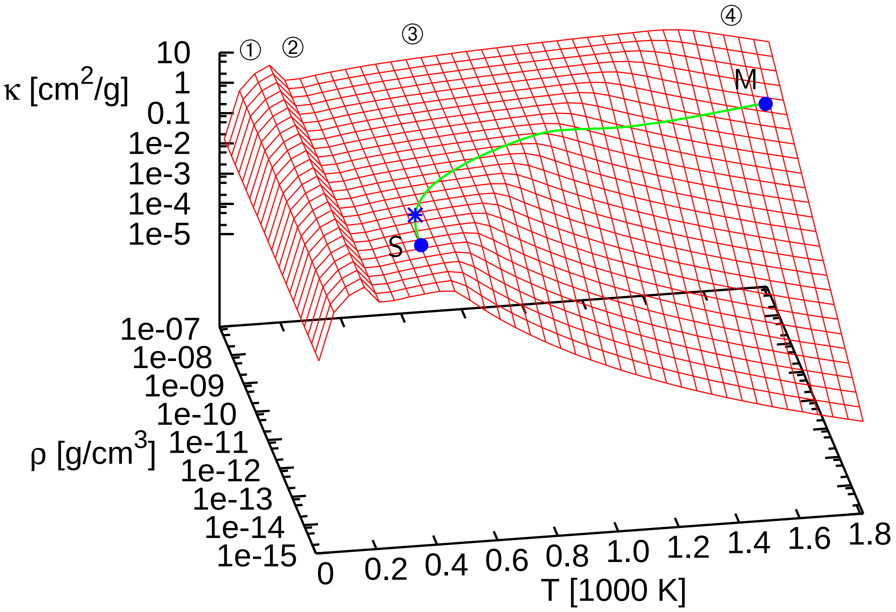

Fig. 6.2: Opacity as a function of temperature and density. The thick curve gives the opacities for the typical densities and temperatures found in our model `R7` (see Tab. 6.2), where M and S correspond to the location of the midplane and the surface, respectively, while the star $\star$ denotes the mean location of the photosphere. For an explanation of the different opacity regions ① to ④ see the text.

6.2.3 Opacity

As has already been explained in Chap. 1, in protoplanetary discs, the opacity of the disc is dominated by dust grains. For our simulations, we use dust opacities $\kappa = \kappa(\rho, T)$ as described in Bell and Lin (1994), which are calculated as a function of the gas density and temperature. Fig. 6.2 shows a plot of the opacity function for the typical density and temperature range that we have in our simulations. Four different regions can be distinguished: At the lowest temperatures, in region ①, the dominant contribution to the opacity is due to ice grains. Since these are more efficient scatterers and absorbers at shorter wavelengths, the opacity increases with temperature. In region ②, ranging from ~ 170 to $\sim 200\,\mathrm{K}$, the ice grains melt, so the opacity decreases. Region ③ is dominated by dust grains and the opacity shows only a weak temperature dependence of the form $\kappa \propto T^{0.5}$. Finally, in region ④, the temperatures and densities are sufficiently high for the dust grains to start melting, leading again to a decrease of the opacity.

6.2.4 Turbulent Dissipation

As has already been pointed out, one of our major goals is to calculate the thermal structure of an actively heated protoplanetary disc as it results from the dynamical balance between turbulent heating and radiative cooling. In a real disc, the heating occurs on the molecular scale, which can, of course, not be resolved in a numerical simulation. Instead, in a simulation, the dissipation takes place on the grid scale where energy is lost due to numerical errors.

Since we use a conservative scheme, the heating of the disc gas in our simulations is automatically consistent with the losses of kinetic and magnetic energy due to the numerical dissipation. The fact that the heating is mainly due to numerical effects[2] means that there will inevitably be some dependence on numerical parameters such as the resolution and the details of the numerical scheme involved. This issue has already been investigated in Sec. 4.2.2, where, at the low resolutions considered, we found significant differences between different numerical schemes concerning the turbulent heating. However, since numerical errors are largest at locations where there are sharp gradients in velocity and magnetic field, the numerical dissipation will at least qualitatively resemble the actual physical dissipation (Hirose et al., 2006; Krolik et al., 2007; Flaig et al., 2010). For high enough resolutions, where enough details of the turbulent flow are resolved, we expect the results to become independent from the numerical effects taking place at the grid scale. It is therefore important to perform runs at different resolutions in order to check if the results are actually converged. Unfortunately, we can not afford to carry out a study comparing different schemes, since due to the very high computational demands of the stratified radiative simulations, we can only carry out very few runs.

6.2.5 Initial Conditions

As the initial conditions for our simulations, we choose the state of approximate hydrostatic equilibrium defined by Eqs. (5.14) and (5.18). We set the initial temperature to a spatially constant value

$$T_0 = 1500 \text{ K} \tag{6.3}$$

for all runs of the "hot" model, which corresponds roughly to the temperature that is found in the saturated turbulent state. During the first ten orbits (which is the time it takes for the disc to become fully turbulent), the boundary temperature in the vertical direction is linearly lowered from the initial value T_0 down to the final value of $T_\mathrm{b} = 10$ K. This greatly improves the numerical stability, because when setting the boundary temperature initially to the small value T_b, sharp temperature gradients develop that may cause the code to crash.

---

[2] Apart from the compressive heating due to the $p\boldsymbol{\nabla} \cdot \boldsymbol{v}$-term in the energy equation.

As has already been stated, the special magnetic field initial conditions Eq. (5.18) let the disc become fully turbulent in just a few orbits. For our radiative simulations, this is very important. When using initial conditions like that defined in Eqs. (5.16) or (5.17), due to our large box sizes, it takes many tens of orbits for the disc to become fully turbulent. During this time, the disc cools and contracts, which often causes numerical problems due to very low densities in the upper layers. Thanks to the specially designed initial conditions for the magnetic field, this problem is avoided.

6.2.6 Test Problem: Equilibrium Temperature Profile

Before describing the 3D radiative simulations of magnetorotational turbulence, we first consider an additional test problem for the radiation transport. The problem that we pose consists of calculating the temperature profile of a non-turbulent disc with no internal heating in hydrostatic equilibrium. This problem will also serve as a further test for our radiation transport solver. We take the density to be given by the fixed Gaussian density profile

$$\rho(z) = \rho_0 \exp(z^2/2H_0^2) \tag{6.4}$$

and set the velocities and magnetic field to zero, $\boldsymbol{v} = \boldsymbol{B} = 0$. Only the temperature is evolved, where we use fixed temperatures at the disc midplane, $T(z=0) = T_0$ and at the disc's upper boundary $T(z = z_b) \equiv T_\mathrm{b}$. The temperature profile resulting from this configuration follows from solving the equation

$$\boldsymbol{\nabla} \cdot \frac{c\lambda}{\kappa\rho} \boldsymbol{\nabla} E = \frac{\mathrm{d}}{\mathrm{d}z} \frac{ac\lambda}{\kappa\rho} \frac{\mathrm{d}T^4}{\mathrm{d}z} = 0. \tag{6.5}$$

Using the defintion of the optical depth τ,

$$\tau \equiv \int_{z_\mathrm{b}}^{z} \kappa\rho \, \mathrm{d}z, \tag{6.6}$$

which means that $\mathrm{d}\tau = \kappa\rho\,\mathrm{d}z$, and integrating, we obtain the relation

$$T^4 = C\tau + D. \tag{6.7}$$

Evaluating this equation at $\tau = 0$ (corresponding to $z = z_\mathrm{b}$) and at $\tau = 1$, the meaning of the integration constants C and D turns out to be as follows:

$$D = T^4(z = z_\mathrm{b}) = T_\mathrm{b}^4, \tag{6.8}$$

$$C = T^4(\tau = 1) - T_\mathrm{b}^4. \tag{6.9}$$

Making use of $T_\mathrm{b} \ll T_\mathrm{phot}$, we get

$$T^4 \approx T_\mathrm{phot}^4 \tau, \tag{6.10}$$

where $T_\mathrm{phot} \equiv T(\tau = 1)$. The temperature increases thus linearly with the optical depth (see also Hubeny, 1990). Setting $z = 0$ in the above equation, we obtain the following equation between the temperature at the photosphere T_phot, the temperature in the center $T_\mathrm{c} \equiv T(z = 0)$ and the optical depth at the center $\tau_\mathrm{c} \equiv \tau(z = 0)$:

$$\frac{T_\mathrm{c}}{T_\mathrm{phot}} = \tau_\mathrm{c}^{1/4}. \tag{6.11}$$

The relations Eq. (6.10) and Eq. (6.11) will not hold exactly for the temperature profile of a turbulent disc with internal heating, but it is still to be expected that they will be fulfilled approximately for the time-averaged temperature profile.

We solve Eq. (6.5) with parameters corresponding to the “hot” model using a one-dimensional grid with 256 grid cells in the vertical direction. We use $\lambda = 1/3$ and set $T_0 = 2000$ K and $T_\mathrm{b} = 10$ K. Starting from a constant temperature of 2000 K, the temperature is evolved until an equilibrium is reached. In Fig. 6.3 we plot the resulting temperature profile, the optical depth and the opacity as a function of height [panels (a)-(c)]. For the equilibrium configuration we consider, the photosphere is located at about 4 scaleheights above the midplane. The corresponding effective temperature is about 260 K. The opacity is around ~ 1 g/cm^2 above three scaleheights and declines when going towards the midplane, reaching a value of ~ 0.1 g/cm^2 there.

In panel (d), we plot the quantity T^4/T_phot^4 vs. the optical depth, resulting in a perfect straight line of slope one, in accordance with Eq. (6.10). The radiation transport solver thus reproduces the analytical equilibrium solution perfectly. This test is complementary to the tests where the MRI growth rates are measured, as described in Chap. 4: The latter test problem describes a time-dependent problem without stratification, while the test problem described in this section consists of calculating an equilibrium temperature profile with the vertical stratification included.

6.3 Simulation Results I: “Hot” Disc Model

Tab. 6.2 provides an overview of the radiative simulations that have been performed according to the parameters chosen for the “hot” model. We perform simulations with different box sizes and resolutions. The lowest resolution chosen is $32 \times 64 \times 256$ (Model `R6`). We also perform a simulation at double the resolution in all directions (simulation `R6D`) and two simulations (`R7` and `R8`) with a larger box size in the vertical direction and

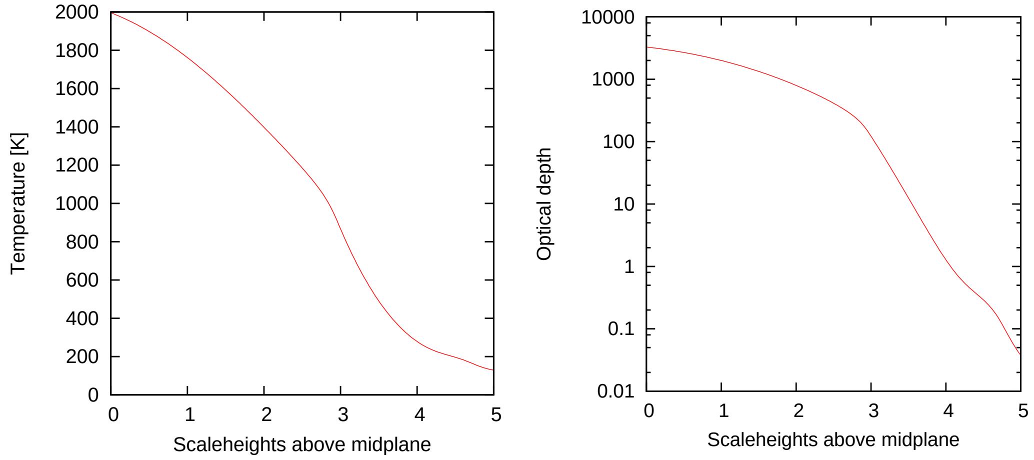

(a) Temperature profile.

(b) Optical depth.

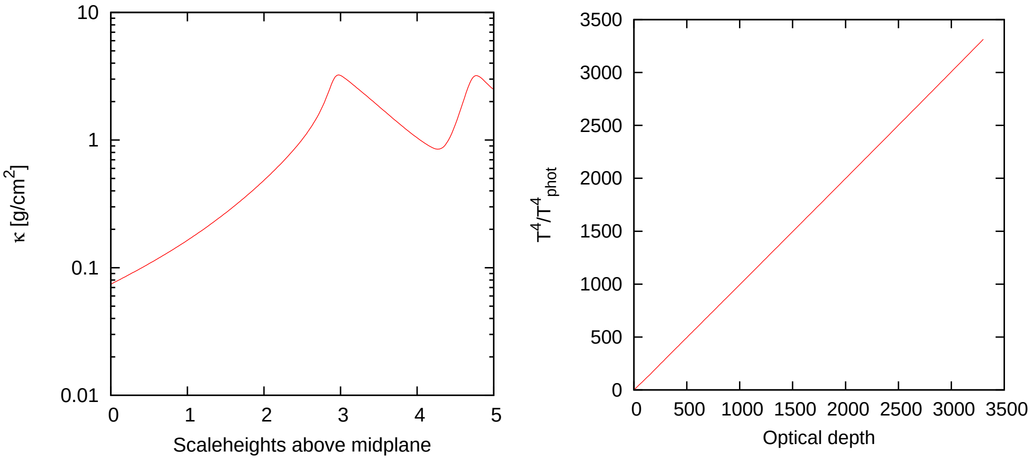

(c) Dust opacity.

(d) T^4-τ relation.

Fig. 6.3: *Vertical structure for a disc in hydrodynamical equilibrium with given inner and outer temperatures.* Panels (a)-(c) show the equilibrium solutions for the temperature, optical depth and the dust opacity as a function of height above the midplane. Panel (d) shows the relation between T^4 and the optical depth τ, which is a perfect straight line as predicted by the analytical calculation.

Name	Resolution	L_z	n_z/H_0	Orb.	$\langle\langle\rho\, v_x v_y\rangle\rangle/\langle\langle p\rangle\rangle$	$\langle\langle -B_x B_y\rangle\rangle/\langle\langle p\rangle\rangle$	$\langle\langle(\rho\, v_x v_y - B_x B_y)\rangle\rangle/\langle\langle p\rangle\rangle$
`R6`	32x64x256	$12H_0$	21	200	0.001 ± 0.001	0.004 ± 0.003	0.005 ± 0.004
`R7`	32x64x448	$14H_0$	32	150	0.003 ± 0.002	0.015 ± 0.010	0.018 ± 0.013
`R8`	32x64x512	$16H_0$	32	90	0.004 ± 0.002	0.018 ± 0.009	0.022 ± 0.011
`R6D`	64x128x512	$12H_0$	42	60	0.004 ± 0.002	0.017 ± 0.008	0.021 ± 0.010

Tab. 6.2: Overview of the radiative simulation runs for the “hot” model. The box size (third column) is measured in scaleheights H_0 referring to the initial gas pressure $p = \rho c_{\mathrm{s}}^2$ at the midplane. Since the pressure at the midplane does not change very much, this also corresponds very well to the actual pressure scaleheight during the simulation. The fourth column gives the number of grid cells n_z per scale height in the vertical direction. The fifth column tells the number of orbits for which the simulation has been run. The last three columns contain the time-averaged values of the turbulent stresses normalised to the space- and time-averaged pressure, as well as the standard deviation. Averages have been taken from 10 orbits until the end of the simulation.

a vertical resolution that is in between model `R6` and `R6D`, since recent results indicate that it is the resolution in the vertical direction that is critical in determining the value of the turbulent saturation level (see Chap. 5).

6.3.1 Time History

Starting from the initial state described in Sec. 6.2.5 the MRI starts to grow quickly and the non-linear state is reached already after a few orbits. After ten orbits the whole disc is fully turbulent and remains turbulent for the whole course of the simulation. Concerning the time history we now concentrate on model `R7`.

The "Butterfly" Pattern of Magnetorotational Turbulence

The turbulent state is not time-steady, but there are periods of high turbulent activity which are followed by periods where the disc is less active. This behaviour can be observed in Fig. 6.4, where various physical quantities are plotted as function of time for the first 80 orbits. Fig. 6.4(a) shows the horizontally averaged azimuthal component of the magnetic field (which is the dominant component). During an active phase the magnetic field is lifted upwards, leading to the typical butterfly structure. Scenarios that try to explain this behaviour invoke the Parker instability (Shi et al., 2010) or a dynamo mechanism (Gressel 2010). As one can estimate from Fig. 6.4(a), one cycle lasts between 10 and 20 orbits. Often the changes in turbulent activity are accompanied by magnetic field reversals in one or both sides of the disc. Unlike, the solar butterfly diagram, the field reversals shown in Fig. 6.4(a) do not follow a regular pattern and there is no strict correlation between the magnetic polarities in both sides of the disc.

Structure of the Corona

In Fig. 6.4(a) we also plot the location of the photosphere (defined as the location where the optical depth equals unity) and the position of the magnetosphere (defined as the location where the magnetic pressure starts to exceed the gas pressure). The photosphere is almost always located above the magnetosphere. During an active phase, the disc expands due to the stronger magnetic forces and the photosphere is pushed outwards. At the same time, the magnetosphere is pushed inwards due to the higher magnetisation caused by stronger turbulence. Therefore, for most of the time, the magnetically dominated region is for a large part optically thick. The same phenomenon has also been reported in the gas-pressure dominated simulation of (Hirose et al., 2006), although the physical regime for this simulation was quite different.

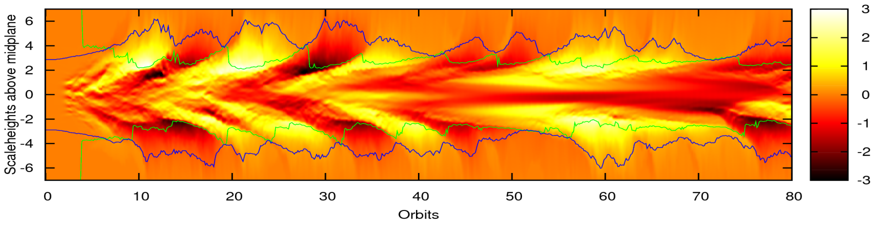

(a) Horizontally averaged azimuthal magnetic field component B_y normalised to the initial magnetic field strength B_0. The blue curve denotes the location of the photosphere and the green curve is the location at which magnetic pressure starts to exceed gas pressure.

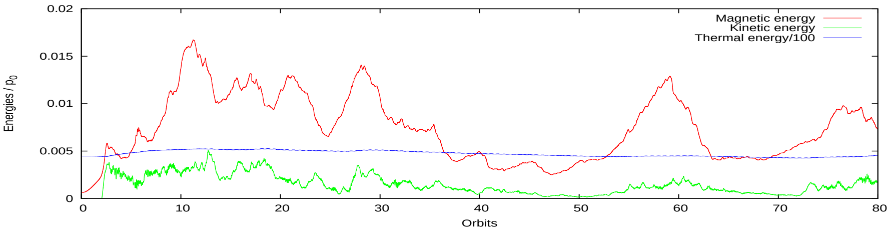

(b) Volume averaged magnetic, turbulent kinetic and thermal energy normalised to the initial gas pressure at the midplane. The gas internal energy is about 100 times the magnetic energy (note the different scaling).

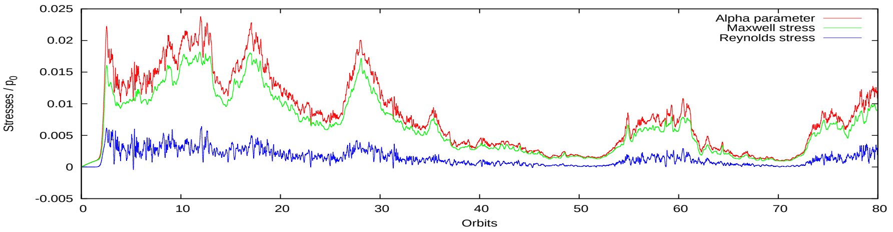

(c) Volume averaged turbulent stresses normalised to the mean gas pressure.

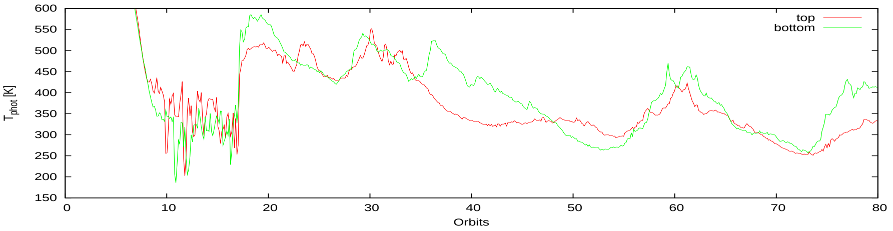

(d) Photospheric temperature at top and bottom boundary.

Fig. 6.4: Time history of various physical variables for model `R7` from 0 to 80 orbits illustrating the changes in turbulent activity and the correlations between stresses, magnetic field strength and luminosity of the disc. For further explanation see the text.

Energy Content of the Disc

We plot the time history of the energies (thermal energy, turbulent kinetic energy and magnetic energy) in Fig. 6.4(b). During active periods the magnetic energy is much larger then during a quiet period. The turbulent kinetic energy (that is the total kinetic energy minus the kinetic energy of the background shear flow) is also larger during active phases. In contrast to this, the long-term changes in the thermal energy are much smaller than the up-and-down variations, which shows that we have indeed reached thermal equilibrium.

Time-variability of the Luminosity

The turbulent stresses that determine the angular momentum transport in the disc are shown in Fig. 6.4(c). The angular momentum transport is dominated by the Maxwell stress which is about four to six times larger than the Reynolds stress. This ratio is consistent with previous results for stratified boxes (for example Stone et al., 1996). From a comparison between Fig. 6.4(b) and Fig. 6.4(c) it is evident that the magnetic energy and the alpha parameter are strongly correlated. Indeed, it is known that in shearing-box calculations, the time-dependence of the alpha parameter can be fitted by a formula of the form $\langle\alpha\rangle \propto \langle B^2\rangle + \text{const.}$ (see Brandenburg, 2008).

Finally, we may ask how the observational appearance of the disc will change due to phases of varying turbulent activity. To address this question, we plot in Fig. 6.4(d) the photospheric temperature (i.e. the temperature at the location where the optical depth equals unity). If we compare Fig. 6.4(d) with Fig. 6.4(c), it is obvious that in general a high degree of turbulent activity leads to a higher flux of radiation through the disc's boundaries. This observation can be made more quantitative by looking at the cross-correlation between alpha-parameter and photospheric temperature:

$$C(\tau) = \int [\langle\alpha\rangle(t-\tau) - \langle\langle\alpha\rangle\rangle][T_{\mathrm{phot}}(t) - \langle T_{\mathrm{phot}}\rangle]\,\mathrm{d}t. \tag{6.12}$$

Here, $\langle\alpha\rangle$ denotes the volume-averaged alpha parameter and T_{phot} is the arithmetic mean of the photospheric temperatures at top and bottom. The cross-correlation is shown in (Fig. 6.5). The lag τ between photospheric temperature and alpha parameter (as inferred from the peak in the correlation function) is about 2-3 orbits. We can compare this to the radiative diffusion timescale $\tau_{\mathrm{rad}} \approx H_0^2/D_{\mathrm{rad}}$, where the radiative diffusion coefficient D_{rad} is given by

$$D_{\mathrm{rad}} = 4acT^3/3c_{\mathrm{V}}\kappa\rho^2 \tag{6.13}$$

(cf. the appendix). When taking typical values $\rho = 2.0 \cdot 10^{-9}\,\mathrm{g\,cm^{-3}}$ and $T = 1700\,\mathrm{K}$ for the density and the temperature in the region near the midplane (see Fig. 6.7 and Fig. 6.8

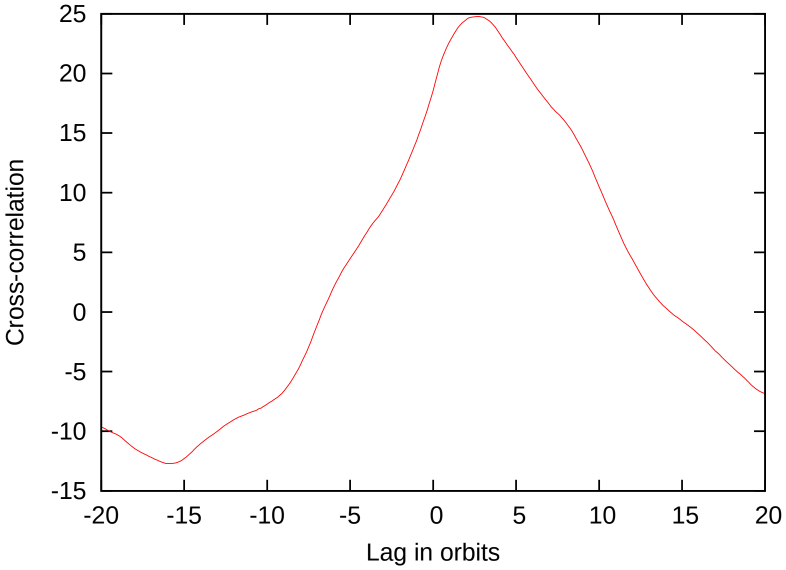

Fig. 6.5: Cross-correlation between alpha stress and photospheric temperature for model `R7`.

later in the paper), we get $\tau_{\mathrm{rad}} \sim 2.5$ orbits, so the lag between stress and photospheric temperature agrees well with the radiative diffusion timescale. Concerning the turbulent transport coefficient $D_{\mathrm{turb}} = v_z^2/\Omega$, we find that near the midplane D_{turb} is typically about one order of magnitude smaller than D_{rad}, so the energy transport by turbulent gas motions is negligible compared to the energy transport by radiative diffusion.

The connection between variations of the turbulent activity and oscillations in accretions discs has already been discussed in the literature, both in the context of local (Arras et al., 2006; Guan and Gammie, 2010), as well as global simulations (Machida and Matsumoto, 2008; O’Neill et al., 2010).[3] The global simulations showed that the characteristic “butterfly” pattern found in simulations of stratified magnetorotational turbulence is not just an artifact of the local approximation, but persists also in a global setup. However, in contrast to our simulations, neither of the works mentioned above did include radiation transport. These means that our simulations are the first where the connection between turbulent activity and changes in the disc luminosity has been explicitly calculated.

---

[3] The works mentioned where mostly concerned with accretion flows around compact objects.

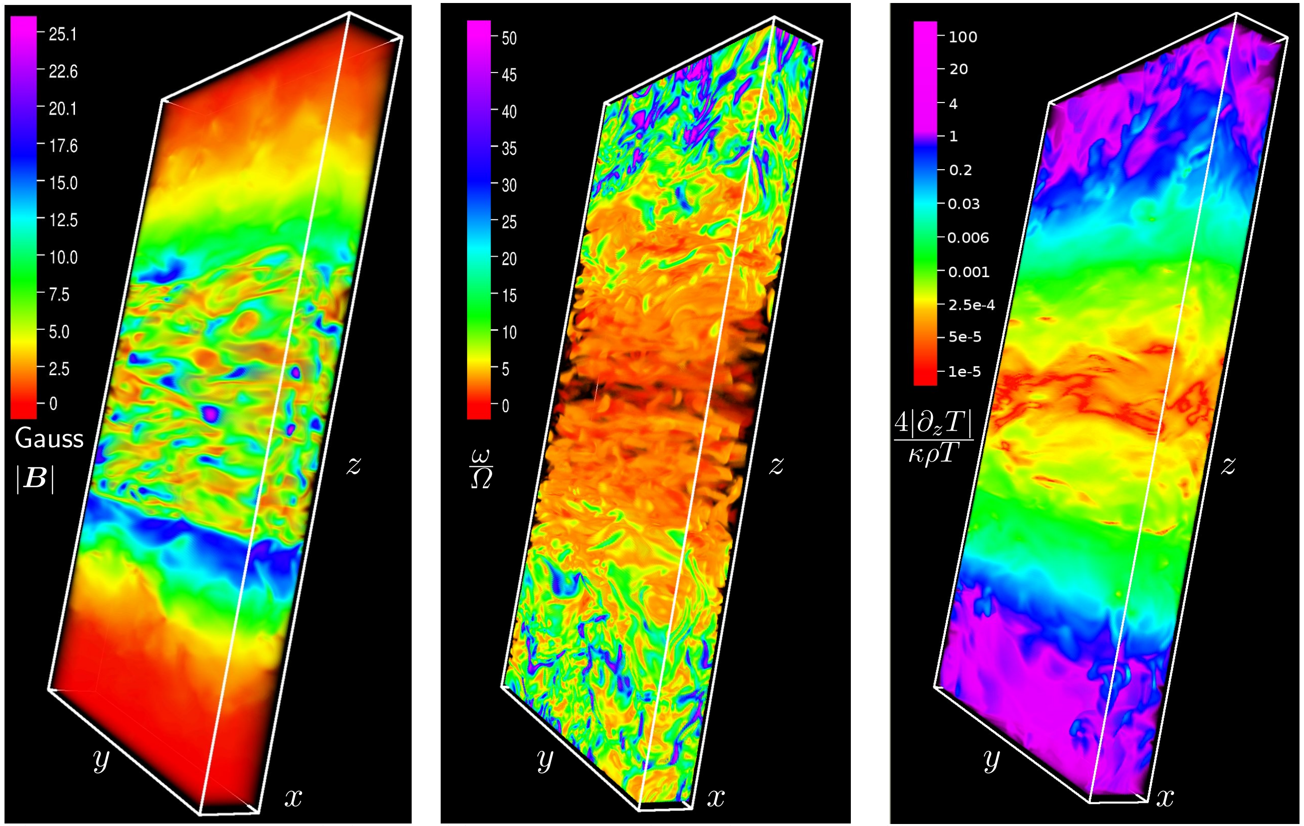
25.1
22.6
20.1
17.6
15.0
12.5
10.0
7.5
5.0
2.5
0
Gauss
$|\boldsymbol{B}|$
y
x
z
50
45
40
35
30
25
20
15
10
5
0
$\frac{\omega}{\Omega}$
y
x
z
100
20
4
1
0.2
0.03
0.006
0.001
2.5e-4
5e-5
1e-5
$\frac{4|\partial_z T|}{\kappa\rho T}$
y
x
z

(a) Magnetic field strength $|\boldsymbol{B}|$ measured in Gauss.

(b) Vorticity $\omega = |\boldsymbol{\nabla} \times \boldsymbol{v}|$ in units of angular orbital frequency Ω.

(c) Ratio of photon mean free path to the length over which the temperature varies.

Fig. 6.6: Snapshots from model `R6D` illustrating the two-layer structure of the disc. The plots in panels (a) and (b) have been taken at $t = 20$ orbits, the plot in panel (c) has been taken at $t = 21$ orbits. For further comments see the text. (Graphics have been produced using the VAPOR visualisation package.)

6.3.2 Vertical Structure

To get an impression of how the turbulent state looks like, the reader may first have a look at Fig. 6.6, where 3D snapshots of some physical quantities are shown for the high-resolution model `R6D`. Panel (a) depicts the magnetic field strength measured in Gauss. In panel (b) a plot of the vorticity measured in units of the angular orbital frequency Ω is shown. Panel (c) contains a plot of the quantity

$$R_z = \frac{|\partial_z E_{\mathrm{rad}}|}{\kappa\rho E_{\mathrm{rad}}} = \frac{4|\partial_z T|}{\kappa\rho T} \tag{6.14}$$

which is the ratio of the photon mean free path $\ell_{\mathrm{phot}} = 1/\kappa\rho$ to the typical length over which the radiation energy (or the temperature) varies.

Concerning the vertical structure, two regions with very different physical properties can be distinguished: On the one hand, there is the region near the midplane (the region inside the first three scaleheights). Here, the magnetic field strength is approximately uniform and of the order of several Gauss. The turbulence is subsonic (see Sec. 6.3.6 below) and many intertwined vortices can be observed. Since $R_z \ll 1$ the photons are diffusing in this region. On the other hand, there is the corona (the region outwards from 4 scaleheights) which exhibits markedly different features: Here, the magnetic field drops sharply, the flow is supersonic and characterised by strong shocks, and the photons are to a large part better described as free streaming rather than diffusing.

6.3.3 Density & Temperature Profile

One of the most interesting quantities that our radiative models are able to provide is the self-consistently calculated temperature profile. We plot the mean temperature profiles for our radiative models in Fig. 6.7. Except for the low resolution model `R6` all the radiative models yield quite similar temperature profiles. In the body of the disc, the temperature profile resembles an inverted parabola and becomes flat in the optically thin regions in the upper layers of the disc. Near the disc midplane, the temperature is about 1800 K. The mean position of the photosphere is located at about 5 scaleheights away from the midplane. The corresponding photospheric temperatures are of the order of 500 – 600 K. According to Eq. (1.27), which was derived in Chap. 1

$$\dot{M} = \frac{8\pi}{3}\frac{\sigma T^4 R_0^3}{G M_\odot} \tag{6.15}$$

this would correspond to an accretion rate $\dot{M}$ of order $10^{-5}\,M_\odot\,\mathrm{yr}^{-1}$. The accretion rate can also be estimated from the alpha parameter according to Eq. (1.25), which was also

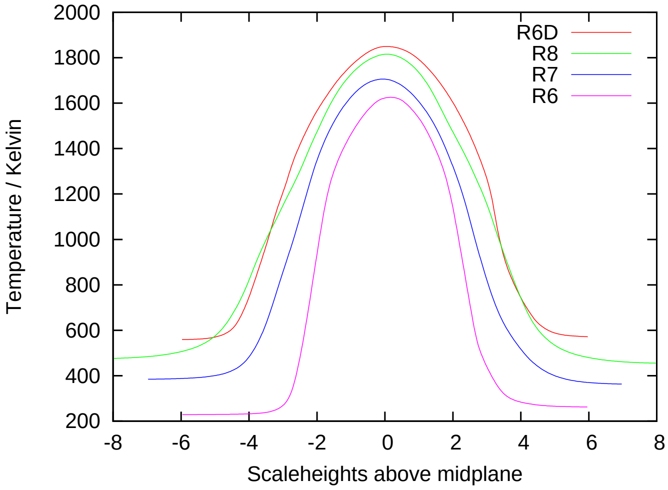

Fig. 6.7: Temperature profiles obtained for the radiative models. Averages have been taken from 20 orbits until the end of the simulation.

derived in Chap. 1,

$$\dot{M} = 3\pi\alpha c_{\mathrm{g}} H \Sigma_0. \tag{6.16}$$

Using $c_{\mathrm{g}} \approx c_{\mathrm{g0}}$ as well as $H \approx H_0$, and plugging in a value of $\alpha = 0.02$ for the alpha parameter (see Sec. 6.3.7), we get again an accretion rate of order $10^{-5}\,M_{\odot}\,\mathrm{yr}^{-1}$, so the two results are nicely consistent.

In Fig. 6.8 we compare the density profile obtained with model `R7` to the profile of the isothermal model `I7` from Chap. 5 and also to the initial profile. Away from the midplane, the density profile flattens due to the additional magnetic support. Since for the radiative model the temperature decreases outwards, the density in the upper layers is lower as compared to the isothermal model.

6.3.4 Magnetic Field

In our model, the radiation pressure is small compared to the gas pressure almost everywhere. This means that concerning the vertical support of the disc against gravity, radiation pressure plays no role, leaving only gas pressure and magnetic forces. As can be inferred from Fig. 6.9, where gas and magnetic pressure are plotted as a function of height, the midplane region inside the first three scaleheights is gas-pressure dominated. The magnetic pressure is approximately constant in the midplane region with a slight

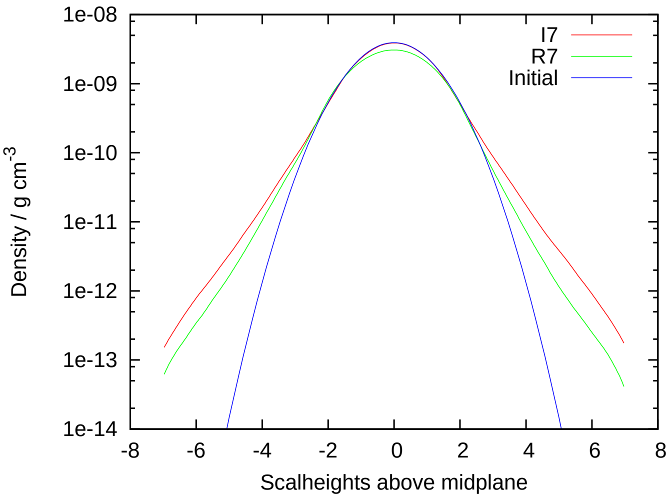

Fig. 6.8: Density profile for models `I7` and `R7`, averaged from 20 orbits until the end of the simulation. For comparison, the initial Gaussian density profile has also been plotted (blue line).

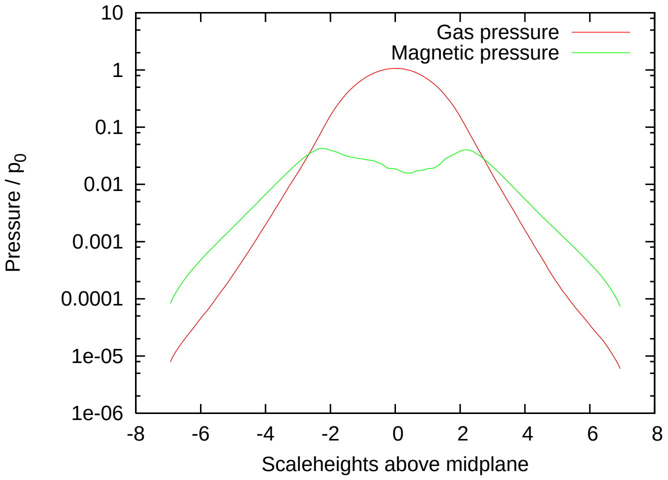

Fig. 6.9: Gas pressure and magnetic pressure for model `R7`. Averages have been taken from 20 orbits until the end of the simulation.

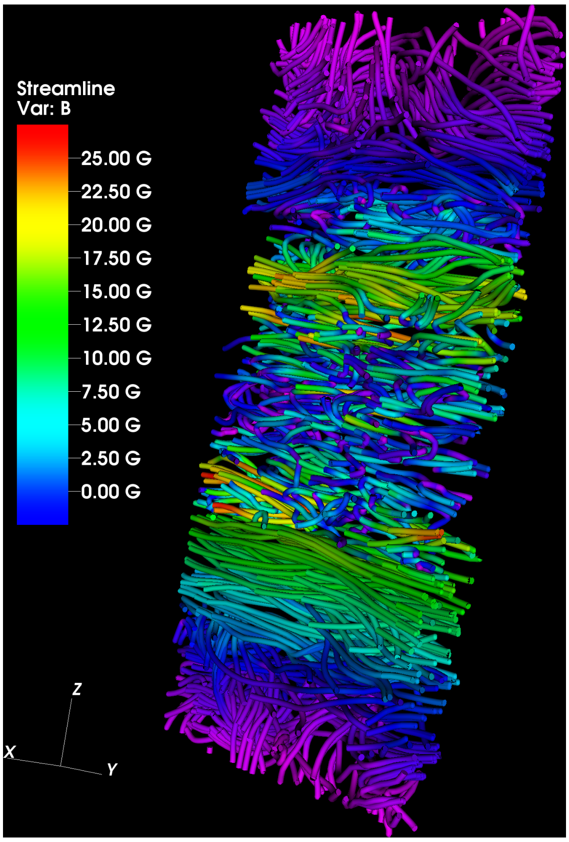

Fig. 6.10: Magnetic field configuration in model `R6D` taken from a snapshot at $t = 20$ orbits. Color-coded is the magnetic field strength, while the field line density is arbitrary in this plot.

increase outwards. Outside the midplane region, the magnetic pressure declines exponentially, but not as steep as the gas pressure. As a consequence, the disc's corona is magnetically dominated.

In Fig. 6.10 we plot the magnetic field lines. Near the midplane, in the MRI-unstable region, the field is highly tangled. Further outwards, where magnetic pressure becomes dominant, the field becomes predominantly azimuthal. Even further outwards, the magnetic field becomes irregular again (see also the discussion in (Suzuki and Inutsuka, 2009)).

The magnetic field strengths near the midplane are of the order of several Gauss. At this point, it is interesting to note that the field strengths generated by the MRI are

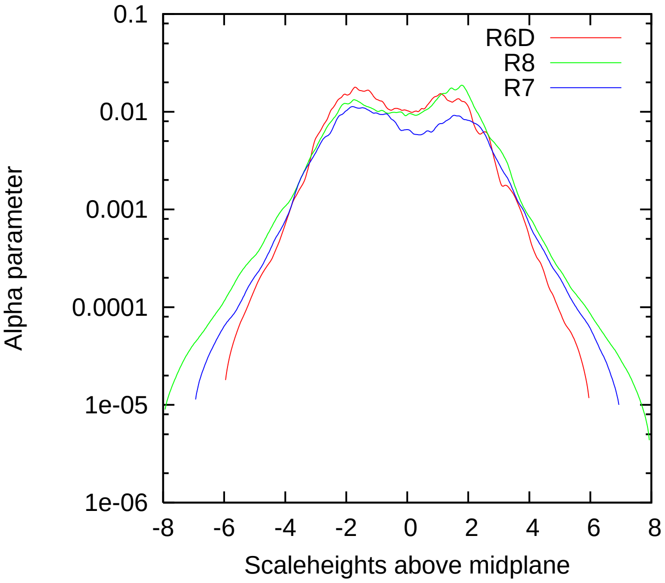

Fig. 6.11: Turbulent stresses as a function of height for the radiative models. Averages have been taken from 20 orbits until the end of the simulation.

thus consistent with the remnant magnetisation found in meteorites from the asteroid belt (Cisowski and Hood, 1991; King and Pringle, 2010).

6.3.5 Turbulent Stresses

We can determine the strength of the turbulence at different locations by measuring the turbulent stresses. This is done in Fig. 6.11, where vertical profiles of the alpha parameter are plotted for the radiative models. Note that except for the low resolution model `R6` all profiles are very similar, indicating convergence. We encounter a similar picture as in Fig. 6.9 for the case of the magnetic pressure: Inside the gas-pressure dominated midplane region the stress profiles are roughly constant with a slight increase outwards (with the exception of the low-resolution model `R6`, where the stresses drop noticeably at the midplane). Outside the midplane region, the stress profiles decline exponentially. This means that almost all the angular momentum transport happens in the midplane region and is there almost independent of height. In the corona, angular momentum transport is negligible.

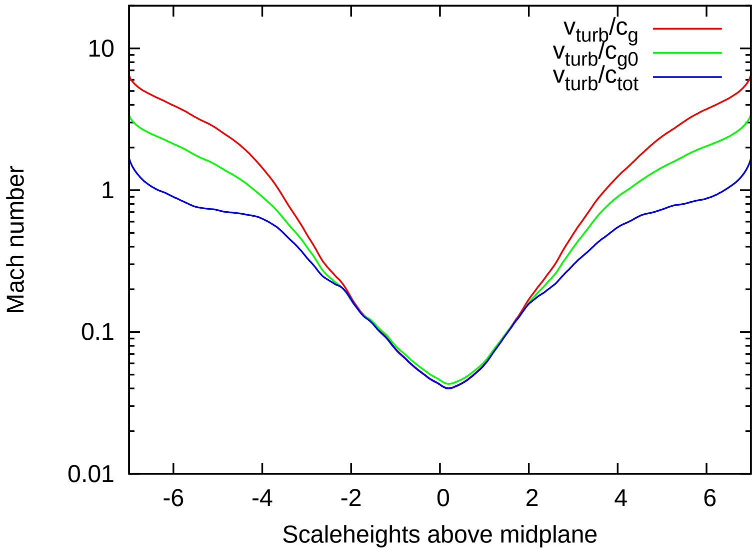

Fig. 6.12: Turbulent velocities for model `R7`, where c_g denotes the gas sound speed, c_g0 is the initial gas sound speed and c_tot is the total sound speed (including gas and magnetic pressure).

6.3.6 Turbulent Velocities

We now look at the velocity distribution in the disc. In Fig. 6.12 we plot the horizontally averaged turbulent velocity $\boldsymbol{v}_\mathrm{turb} = \boldsymbol{v} - \boldsymbol{v}_\mathrm{kep}$ normalised by the gas sound speed as a function of height. In the midplane region, the turbulence is subsonic, while in the corona it becomes highly supersonic, exceeding Mach 5 at the boundaries. For comparison with other works we also plot the velocity normalised to the initial isothermal sound speed at the midplane and the velocity normalised to the total sound speed c_tot, where $c_\mathrm{tot}^2 = (p + B^2/8\pi)/\rho$. Our results are in agreement with the isothermal simulations done by Miller and Stone (2000) who report Mach numbers of about two and with HKS, who report Mach numbers (with respect to the total sound speed) between one and two.

From Fig. 6.6, middle panel, where a snapshot of the vorticity is plotted, on can appreciate the highly dynamic and tangled nature of the velocity field. In the subsonic midplane region many intertwined vortices can be distinguished. Vortices have been proposed as a means of trapping dust particles, thereby helping the formation of larger bodies by enhancing the number of collisions and slowing down the spiraling into the star (Barge and Sommeria, 1995; Tanga et al., 1996). However, the vortices in our simulations are rather short-lived, usually lasting much shorter than one orbit, so particle trapping in the MRI-generated vortices in the midplane region will not be efficient.

In observations, the turbulence will show itself in the form of a broadening of spectral lines due to the velocity dispersion induced by it. At the mean location of the photosphere the turbulent velocities are about Mach 2-3 which implies a significant effect on the line widths. The detection of CO overtone emission in young stellar objects (YSOs) provides a useful diagnostic tool to detect turbulent line broadening. The reason for this is that the near overlap of CO transitions near the $v = 2 - 0$ band allows a separation of the local broadening (e.g. turbulence) from the macro-broadening (caused for example by a disc wind). In the case of several YSOs, there is indeed substantial empirical evidence for supersonic turbulent line broadening of the magnitude that we find in our simulations (Najita et al., 1996; Carr et al., 2004; Hügelmeyer, 2009).

6.3.7 Turbulent Saturation Level

As has already been remarked in the introduction, in numerical simulations of MRI turbulence, the turbulent saturation level is influenced by a number of numerical factors. By performing a suite of simulations with different box sizes an at different resolutions, we are able to gauge the strength of the influence of these numerical parameters.

In Fig. 6.13 we plot the values of the alpha parameter for the isothermal models of Chap. 5 (as given in Tab. 5.1), as well as for the radiative runs corresponding to the "hot" model (as given in Table 6.2). When increasing the resolution from 32x64x256 (models `I6` and `R6`), to the double resolution of 64x128x512 (models `I6D` and `R6D`), the values of the stresses increase considerably. A similar increase of the stresses is observed also when only the resolution in the vertical direction is increased (models `I5`, `I7`, `R7` and `R8`), which is analogous to what has been found in the radiative simulations of (Shi et al., 2010). A look at Fig. 6.11 suggests that it is especially the region near the midplane that is not sufficiently resolved, since the stress drops there noticeably, while in the better resolved models it does not.

The results depicted in Fig. 6.13 suggest that once a resolution of about 30 grid cells per scaleheight in the vertical direction has been achieved, the results will no longer significantly depend on the numerical resolution. All models except `I6` and `R6` are consistent with an α-value of about $\alpha \sim 0.015 - 0.02$, with the isothermal models yielding somewhat lower stresses that are closer to the lower end of $\alpha \sim 0.015$, while the stresses found in the radiative models are grouped around the value $\alpha \sim 0.02$. No tendency is found for the turbulent saturation level to change with respect to neither the vertical box size nor the resolution in the radial and azimuthal directions.

As a consequence of the lower stress, the heating in the low-resolution model `R6` is also smaller than compared to the other radiative models, leading to significantly lower

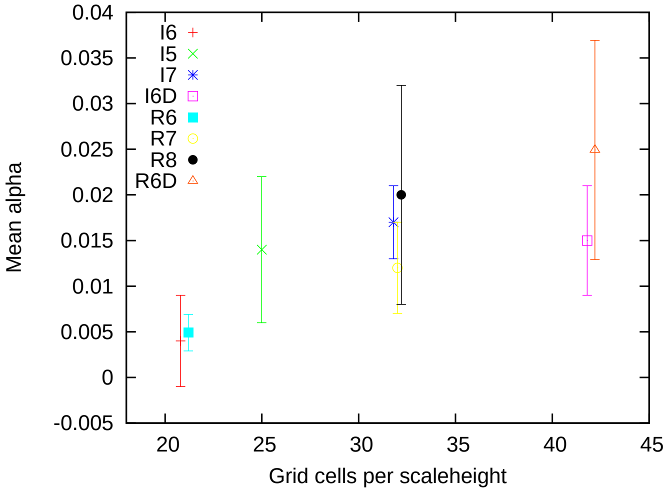

Fig. 6.13: Time-averaged value of the alpha parameter as a function of the number of grid cells in the *vertical* direction per scale height for all models. The "error bars" correspond to the deviation from the mean value.

temperatures in this model. Apart from this, the temperature profile for model `R6` is qualitatively similar to the other models.

As has already remarked before, the heating does intrinsically depend on numerical effects. However, as can be seen from Fig. 6.7, the temperature profiles for the better resolved models (`R7`, `R8` and `R6D`) are very similar, suggesting that the heating rates are also converged.

6.4 Simulation Results II: "Cool" Disc Model

We now describe the already mentioned "cool" disc model, which is located further away from the star than the "hot" model and uses a lower surface density. We choose the same setup as for the "hot" model, except that we place the simulation domain at a distance of 5 AU from the central star, and we choose a surface density of 456 $\mathrm{g\,cm^{-2}}$. In this model, we start with an initial temperature of $T_0 = 125\,\mathrm{K}$. All other physical parameters are the same as for the "hot" model. We use the HLLD Riemann solver for all runs of the "cool" model.

We perform one run that includes Ohmic resistivity. For this simulation, the ionisation level is calculated on the basis of a model that includes as ionisation sources stellar X-

Parameter	Symbol	Value
Radial box size	L_x	0.27 AU
Azimuthal box size	L_y	1.63 AU
Vertical box size	L_z	2.18 AU
Mass of central star	M_*	$1\,M_\odot$
Distance to central star	R_0	5 AU
Surface density	Σ_0	$456\ \mathrm{g\,cm^{-2}}$
Adiabatic index	γ	1.4
Mean molecular weight	μ	2.35
Grain size	a_d	$10\,\mu\mathrm{m}$
Dust-to-gas ratio	$\rho_\mathrm{d}/\rho_\mathrm{g}$	0.01

Tab. 6.3: Summary of basic physical parameters for the "cool" model.

rays, cosmic rays and the decay of radionuclides. The recombination rate is calculated on the basis of a simple chemical network as proposed by Oppenheimer and Dalgarno (1974). We assume grains of size $10\,\mu\mathrm{m}$ and a dust-to-gas ratio of 0.01. The details of the chemical model are described in Ruoff (2010). The resistivity is calculated according to the formula

$$\eta = 230\,(T/K)^{1/2}\,\chi^{-1}\,\mathrm{cm^2\,s^{-1}}, \tag{6.17}$$

where $\chi = n_\mathrm{e}/n_\mathrm{n}$ is the ionisation level. For a summary of the physical parameters of these model, see Table 6.3.

Tab. 6.4 provides an overview of the runs performed. Run `ri16` is a low resolution run that uses ideal MHD. In addition, we perform a run at double the resolution (run `ri32`) and a run where resistivity is switched on (run `rc16`). The ideal runs both yield similiar values for the turbulent stresses, which shows that when using the HLLD Riemann solver, already a resolution of 16 grid cells per scaleheight does produce meaningful results.

6.4.1 Time History

In Fig. 6.14, we show space-time diagrams of the density, the turbulent Mach number and the magnetic energy. Since the simulation domain covers only 4 scaleheights in the vertical direction, the disc looses some of it's mass, as can be seen in the upper panel of Fig. 6.14.

The turbulence is subsonic throughout most of the simulation domain and becomes supersonic only near the vertical boundaries (middle panel of Fig. 6.14). The photosphere

Name	Resolution	Chem.	n_z/H_0	Orbits	$\langle\langle\rho\, v_x v_y\rangle\rangle/\langle p_0\rangle$	$\langle\langle -B_x B_y\rangle\rangle/\langle p_0\rangle$	$\langle\langle(\rho\, v_x v_y - B_x B_y)\rangle\rangle/\langle p_0\rangle$
`ri16`	16x32x128	no	16	75	0.006	0.031	0.037
`ri32`	32x64x256	no	32	75	0.007	0.029	0.036
`rc16`	16x32x128	yes	16	75	0.0002	0.0031	0.0033

Tab. 6.4: Overview of the simulation runs for the “cool” model. The fourth column gives the number of grid cells in_z per scale height in the vertical direction. The fifth column tells the number of orbits for which the simulation has been run. The last three columns contain the time-averaged values of the turbulent stresses normalised to the mean initial pressure. Averages have been taken from 10 orbits until the end of the simulation, except for model `sc16`, where the averages have been taken starting from 30 orbits until the end of the simulation.

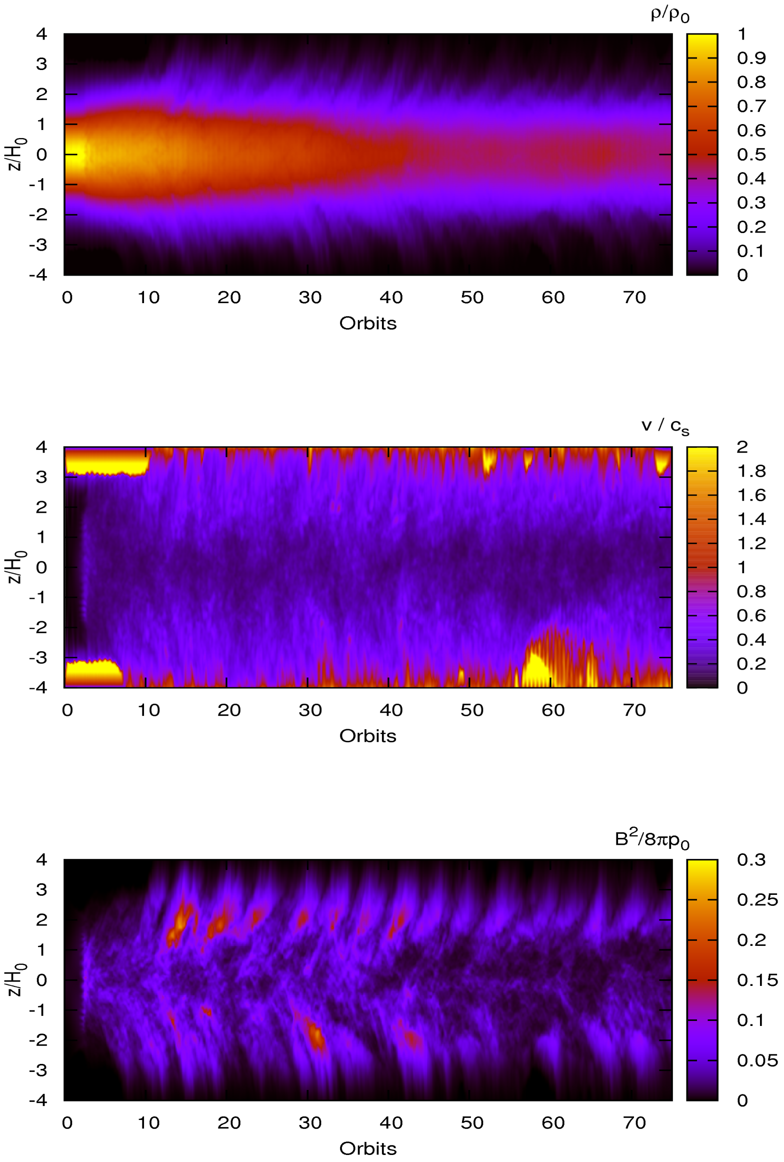

Fig. 6.14: *Time history of model* `ri32`*.* Shown are space-time plots of the following quantities (from top to bottom): Density (normalised to initial midplane density), turbulent Mach number, magnetic energy (normalised to the initial midplane pressure). Note that the middle panel shows the Mach number with respect to the initial isothermal soundspeed at the midplane.

(which is not shown in the plot) is located in the region slightly upwards of 3.5 pressure scaleheights away from the midplane. This means that the finding of a supersonic turbulent Mach number at the location of the photosphere, which was established for the "hot" disc model in the last section, does also hold for the "cool" disc model.

Concerning the magnetic field, we find the same "butterfly" pattern as for the "hot" disc model, which has been simulated using the HLL Riemann solver (lower panel of Fig.6.14). During the end of the simulation, the magnetic field becomes a bit weaker, since due to the small box size, some of the mass is lost through the vertical boundaries.

6.4.2 Turbulent Stresses

We plot the turbulent stresses for the models `ri16`, `ri32` and `rc16` in Fig.6.15. From the upper and middle panel of Fig. 6.15 it is clear that the simulations have reached a meaningful quasi-steady turbulent state. Also, the stress patterns for model `ri16` and `ri32` are very similar.

Concerning the resistive model `rc16` we let this model run with resistivity turned off for the first twenty orbits, therefore during this phase the evolution is similar to model `ri16`. Shortly after $t = 20$ orbits, where a saturated turbulent state has been reached, we switch on the resistivity. During the next ten orbits, a MRI-inactive dead zone forms near the disc midplane, while the upper layers still show signs of turbulent activity. Although the MRI is quenched near the midplane, the value of Maxwell and Reynolds stresses do not drop to zero there, so there is some angular momentum transport going on even in the MRI inactive region. This phenomenon has also been reported in other works (for example Fleming and Stone, 2003; Oishi and Mac Low, 2009). Possible reasons for this are hydrodynamic waves, that are activated by the turbulence in the upper layers and penetrate to the midplane Oishi and Mac Low (2009); as well as the diffusion of radial magnetic fields towards the midplane, where the shear generates an azimuthal field, resulting in a non-zero *laminar* Maxwell stress Turner and Sano (2008). However, the overall angular momentum transport is much smaller than in the ideal case (see the plots of the alpha parameter in Fig. 6.16)).

6.4.3 Temperature

A space-time plot of the temperature for the models `ri16`, `ri32` and `rc16` can be found in Fig. 6.17 In the ideal models (upper two panels), the temperature decreases with time due to the mass loss. Concerning the resistive model `rc16`, it cools rather quickly after the resistivity has been switched on, since the turbulent heating becomes very small. At the end of the simulation, the models `ri16` and `ri32` have a midplane temperature

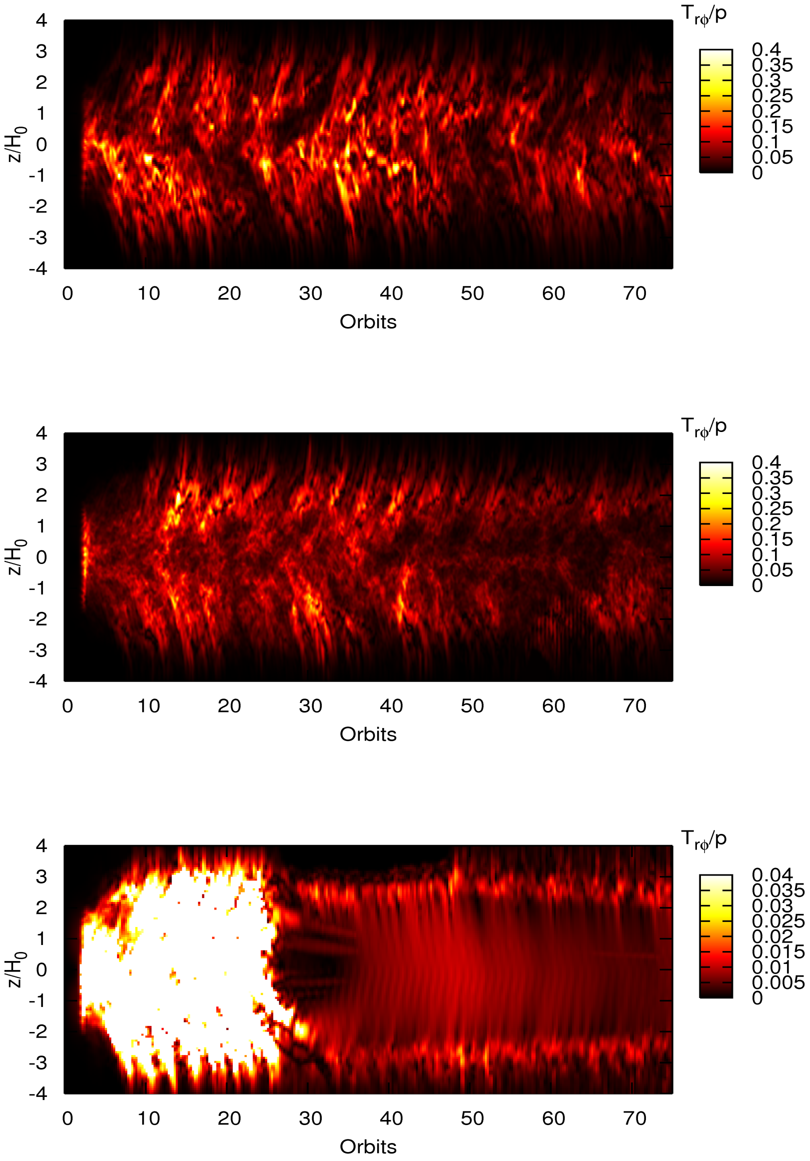

Fig. 6.15: Shown are the turbulent stresses (absolute values) for the following models (from top to bottom): `ri16`, `ri32` and `rc16`. The stresses are normalised to the initial gas pressure (therefore the values for the stresses are smaller than the one given in Tab. 6.2). Note the different color scale in the last panel.

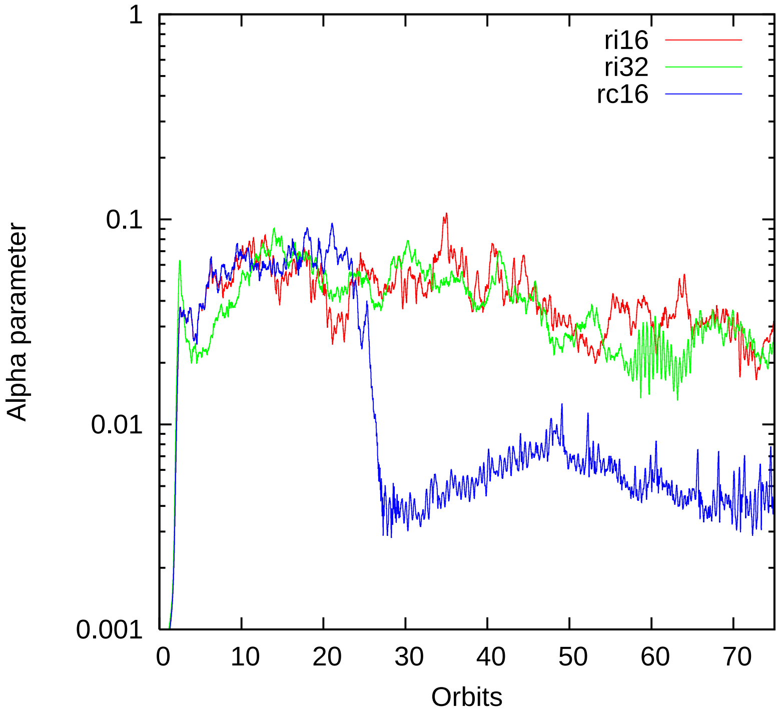

Fig. 6.16: Shown is the alpha parameter for the runs corresponding to the “cool” model. Concerning the resistive model `rc16`, resistivity is switched on just after 20 orbits.

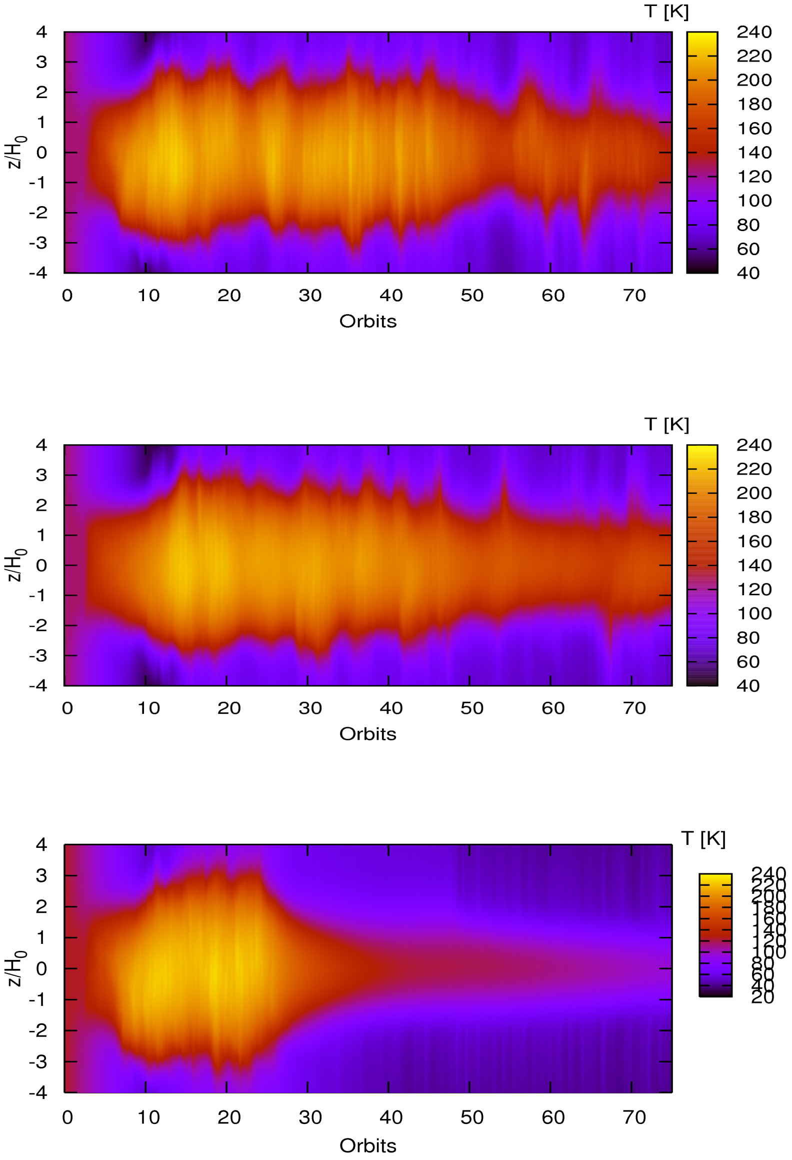

Fig. 6.17: Shown are space-time plots of the temperature for the following models (from top to bottom): `ri16`, `ri32` and `rc16`. Note that the temperature decreases in time because the disc looses part of its mass.

$\sim$ 150 K and a photospheric temperature $\sim$ 70 K, while model `rc16` has a midplane temperature $\sim$ 100 K and a photospheric temperature $\sim$ 45 K.

6.5 Summary

In the present chapter we have described 3D radiation-magnetohydrodynamics simulations of magnetorotational turbulence in protoplanetary discs. Ours are the first simulations that include a detailed treatment of radiation transport, allowing us to obtain a self-consistent picture of the vertical structure which results from a dynamic balance between turbulent heating and radiative cooling. Our simulations do not only contain a much greater level of realism as compared to previous isothermal simulations, but are also an important step towards bringing numerical simulations into contact with observations. We summarise the most important results of our study:

- In our models two regions can be distinguished: A gas-pressure dominated midplane region where most of the angular momentum transport takes place, and a magnetically dominated corona where the MRI is quenched and angular momentum transport is negligible.
- The position of the photosphere is highly variable due to changing turbulent activity, but is usually located above the point where magnetic pressure starts to dominate gas pressure. The variations in the turbulent activity lead to oscillations in the disc's luminosity, which we model for the first time using radiation transport.
- Magnetic field strengths generated by the MRI are compatible with the remanent magnetisation found in meteorites.
- The turbulent Mach number found at the location of the photosphere is consistent with the Mach number derived from the (turbulent) line broadening of CO lines found in observations of young stellar objects. This supports the assuption that the MRI is active in theses systems.

We concentrated our work on simulations of the inner, hotter parts of protoplanetary discs, where non-ideal MHD effects can be neglected. In addition, we have also started to model the cooler parts, where one has to include the effect of Ohmic resistivity. The calculation of the resistivity is done on the basis of a simplified chemical network, leading to a fully self-consistent protoplanetary disc model. We believe that the numerical setup that we developed will be a very important tool for future research.

Chapter 7: Summary and Outlook

In this thesis, we performed numerical simulations of turbulence in protoplanetary discs which is driven by the magnetorotational instability (MRI). We employed the local approximation, where the computational domain covers only a small part in the radial direction of the disc, which allows one to achieve much higher spatial resolutions than in a global setup. Since our calculations are the first of this type which do include radiation transport, they deliver, as of today, the most detailed picture of the vertical structure of an MRI-turbulent protoplanetary disc.

We started our presentation in Chapter 1 with a brief overwiev of the basics of protoplanetary disc physics. Protoplanetary discs are accretion discs around young stars which typically last for only a few million years. This observation poses the important question of what mechanism actually powers the accretion process. The most widely accepted answer to this problem is MRI-driven internal turbulence.

We then developed in Chapter 2 the general mathematical framework for the calculations to be performed in this thesis. We describe the disc gas by the equations of radiation-magnetohydrodynamics. Restricting ourselves to the planet-forming region within the first ten AU, we can neglect all non-ideal magnetohydrodynamical effects except Ohmic resistivity.

In Chapter 3, we started our research work by performing a local stability analysis of a rotating, magnetised shear flow including both radiation transport and resistivity. Our calculation yields the most general MRI dispersion relation in the astrophysical literature and is applicable for for a wide range of astrophysical accretion flows, including both a cool, poorly ionised protoplanetary disc and the opposite extreme of a hot, fully ionised accretion disc around a black hole. We verified our analytical calculations by performing numerical simulations of single MRI modes. These simulations also proved very useful in comparing the performance of different MHD solvers and verifying the numerical implementation of the radiation transport and resistivity parts.

After having finished our study of the linear growth phase of the MRI, we moved on to 3D numerical simulations of MRI-driven turbulence (Chapter 4). For our study we choose the local shearing-box approximation, which means simulating a small rectangular domain located near the midplane of an accretion disc; where we neglect the vertical component of gravity and use special, “shear-periodic”, boundary conditions in the radial direction that are consistent with the background shear flow. We restrict ourselves to the case where the disc is threaded by an external magnetic field, meaning that there is a well-defined driving scale for the turbulence, namely the wavelength of the fastest growing mode that fits in the box.

First, we compare different MHD codes by performing runs with the same parameters using four different codes, namely `ZEUS`, `NIRVANA`, `CRONOS` and `ATHENA`. We find that for the net-flux model that we simulated, all four codes produce rather similar results for the turbulent saturation level, even at low resolutions. This result is not surprising, since once the fastest growing mode is well resolved, the simulation outcome will likely not depend much on numerical factors. The same can, however, not be said of the heating rates. Since we do not include any physical dissipation, the dissipation in the simulations is determined by numerical effects taking place at the grid scale. In our low resolution simulations, we find significant differences between the various codes concerning the heating rates. From this we conclude that it is important to perform runs at different resolutions in order to check if the results are actually converged.

When including radiative diffusion into our simulations, we find that it reduces the saturation level of the magnetorotational turbulence. By making a connection to our study of the linear growth phase, we can provide a simple possible explanation for this: In the net-flux case we are considering, the turbulence is driven by the fastest growing vertical mode. Due to the background shear, the magnetic field in the turbulent state has a dominant azimuthal component, meaning that the growth rates of the vertical modes are reduced by radiative diffusion. As a consequence, the driving of the turbulence is weaker when radiative diffusion is present, leading to a lower saturation level.

As the logical next step towards more realistic models of MRI-turbulent protoplanetary discs, we include the vertical component of gravity (Chapter 5). As a consequence, the vertical structure looks no longer uniform. The density is given roughly by a Gaussian profile, with very low density in the upper layers. As a consequence, a magnetically dominated corona forms above and below approximately three pressure scaleheights away from the midplane. This leads to numerical difficulties due to a small timestep limited by the Alfvén speed, and also due to problems with the magnetic field near the vertical boundaries. We find that vertical field boundary conditions for the magnetic field are a very good choice, because they are numerically quite stable and also do not distort the magnetic field near the boundaries significantly.

We start with simulations that use an isothermal equation of state. While such an approach is not realistic for protoplanetary discs, we take this simulations to serve both as a test for our vertically stratified setup and also later to compare results between isothermal and radiative simulations. We choose a setup where the net vertical magnetic flux through the computational domain is zero. This means that there is no external driving, but the fate of the turbulence depends instead on the working of an internal dynamo process. We perform runs at different resolutions and using different box sizes. The result is that the turbulent saturation level is similar for simulation that use a resolution of about 30 grid cells per pressure scale height and more.

We then perform vertically stratified simulations including radiation transport (Chapter 6). In order to arrive at a self-consistent model, that includes all the relevant physics, we choose a rather high surface density (corresponding to a massive protoplanetary disc in the early stages of its evolution), and we place our simulation domain near to the star, at a distance of 1 AU. The temperatures that come out of our model are of the order of 1000 K, which is enough for collisional ionisation to be effective, such that we can assume ideal MHD. In the vertically stratified models, the turbulent activity shows oscillations on a timescale of 10-20 orbits, leading to a typical "butterfly" structure when plotting quantities such as the density, the magnetic field or the turbulent stresses in a space-time diagramm. We find that associated with these oscillations are fluctuations in the luminosity of the disc. Since the butterfly pattern is also observed in global simulations (i.e. it is not just an artifact of the local approximation), the changes in the luminosity are a possible observable signature of stratified magnetorotational turbulence.

The vertical structure of the disc that comes out of our simulations is made up of two layers with very different physical conditions: A midplane layer extending about three scaleheights above both sides of the equator, where the disc is gas-pressure dominated, the turbulent stresses are approximately uniform, the turbulence is subsonic and the disc gas is optically thick; and a magnetically dominated corona, where angular momentum transport is negligible, the fluid motions are supersonic and the photons are better described as free streaming rather than diffusing. It is interesting to note that the magnetic field strengths generated by the MRI (which are of the order of several Gauss) are compatible with the remanent magnetisation found in meteorites. A possible direct observational consequence that can be derived from our simulations is the broadening of spectral lines due to the velocity dispersion induced by the turbulence. The turbulent Mach number of 2-3 at the photosphere, that we find in our simulations, is indeed the same as that derived by the fitting of spectral lines due to CO overtone emission. We conclude that this result supports the assumption that MRI-turbulence is active in protoplanetary discs.

Concerning the resolution dependence of the turbulent saturation level, we find similar results as in the case of the isothermal models, namely that as soon as a resolution of ~ 30 grid cells per pressure scale height is reached, the results do no longer significantly depend on the resolution, and also not on the size of the computational domain. With respect to the temperature profile, we also find that for the well resolved runs the mean temperature profiles are similar. This means that both the turbulent saturation level and the heating rates are reasonably converged, suggesting that the results are indeed reliable.

The next logical step in our work is to simulate models of cooler regions of protoplanetary discs, where non-ideal MHD effects are no longer negligible. We are currently running such simulations, including both radiation transport and an Ohmic resistivity. With this setup we are able to cover the full range of the planet-forming region inside the disc, using a fully self-consistent model of an MRI-turbulent protoplanetary disc. Since the curvilinear coordinates of the `CRONOS` have by now been extensively tested, we will also be able to perform global protoplanetary disc simulations covering a large radial range. We believe that the numerical setup and methods that we developed during this thesis will prove to be a very important tool for future research.

Bibliography

Andrews, S. M., and J. P. Williams. “High-Resolution Submillimeter Constraints on Circumstellar Disk Structure.” *ApJ* **659**, 705 (2007)

Armitage, P. J. “Turbulence and Angular Momentum Transport in Global Accretion Disk Simulation.” *ApJ* **501**, L189 (1998)

———. “Dynamics of Protoplanetary Disks.” `arXiv:1011.1496A`

Arras, P., O. Blaes, and N. J. Turner. “Quasi-periodic Oscillations from Magnetorotational Turbulence.” *ApJ* **645**, L65 (2006)

Balbus, S. A. “Enhanced Angular Momentum Transport in Accretion Disks.” *ARA&A* **41**, 555 (2003)

———. “Magnetohydrodynamics of Protostellar Disks.” In *Physical Processes in Circumstellar Disks around Young Stars*, edited by P. Garcia, 2011

Balbus, S. A., and J. F. Hawley. “A powerful local shear instability in weakly magnetized disks. I - Linear analysis. II - Nonlinear evolution.” *ApJ* **376**, 214 (1991)

Balbus, Steven A., and John F. Hawley. “Instability, turbulence, and enhanced transport in accretion disks.” *Rev. Mod. Phys.* **70**, 1 (1998)

———. “An Exact, Three-dimensional, Time-dependent Wave Solution in Local Keplerian Flow.” *ApJ* **652**, 1020 (2006)

Balsara, D. S., and C. Meyer. “Evaluating the Magnetorotational Instability’s Dependence on Numerical Algorithems and Resolution.” `arXiv:1006.2146B`

Balsara, D. S., and D. S. Spicer. “A Staggered Mesh Algorithm Using High Order Godunov Fluxes to Ensure Solenoidal Magnetic Fields in Magnetohydrodynamic Simulations.” *Journal of Computational Physics* **149**, 270 (1999)

Barge, P., and J. Sommeria. “Did planet formation begin inside persistent gaseous vortices?” *A&A* **295**, L1 (1995)

Bell, K. R., and D. N. C. Lin. “Using FU Orionis outbursts to constrain self-regulated protostellar disk models.” *ApJ* 427: (1994) 987–1004.

Blaes, O., and A. Socrates. “Local Dynamical Instabilities in Magnetized, Radiation Pressure-supported Accretion Disks.” *ApJ* 553: (2001) 987–998.

Blaes, O. M., and S. A. Balbus. “Local shear instabilities in weakly ionized, weakly magnetized disks.” *ApJ* 421: (1994) 163–177.

Blaes, O. M., S. W. Davis, S. Hirose, J. H. Krolik, and J. M. Stone. “Magnetic Pressure Support and Accretion Disk Spectra.” *ApJ* 645: (2006) 1402–1407.

Brandenburg, A. “Turbulent protostellar discs.” *Physica Scripta* 014016.

Brandenburg, A., A. Nordlund, R. F. Stein, and U. Torkelsson. “Dynamo-generated Turbulence and Large-Scale Magnetic Fields in a Keplerian Shear Flow.” *ApJ* 446: (1995) 741–+.

Carr, J. S., A. T. Tokunaga, and J. Najita. “Hot H_2O Emission and Evidence for Turbulence in the Disk of a Young Star.” *ApJ* 603: (2004) 213–220.

Chiang, E. I., and P. Goldreich. “Spectral Energy Distributions of T Tauri Stars with Passive Circumstellar Disks.” *ApJ* 490: (1997) 368–+.

Cho, J., and A. Lazarian. “Grain Alignment and Polarized Emission from Magnetized T Tauri Disks.” *ApJ* 669: (2007) 1085–1097.

Cisowski, S. M. and L. L.Hood. “The `RELICT` magnetism of meteorites.” In *The Sun in Time*, edited by C. P. Sonett, M. S. Giampapa & M. S. Matthews. 1991, 761–784.

Colella, P., and P. R. Woodward. “The Piecewise Parabolic Method (PPM) for Gas-Dynamical Simulations.” *Journal of Computational Physics* 54: (1984) 174–201.

Davis, S. W., J. M. Stone, and M. E. Pessah. “Sustained Magnetorotational Turbulence in Local Simulations of Stratified Disks with Zero Net Magnetic Flux.” *ApJ* 713: (2010) 52–65.

Desch, S. J. “Mass Distribution and Planet Formation in the Solar Nebula.” *ApJ* 671: (2007) 878–893.

Dullemond, C. P., D. Hollenbach, I. Kamp, and P. D’Alessio. “Models of the Structure and Evolution of Protoplanetary Disks.” *Protostars and Planets V* 555–572.

Dutrey, A., S. Guilloteau, G. Duvert, L. Prato, M. Simon, K. Schuster, and F. Menard. "Dust and gas distribution around T Tauri stars in Taurus-Auriga. I. Interferometric 2.7mm continuum and ˆ13ˆCO J=1-0 observations." *A&A* 309: (1996) 493–504.

Dzyurkevich, N., M. Flock, N. J. Turner, H. Klahr, and T. Henning. "Trapping solids at the inner edge of the dead zone: 3-D global MHD simulations." *A&A* 515: (2010) A70+.

Ferreira, J. "The inner magnetized regions of circumstellar accretion discs." *New Astron. Rev.* 52: (2008) 42–59.

Flaig, M., R. Kissmann, and W. Kley. "Growth of the MRI in accretion discs - the influence of radiation transport." *MNRAS* 394: (2009) 1887 (FK2).

Flaig, M., W. Kley, and R. Kissmann. "Vertical structure and turbulent saturation level in fully radiative protoplanetary disc simulations." *MNRAS* 394: (2010) ??

Fleming, S., and R. P. Stone. "Local Magnetohydrodynamic Models of Layered Accretion Disks." *A&A* 585: (2003) 908–920

Flock, M., N. Dzyurkevich, H. Klahr, and A. Mignone. "High-order Godunov schemes for global 3D MHD simulations of accretion disks. I. Testing the linear growth of the magneto-rotational instability." *A&A* 516: (2010) A26+.

Fromang, S. "MHD simulations of thee magnetorotational instability in a shearing box withe zero net flux: thee case Pm = 4." *A&A* 514: (2010) L5+.

Fromang, S., and R. P. Nelson. "Global MHD simulations of stratified and turbulent protoplanetary discs. I. Model properties." *A&A* 457: (2006) 343–358.

———. "Global MHD simulations of stratified and turbulent protoplanetary discs. II. Dust settling." *A&A* 496: (2009) 597–608.

Fromang, S., and J. Papaloizou. "MHD simulations of the magnetorotational instability in a shearing box with zero net flux." *A&A* 476, 3: (2007) 1113–1122.

Fromang, S., J. Papaloizou, G. Lesur, and T. Heinemann. "MHD simulations of the magnetorotational instability in a shearing box with zero net flux. II. The issue of transport coefficients." *A&A* 476: (2007) 1123–1132.

Gammie, C. F. "Layered Accretion in T Tauri Disks." *ApJ* 457: (1996) 355–+.

Goodman, J., and G. Xu. “Parasitic instabilities in magnetized, differentially rotating disks.” *ApJ* 432: (1994) 213–223.

Guan, X., C. F. Gammie, J. B. Simon, and B. M. Johnson. “Locality of MHD Turbulence in Isothermal Disks.” *ApJ* 694: (2009) 1010–1018.

Guan, X., and C. Gammie. “Radially Extended, Stratified, Local Models of Isothermal Disks.” `arXiv:1012.3789`

Hartmann, L., N. Calvet, E. Gullbring, and P. D’Alessio. “Accretion and the Evolution of T Tauri Disks.” *ApJ* 495: (1998) 385–+.

Hawley, J. F. “Global Magnetohydrodynamical Simulations of Accretion Tori.” *ApJ* 528: (2000) 462–479.

———. “Global Magnetohydrodynamic Simulations of Cylindrical Keplerian Disks.” *ApJ* 554: (2001) 534–547.

Hawley, J. F., C. F. Gammie, and S. A. Balbus. “Local Three-dimensional Magnetohydrodynamic Simulations of Accretion Disks.” *ApJ* 440: (1995) 742–+.

———. “Local Three-dimensional Simulations of an Accretion Disk Hydromagnetic Dynamo.” *ApJ* 464: (1996) 690–+.

Hawley, J. F., and J. H. Krolik. “Global MHD Simulation of the Inner Accretion Disk in a Pseudo-Newtonian Potential.” *ApJ* 548: (2001) 348–367.

Hawley, John F., Steven A. Balbus, and Wayne F. Winters. “Local Hydrodynamic Stability of Accretion Disks.” *ApJ* 518, 1: (1999) 394–404.

Hayashi, C. “Structure of the Solar Nebula, Growth and Decay of Magnetic Fields and Effects of Magnetic and Turbulent Viscosities on the Nebula.” *Progress of Theoretical Physics Supplement* 70: (1981) 35–53.

Hirose, S., J. H. Krolik, and J. M. Stone. “Vertical Structure of Gas Pressure-dominated Accretion Disks with Local Dissipation of Turbulence and Radiative Transport.” *ApJ* 640: (2006) 901–917.

Hubeny, I. “Vertical structure of accretion disks - A simplified analytical model.” *ApJ* 351: (1990) 632–641.

Hueso, R., and T. Guillot. “Evolution of protoplanetary disks: constraints from DM Tauri and GM Aurigae.” *A&A* 442: (2005) 703–725.

Hügelmeyer, S.D. *Multidimensional radiative transfer in circumstellar disks.* Ph.D. thesis, Georg-August-Universität Göttingen, Göttingen, 2009.

Hughes, A. M., D. J. Wilner, J. Cho, D. P. Marrone, A. Lazarian, S. M. Andrews, and R. Rao. “Stringent Limits on the Polarized Submillimeter Emission from Protoplanetary Disks.” *ApJ* 704: (2009) 1204–1217.

Isella, A., L. Testi, A. Natta, R. Neri, D. Wilner, and C. Qi. “Millimeter imaging of HD 163296: probing the disk structure and kinematics.” *A&A* 469: (2007) 213–222.

Jin, L. “Damping of the Shear Instability in Magnetized Disks by Ohmic Diffusion.” *ApJ* 457: (1996) 798–+.

King, A. R., and J. E. Pringle. “The accretion disc dynamo in the solar nebula.” *MNRAS* 404: (2010) 1903–1909.

King, A. R., J. E. Pringle, and M. Livio. “Accretion disc viscosity: how big is alpha?” *MNRAS* 376: (2007) 1740–1746.

Kissmann, Ralf. *Numerical Investigation of the Turbulent ISM.* Ph.D. thesis, Ruhr-Universität Bochum, 2006.

Klahr, H. “The Global Baroclinic Instability in Accretion Disks. II. Local Linear Analysis.” *ApJ* 606: (2004) 1070–1082.

Lyra, W. and Klahr, H. “The Baroclinic Instability in the Context of Layered Accretion. Self-sustained Vortices in Local Compressible Unstratifed Models of Protoplanetary Disks.” `arXiv:1011.0497`

Kley, W., J. C. B. Papaloizou, and D. N. C. Lin. “On the Angular Momentum Transport Associated with Convective Eddies in Accretion Disks.” *ApJ* 416: (1993) 679–+.

Krolik, J. H., S. Hirose, and O. Blaes. “Thermodynamics of an Accretion Disk Annulus with Comparable Radiation and Gas Pressure.” *ApJ* 664: (2007) 1045–1056.

Kurganov, A., S. Noelle, and G. Petrova. “Semidiscrete Central-Upwind Schemes for Hyperbolic Conservation Laws and Hamilton–Jacobi Equations.” *SIAM J. Sci. Comput.* 23, 3: (2001) 707–740.

Lada, C. J. “Star formation - From OB associations to protostars.” In *Star Forming Regions*, edited by M. Peimbert & J. Jugaku. 1987, volume 115 of *IAU Symposium*, 1–17.

Larson, R. B. “The physics of star formation.” *Reports on Progress in Physics* 66: (2003) 1651–1697.

Lesur, G., and J. C. B. Papaloizou. “The subcritical baroclinic instability in local accretion disc models.” *A&A* 513: (2010) A60+.

Levermore, C. D., and G. C. Pomraning. “A flux-limited diffusion theory.” *ApJ* 248: (1981) 321–334.

Levy, E. H., and C. P. Sonett. “Meteorite magnetism and early solar system magnetic fields.” In *IAU Colloq. 52: Protostars and Planets*, edited by T. Gehrels. 1978, 516–532.

Lodato, G. “Classical disc physics.” *New Astron. Rev.* 52: (2008) 21–41.

Londrillo, P., and L. Del Zanna. “High-Order Upwind Schemes for Multidimensional Magnetohydrodynamics.” *ApJ* 530: (2000) 508–524.

Machida, M., and R. Matsumoto. “Excitation of Low-Frequency QPOs in Black-Hole Accretion Flows.” *PASJ* 60: (2008) 613

Matsumoto, R., and K. Shibata. “Three-Dimensional Global MHD Simulations of Magnetised Accretion Disks and Jets.” In *IAU Colloq. 163: Accretion Phenomena and Related Outflows*, edited by D. T. Wickramasinghe, G. V. Bicknell, & L. Ferrario. 1997, volume 121 of *Astronomical Society of the Pacific Conference Series*, 443–+.

McCaughrean, M. J., and C. R. O’Dell. “Direct Imaging of Circumstellar Disks in thee Orion Nebula.” *AJ* 111: (1996) 1977–+.

Miller, K. A., and J. M. Stone. “The Formation and Structure of a Strongly Magnetized Corona above a Weakly Magnetized Accretion Disk.” *ApJ* 534: (2000) 398–419.

Miyoshi, Takahiro, and Kanya Kusano. “A multi-state HLL approximate Riemann solver for ideal magnetohydrodynamics.” *Journal of Computational Physics* 208, 1: (2005) 315 – 344. `http://www.sciencedirect.com/science/article/B6WHY-4FY3P80-7/2/426234268c96dcca8a828d098b75fe4e`.

Najita, J., J. S. Carr, A. E. Glassgold, F. H. Shu, and A. T. Tokunaga. “Kinematic Diagnostics of Disks around Young Stars: CO Overtone Emission from WL 16 and 1548C27.” *ApJ* 462: (1996) 919–+.

Natta, A., L. Testi, N. Calvet, T. Henning, R. Waters, and D. Wilner. “Dust in Protoplanetary Disks: Properties and Evolution.” *Protostars and Planets V* 767–781.

Oishi, J. S., and M.-M. Mac Low. “On Hydrodynamic Motions in Dead Zones.” *ApJ* 704: (2009) 1239–1250

O’Neill et al. “Low-Frequency Oscillations in Global Simulations of Black Hole Accretion.” `arXiv:1009.1882`

Oppenheimer, M., and A. Dalgarno. “The Fractional Ionization in Dense Interstellar Clouds.” *ApJ* 192: (1974) 29–32.

Pringle, J. E. “Accretion discs in astrophysics.” *ARA&A* 19: (1981) 137–162.

Rempel, E. L., G. Lesur, and M. R. E. Proctor. “Supertransient Magnetohydrodynamic Turbulence in Keplerian Shear Flows.” *Physical Review Letters* 105, 4: (2010) 044,501–+.

Ruoff, Patrick. *Chemistry in Protoplanetary Discs.* Ph.D. thesis, Eberhard Karls Universität Tübingen, 2010.

Sano, T., and S. M. Miyama. “Magnetorotational Instability in Protoplanetary Disks. I. On the Global Stability of Weakly Ionized Disks with Ohmic Dissipation.” *ApJ* 515: (1999) 776–786.

Sano, T., S. M. Miyama, T. Umebayashi, and T. Nakano. “Magnetorotational Instability in Protoplanetary Disks. II. Ionization State and Unstable Regions.” *ApJ* 543: (2000) 486–501.

Sano, Takayoshi, and Shu-ichiro Inutsuka. “Saturation and Thermalization of the Magnetorotational Instability: Recurrent Channel Flows and Reconnections.” *The Astrophysical Journal Letters* 561, 2: (2001) L179–L182.

Schekochihin, A. A., S. A. Boldyrev, and R. M. Kulsrud. “Spectra and Growthe Rates of Fluctuating Magnetic Fields in thee Kinematic Dynamo Theeory withe Large Magnetic Prandtl Numbers.” *ApJ* 567: (2002a) 828–852.

Schekochihin, A. A., J. L. Maron, S. C. Cowley, and J. C. McWilliams. “Thee Small-Scale Structure of Magnetohydrodynamic Turbulence withe Large Magnetic Prandtl Numbers.” *ApJ* 576: (2002b) 806–813.

Shakura, N. I., and R. A. Sunyaev. “Black holes in binary systems. Observational appearance.” *A&A* 24: (1973) 337–355.

Shi, J., J. H. Krolik, and S. Hirose. “What is the Numerically Converged Amplitude of Magnetohydrodynamics Turbulence in Stratified Shearing Boxes?” *ApJ* 708: (2010) 1716.

Sicilia-Aguilar, A., L. Hartmann, N. Calvet, S. T. Megeath, J. Muzerolle, L. Allen, P. D’Alessio, B. Merin, J. Stauffer, E. Young, and C. Lada. “Disk Evolution in Cep OB2: Results from the Spitzer Space Telescope.” *ApJ* 638: (2006) 897–919.

Simon, J. B., J. F. Hawley, and K. Beckwith. “Simulations of Magnetorotational Turbulence with a Higher-Order Godunov Scheme.” *ApJ* 690: (2009) 974–997.

———. “Resistivity-driven State Changes in Vertically Stratified Accretion Disks.” *ArXiv e-prints* .

Stone, J. M., and T. A. Gardiner. “Implementation of the Shearing Box Approximation in Athena.” *ApJS* 189: (2010) 142–155.

Stone, J. M., J. F. Hawley, C. F. Gammie, and S. A. Balbus. “Three-dimensional Magnetohydrodynamical Simulations of Vertically Stratified Accretion Disks.” *ApJ* 463: (1996) 656–+.

Stone, J. M., and M. L. Norman. “ZEUS-2D: A radiation magnetohydrodynamics code for astrophysical flows in two space dimensions. I - The hydrodynamic algorithms and tests.” *ApJS* 80: (1992) 753–790.

Suzuki, T. K., and S.-i. Inutsuka. “Disk Winds Driven by Magnetorotational Instability and Dispersal of Protoplanetary Disks.” *ApJ* 691: (2009) L49–L54.

Tamura, M., J. H. Hough, J. S. Greaves, J.-I. Morino, A. Chrysostomou, W. S. Holland, and M. Momose. “First Detection of Submillimeter Polarization from T Tauri Stars.” *ApJ* 525: (1999) 832–836.

Tanga, P., A. Babiano, B. Dubrulle, and A. Provenzale. “Forming Planetesimals in Vortices.” *Icarus* 121: (1996) 158–170.

Turner, N. J. “On the Vertical Structure of Radiation-dominated Accretion Disks.” *ApJ* 605: (2004) L45–L48.

Turner, N. J., and T. Sano. “Dead Zone Accretion Flows in Protostellar Disks.” *ApJ* 679: (2008) L131–L134.

Turner, N. J., J. M. Stone, and T. Sano. "Local Axisymmetric Simulations of Magnetorotational Instability in Radiation-dominated Accretion Disks." *ApJ* 566: (2002) 148–163.

von Neumann, J., and R. D. Richtmyer. "A Method for the Numerical Calculation of Hydrodynamic Shocks." *J. Appl. Phys.* 21: (1950) 232.

Wardle, M. "Magnetic fields in protoplanetary disks." *Ap&SS* 311: (2007) 35–45.

Weidenschilling, S. J. "The distribution of mass in the planetary system and the solar nebula." *Ap&SS* 51: (1977) 153–158

Weiss, B. P., J. Gattacceca, S. Stanley, P. Rochette, and U. R. Christensen. "Paleomagnetic Records of Meteorites and Early Planetesimal Differentiation." *Space Sci. Rev.* 152: (2010) 341–390.

Wilner, D. J., P. D'Alessio, N. Calvet, M. J. Claussen, and L. Hartmann. "Toward Planetesimals in the Disk around TW Hydrae: 3.5 Centimeter Dust Emission." *ApJ* 626: (2005) L109–L112.

Youdin, A. N. and Goodman, J. "Streaming Instabilities in Protoplanetary Disks." *ApJ* 620: (2005) 459-460.

Ziegler, U. "A central-constrained transport scheme for ideal magnetohydrodynamics." *Journal of Computational Physics* 196, 2: (2004) 393 – 416.

Appendix A: Table of Physical and Astronomical Constants

Speed of light	c	$2.99792458 \cdot 10^{10}$ cm s^{-1}
Gravitational constant	G	$6.67259 \cdot 10^{-8}$ cm^{3} g^{-1} s^{-2}
Electron charge	e	$4.8032068 \cdot 10^{-10}$ esu
Mass of electron	m_e	$9.1093897 \cdot 10^{-28}$ g
Boltzmann's constant	k_B	$1.380658 \cdot 10^{-16}$ erg K^{-1}
Radiation density constant	a	$7.5646 \cdot 10^{-15}$ erg cm^{-3} K^{-4}
Mass of hydrogen	m_H	$1.6733 \cdot 10^{-24}$ g
$M_\odot$	Mass of the Sun	$1.99 \cdot 10^{33}$ g
Astronomical unit	AU	$1.496 \cdot 10^{13}$ cm

Tab. A.1: Table of fundamental physical and astronomical constants used in the present work.

Appendix B: Table of Mathematical Symbols

ρ	density
$\boldsymbol{v}$	velocity
$\boldsymbol{B}$	magnetic induction
p	pressure
e	thermal energy
E	radiation energy
E_{tot}	total energy
$\boldsymbol{F}$	radiation flux
T	temperature
ν	viscosity
η	Ohmic resistivity
$\varSigma$	surface density
$M_\star$	mass of central star
$\varOmega$	angular orbital frequency
μ	mean molecular weight
$\varPhi$	gravitational potential

Tab. B.1: Table listing the most important mathematical symbols used in the present work.

Curriculum Vitae

Persönliche Angaben

Name	Markus Flaig
Familienstand	verheiratet, 1 Kind
Staatsangehörigkeit	deutsch
Geburtsdatum	17.02.1978
Geburtsort	Oberndorf a.N.

Schulbildung

1985 - 1989	Grundschule Waldmössingen
1989 - 1995	Realschule Dunningen, Realschulreife Juni 1995
1995 - 1998	Wirtschaftsgymnasium Rottweil Abitur Juni 1998, Note: 1,3

Wehr- / Zivildienst

1999 - 2000	Zivildienst im Antonie-Maurer-Haus (Wohnheim für Behinderte) in Waldmössingen

Berufliche Tätigkeit

2000 - 2001	Tätigkeit als freier Mitarbeiter in selbiger Einrichtung

Wissenschaftlicher Werdegang

2000 - 2007	Studium der Physik an der Eberhard Karls Universität Tübingen, Diplom Februar 2007, Note ‚sehr gut‘
2005 - 2007	Wissenschaftliche Hilfskraft an der Fakultät für Mathematik und Physik der Universität Tübingen
2007 - 2011	Anfertigung der vorliegenden Dissertation *Magnetorotational Turbulence in Protoplanetary Discs* am Institut für Computational Physics der Universität Tübingen unter Anleitung von Prof. Dr. W. Kley
2007 - 2011	Wissenschaftlicher Angestellter am Institut für Computational Physics der Universität Tübingen

Akademische Lehrer

H. Clement, J. Frauendiener, H. Kaul, R. Kleiner, W. Kley, D. Kölle, M. Liu, H. Müther, F. Nüsslin, H. Reinhardt, U. Schlotterbeck, N. Schopohl, G. J. Wagner, K. Werner